Air Force Institute of Technology
AFIT Scholar

Theses and Dissertations | Student Graduate Works

3-22-2019

Micro-contacts with 3-D Surfaces made with Grayscale Lithography

Paul L.J. Michaud

Follow this and additional works at: https://scholar.afit.edu/etd

Part of the Electro-Mechanical Systems Commons

Recommended Citation
Michaud, Paul L.J., "Micro-contacts with 3-D Surfaces made with Grayscale Lithography" (2019). *Theses and Dissertations*. 2271.
https://scholar.afit.edu/etd/2271

This Thesis is brought to you for free and open access by the Student Graduate Works at AFIT Scholar. It has been accepted for inclusion in Theses and Dissertations by an authorized administrator of AFIT Scholar. For more information, please contact richard.mansfield@afit.edu.

MICRO-CONTACTS WITH 3-D SURFACES MADE WITH GRAYSCALE LITHOGRAPHY

THESIS

Paul L.J. Michaud, 2nd Lieutenant, USAF

AFIT-ENG-MS-19-M-043

DEPARTMENT OF THE AIR FORCE
AIR UNIVERSITY

AIR FORCE INSTITUTE OF TECHNOLOGY

Wright-Patterson Air Force Base, Ohio

DISTRIBUTION STATEMENT A.
APPROVED FOR PUBLIC RELEASE; DISTRIBUTION UNLIMITED.

The views expressed in this thesis are those of the author and do not reflect the official policy or position of the United States Air Force, Department of Defense, or the United States Government. This material is declared a work of the U.S. Government and is not subject to copyright protection in the United States.

AFIT-ENG-MS-19-M-043

MICRO-CONTACTS WITH 3-D SURFACES MADE WITH GRAYSCALE LITHOGRAPHY

THESIS

Presented to the Faculty

Department of Electrical and Computer Engineering

Graduate School of Engineering and Management

Air Force Institute of Technology

Air University

Air Education and Training Command

In Partial Fulfillment of the Requirements for the

Degree of Master of Science in Electrical Engineering

Paul L.J. Michaud, B.S.E.E

2nd Lieutenant, USAF

March 2019

DISTRIBUTION STATEMENT A.
APPROVED FOR PUBLIC RELEASE; DISTRIBUTION UNLIMITED.

AFIT-ENG-MS-19-M-043

MICRO-CONTACTS WITH 3-D SURFACES MADE WITH GRAYSCALE LITHOGRAPHY

Paul L.J. Michaud, B.S.E.E

2nd Lieutenant, USAF

Committee Membership:

Maj Tod V. Laurvick, PhD
Chair

Dr. Hengky Chandrahalim
Member

Dr. F. Kenneth Hopkins
Member

AFIT-ENG-MS-19-M-043

Abstract

MEMS switches show advantages over FET transistors and PIN diodes for switching applications due to low contact resistance, high linearity, low power use, better isolation and lower insertion loss. The switches have not replaced FETs or PIN diodes due to perceived limitations in their reliability and the need for stable contact resistance. In order to create switches acceptable for industry applications, research on micro-contact physics and failure mechanisms of micro-contacts is necessary to develop durable contact surfaces. The aim of this research was to design and fabricate micro-contacts with three-dimensional surfaces using grayscale lithography. The goal was to create devices that have stable resistances within the ballistic electron transport region. These devices were designed to restrict current to smaller areas to take advantage of micro-contact physics. The micro-contacts were designed using a 2^4 factorial to determine factors that are significant to operating within the ballistic regime and maintaining stable contact resistances. The contacts were tested in a test stand filled with nitrogen gas that uses a piezoelectric actuator to cycle the devices with an applied signal for a specified number of cycles. The contact resistance and contact force were recorded at certain points during testing. Testing revealed that certain micro-contacts with three-dimensional surfaces fit into the ballistic electron transport model for 1 million cycles. After testing, the micro-contacts were inspected using a Scanning Electron Microscope and 3-D microscope to determine the presence of failure mechanisms.

Acknowledgments

I would like to express my sincere appreciation to my faculty advisor, Maj Tod Laurvick, for his guidance and support throughout the course of this thesis effort. The insight and experience was greatly appreciated. I would like to thank the clean room technicians, Rich Johnston and Adam Fritzche, for all their help with lab equipment. I would also like to thank my friends, classmates, and family for their help with troubleshooting, proofreading, and providing guidance and support. Special thanks go out the Air Force Research Laboratories for helping fabricate devices when not possible at AFIT.

Paul L.J. Michaud

Table of Contents

Page

Abstract ... iv

Table of Contents ... vi

List of Figures ... ix

List of Tables ... xvi

I. Introduction ... 1

1.1 Problems with MEMS Switches ... 2

1.2 Focus and Motivation of Thesis Research ... 3

1.3 Chapter Summary ... 3

II. Literature Review ... 4

2.1 Chapter Overview ... 4

2.2 Micro-contact Resistance and Modeling ... 4

2.3 Device Fabrication Used for Research ... 16

2.4 Micro-contact Causes of Failure ... 24

2.5 Micro-contact Reliability ... 32

2.6 Test Fixture ... 36

2.7 Chapter Summary ... 39

III. Methodology ... 41

3.1 Chapter Overview ... 41

3.2 Micro-contact Fabrication ... 41

3.3 Grayscale Lithography ... 42

3.4 Design of Experiments ... 44

3.5 Resistance Modeling ... 49

3.6 Test Stand ... 51

3.7 Types of Testing 54

3.8 Examination of Contacts 55

3.9 Chapter Summary 56

IV. Analysis and Results 58

4.1 Chapter Overview 58

4.2 Fabrication Analysis 58

4.3 Micro-contact Design #1 with 6 µm Bump...63

4.4 Micro-contact Design #4 with 6 µm Bump...68

4.5 Micro-contact Design #1 with 8 µm Bump...71

4.6 Micro-contact Design #5 with 8 µm Bump...74

4.7 Micro-contact Failure Prediction: Design #8 with 6 µm Bump.......................77

4.8 Micro-contacts used as Controls 80

4.9 Comparison Testing 85

4.10 Resistance and Standard Deviation of Micro-contacts 92

4.11 Chapter Summary 93

V. Conclusions and Recommendations 95

5.1 Chapter Overview 95

5.2 Conclusions of Research 95

5.3 Recommendations for Future Research 96

5.4 Chapter Summary 98

Appendix A. Mask Layouts 100

Appendix B. Process Followers 102

Appendix C. Grayscale Designs 110

Appendix D. MATLAB Code...119

Bibliography 126

List of Figures

Figure Page

1. Surface of a micro-contact with several a-spots [7].. 5

2. Illustration showing diffusive and ballistic electron transport in a conductor [11]. 9

3. Gamma function from Mikrajuddin *et al.* [11]. 10

4. Spreading of current streamlines near a constriction between two thin films with r_A being the inner radius [15]. 12

5. Spreading of current streamlines in two bulk conductors [15]. 13

6. Diagram of a thin film [16]. 14

7. Modeling of a fixed-fixed beam [8]. 19

8. Process to create fixed-fixed beam structures using surface micromachining techniques [8]. 21

9. CAD designs used for different exposure amounts [23]. 23

10. 2D pyramid structures created using grayscale lithography and RIE [8]. 24

11. SEM image showing the stiction failure of the bottommost cantilever beam [25]. ... 26

12. SEM image showing fretting wear scars [26]. 27

13. SEM image of a Ruthenium micro-contact after undergoing trailing edge hot switching showing a void caused by material transfer [4]. 29

14. SEM images showing frictional polymer formation on a Ruthenium contact where the polymer appears from the surface adjoining the contact site [3]. 30

15. “Bathtub” reliability curve to model the failure rate of devices [24]. 33

16. Test stand for testing micro-contacts [6]. 39

17. Design of the fixed-fixed beam created using L-Edit software with its dimensions labeled. There is a 3 μm gap between the electroplated beam and the bottom metal. 42

18. Cross section of a wafer to determine the selectivity. 44

19. Experimental runs for the initial design. 46

20. L-Edit designs for the 2^4 factorial experiment. Each design is 32 μm by 32 μm. The white denotes the highest point of the micro-contact and the dark blue denotes the lowest point of the contact. 47

21. Additional designs created in L-Edit for fabrication and testing. 48

22. Contact Resistance model created with MATLAB to show the differences between contacts undergoing plastic or elastic deformation. 49

23. Contact Resistance model created with MATLAB to compare the resistance of contacts with ballistic electron transport to contacts with diffusive electron transport. 50

24. Micro-contact support structure that enables the Holm crossbar technique to be used to determine the contact resistance [8]. 52

25. Image of the carrier with a chip having devices under test. 53

26. Schematic of a DUT connected to the test stand equipment. 53

27. Current version of the test stand with new cameras mounted around it. 54

28. New Alignment marks designed using L-Edit software to align the wafer to the bottom metal patterns. 59

29. Comparison between the L-Edit design of the micro-contact and the actual micro-contact after fabrication. 61

30. Comparison between the L-Edit design of the micro-contact and the actual micro-contact after fabrication. 61
31. Electroplated beam that did not need gold etching. 62
32. Electroplated beam after 12 minutes of gold etching to make it thinner. 63
33. Micro-contact design in L-Edit specified by DOE run #1 and the resulting design after fabrication. 63
34. Contact resistance of DOE design #1 after 10 cycles compared to models for ballistic electron transport with a Knudsen number of 10, labeled as RcB and diffuse electron transport, labeled as RcDE. 64
35. Resistance of the micro-contact while 100 µN were applied for the duration of testing, where BET stands for ballistic electron transport. An increase in resistance is thought to be because of electromigration. 65
36. Lowest resistances recorded of the micro-contact for the duration of testing. 66
37. SEM image of the micro-contact after testing on the left, and image taken with a 3-D microscope on the right. 67
38. SEM image of the damage caused by electromigration on the micro-contact. 67
39. Micro-contact design in L-Edit specified by DOE run #4 and the resulting design after fabrication. 68
40. Resistance of the micro-contact for forces up to 200 µN after 10 cycles compared to models for ballistic electron transport with a Knudsen of 10, labeled as RcB and for diffusive electron transport labeled as RcDE. 69
41. Resistance of the micro-contact while 100 µN was applied at each test point. The micro-contact underwent 10^6 cycles. 70

42. Lowest resistance recorded while a force was applied for each test point. The micro-contact underwent 10^6 cycles. 70
43. Design of the micro-contact as well as an image of the actual contact. 71
44. Resistance of the micro-contact for forces up to 200 μN after 39,810 cycles. The irregular shape of the curve does not match either model and is an indication that a failure mechanism is occurring. 72
45. Resistance of the micro-contact after a million cycles for forces up to 200 μN......... 72
46. Resistance of the micro-contact while 100 μN is applied taken at test points spread out over the duration of testing. The sharp increase in resistance near the end of testing is an indicator of a failure mechanism. 73
47. Lowest resistance recorded of the micro-contact measured at test points for the duration of testing. 74
48. Design of the micro-contact and an image of the actual micro-contact. 75
49. Contact resistance for forces up to 200 μN after the millionth cycle. 76
50. Contact resistance measured while 100 μN was applied to the beam taken at test points throughout testing. 76
51. Lowest contact resistance measured while a force was applied taken at test points during testing. The resistance shows that the micro-contact underwent ballistic electron transport for the duration of testing. 77
52. Design and image of the micro-contact that was tested for a million cycles.............. 78
53. Resistance of the micro-contact for forces up to 200 μN after 10 cycles. The irregular shaped curve is an indicator that the contact is being affected by a failure mechanism. 78

54. Resistance of the micro-contact with 100 μN applied to the beam taken at test points throughout testing. 79

55. The lowest resistances measured while a force was applied to the beam for the micro-contact taken at test points throughout testing. 80

56. Resistance of the micro-contact with 100 μN applied to the beam taken at test points throughout testing. BET stands for ballistic electron transport and DET stands for diffusive electron transport. 81

57. The lowest resistances measured while a force was applied to the beam for the micro-contact taken at test points throughout testing. The control micro-contact remained diffuse after the initial wear-in period. 82

58. Resistance of the micro-contact with 100 μN applied to the beam taken at test points throughout testing. 83

59. The lowest resistances measured while a force was applied to the beam for the micro-contact taken at test points throughout testing. 84

60. Image taken with the 3-D microscope showing that electromigration started to occur on the bottom contact. 84

61. SEM image showing the damage caused by electromigration to the bottom contact. 85

62. Comparison of the resistance measured when 100 μN is applied between a contact with a 3-D surface and one without. 86

63. Comparison of the lowest resistances recorded while a force was applied between a contact with a 3-D surface and one without. 87

64. Comparison of the resistance measured when 100 μN is applied between a contact with a 0.5 V load and one with a 1 V load. 88

65. Comparison of the lowest resistances recorded while a force was applied between a contact with a 0.5 V load and one with a 1 V load. 89
66. Resistance of the micro-contacts for forces up to 200 µN after 100,000 cycles. 90
67. Resistance of the micro-contacts for forces up to 200 µN after a million cycles. 91
68. Comparison of the resistance measured when 100 µN is applied between a contact with a 6 µm upper bump radius and an 8 µm upper bump radius............................. 91
69. Comparison of the lowest resistances recorded while a force was applied between a contact with a 6 µm upper bump radius and an 8 µm upper bump radius. 92
70. Overlay of five masks that were designed for use with a dual camera alignment system. The mask includes a single horizontal strip and alignment marks. For this research, only the top two regions are used. The top two contain 16 devices per reticle with a fixed-fixed beam with 8 or 6 micron contact bumps [6]. 100
71. Mask layout for grayscale lithography that lines up with the masks in Figure 70. This is the first lithography step done in the process follower and is a direct write with the Heidelberg mask writer rather than using an actual mask. 101
72. DOE design #1: small circles 4 µm apart 110
73. DOE design #2: large circles 4 µm apart 110
74. DOE design #3: small squares 4 µm apart 111
75. DOE design #4: large squares 4 µm apart 111
76. DOE design #5: small circles 6 µm apart 111
77. DOE design #6: large circles 6 µm apart 112
78. DOE design #7: small squares 6 µm apart 112
79. DOE design #8: large squares 6 µm apart 112

80. Miscellaneous design #1 113

81. Miscellaneous design #2 113

82. Miscellaneous design #3 114

83. Miscellaneous design #4 114

84. Miscellaneous design #5 114

85. Miscellaneous design #6 115

86. Miscellaneous design #7 115

87. Miscellaneous design #8 115

88. Miscellaneous design #9 116

89. Miscellaneous design #10 116

90. Miscellaneous design #11 116

91. Miscellaneous design #12 117

92. Miscellaneous design #13 117

93. Miscellaneous design #14 118

94. Miscellaneous design #15 118

95. Miscellaneous design #16 118

List of Tables

Table Page

1. Settings used to create grayscale micro-contacts with the Heidelberg Mask Writer.... 43

2. Measurements taken after grayscale lithography and after RIE exposure to calculate the selectivity. 60

3. Resistance for certain cycles and standard deviation of the resistance of the devices tested. The green boxes indicate that a device operated within the ballistic electron transport model.. 93

MICRO-CONTACTS WITH 3-D SURFACES MADE WITH GRAYSCALE LITHOGRAPHY

I. Introduction

As the reliability of Micro-Electronic Mechanical System (MEMS) devices, specifically switches, become more advanced, the prevalence of their use becomes more widespread. MEMS devices are used in automobiles, printers, cellular phones, and overhead projectors [1]. In the Radio Frequency (RF) community, MEMS components are found in attenuators, limiters, phase shifters, transmit/receive switches and tunable matching networks. Some of the radar subsystems that benefit from RF MEMS technology include active electronically scanned arrays, passive electronically scanned arrays, and radomes [2]. Technology that benefits from using RF MEMS switches includes RF beamforming, switch matrices for satellite switching networks, programmable filters, zero standby-power self-aware systems, cellphone front ends, and automated test equipment [3]–[5]. MEMS switches are seen to be paramount in ushering in the next generation of RF circuits and applications due to their extremely low power consumption, small geometries, and superior RF performance. The use of MEMS switches over conventional electronic switches such as Field Effect Transistors (FETs) and PIN diodes is due to their low insertion loss (~0.2dB), high isolation (20-30dB) and their broadband operation (DC-40 GHz) [1]. The cut-off frequency for RF MEMS

switches ranges from 10-20 THz which is ten times higher than the value for PIN diodes and GaAs FETs [3].

1.1 Problems with MEMS Switches

Before MEMS switches can be adapted for use in the next generation of electronic devices, several problems must be overcome. There are three inherent factors to any microswitch: the contact resistance reached by the micro-contact within the microswitch, the variance present in the contact resistance, and the cycles a device is capable of undergoing before failure or unacceptable degradation of performance [6]. MEMS switches still have not been fully accepted in the cellular or automotive industries to replace conventional electronic switches due to limitations in the duration of their lifetime of performance and due to not having a stable contact resistance. For industry acceptance, a goal of at least 200 billion cycles to a trillion cycles for reliability has been set for use in RF applications, communications equipment or high-speed data processing applications [1], [6]. In order to create microswitches and micro-contacts that can remain reliable over this amount of cycles, the problem can be engineered away or research on the fundamentals of micro-contact physics and thin film metallurgy can be applied toward designs. The latter is considered the way ahead for the MEMS community. It would have researchers focus on learning the root causes of device failure rather than just avoiding failure and not learning from the process [1]. This research aims to apply known micro-contact physics as well as modern lithography techniques to the creation of micro-contacts in order to produce better microswitches.

1.2 Focus and Motivation of Thesis Research

The focus of this work is to design and fabricate three-dimensional surfaces on micro-contacts using grayscale lithography to operate in the ballistic electron transport region and to lower the variance of the contact resistance. The designs will attempt to take advantage of the physics of ballistic electron transport to reduce the effects of joule heating by restricting the contacting surface to several small areas. Having micro-contacts that operate in the ballistic electron transport region is a first step toward creating micro-contacts that operate for a trillion cycles. Testing will be done to determine if micro-contacts operated within the ballistic electron transport model and to investigate whether there are advantages to using specific geometries, spacing, upper contact bumps, or voltage loads on the micro-contacts.

1.3 Chapter Summary

The problems with MEMS switches are a great opportunity to test micro-contact physics in an attempt to operate within the ballistic electron transport model and to stabilize their contact resistance. The focus of this work is in applying grayscale lithography to restrict the contacting surface area of the micro-contacts. The next section of this document is used to discuss relevant research and literature in the field of micro-contacts and lithography that will help with the design, fabrication, and testing of micro-contacts with three-dimensional surfaces.

II. Literature Review

2.1 Chapter Overview

The purpose of this chapter is to review relevant literature pertaining to the topic of micro-contacts and MEMS processes. It will cover modeling of micro-contacts, device fabrication, grayscale lithography, micro-contact failure mechanisms, reliability of devices, and the test stand for experimentation.

2.2 Micro-contact Resistance and Modeling

Modeling micro-contacts requires a knowledge of contact surfaces and the way the surfaces interact when brought into contact. Micro-contacts have irregularities on their surfaces that are large relative to the size of the contact area. In other words, micro-contacts have rough surfaces and is the main difference from macro-scale contacts. Most modeling of a micro-contact centers around the contact area, the surface roughness of the contacts, and the deformation of the contact surfaces [7]. The surfaces of the contacts are covered in asperity peaks, known as 'a-spots' which are the interfaces where the contacts meet and become the contact area [8]. The asperity peaks have been described as "small cold welds providing the only conducting paths for the transfer of electrical current" [7]. The effective contact area is much smaller than it would appear due to the asperity peaks being the only surfaces brought into contact [9]. Because current is constricted to the a-spots, the temperature at the a-spot while the switch is conducting is likely to be much higher than the rest of the switch. Additionally, the current is not uniformly spread which causes the a-spot temperature to be a function of the voltage drop rather than the current

[3]. A graphical representation of the surface of a micro-contact with several a-spots shown as an effective radius of the contact is shown in Figure 1 [7].

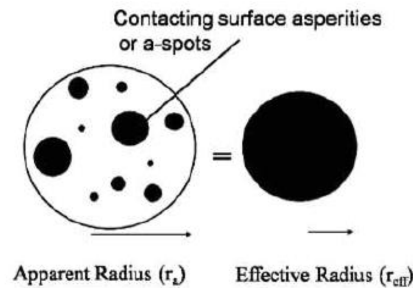

Figure 1. Surface of a micro-contact with several a-spots [7].

An ideal micro-contact is one that minimizes contact resistance, maximizes longevity, and maintains a consistent contact resistance by reducing variability. All three factors are important to consider in the design of micro-contacts [6].

Contact resistance is the convergence and spreading of the electrical current through conducting a-spots [7]. The minimization of the contact resistance is one of the factors mentioned before that go into producing ideal micro-contacts. The measured contact resistance gives a convenient way to determine if a contact is still functional and to compare stability between different devices. For example, a gradual increase in contact resistance over time can be an indicator that a contaminant film is forming and may lead to device failure [6].

Majumder *et al.* modeled the contact resistance of devices with three steps. The first determines the contact force as a function of the applied gate voltage. The second step determines the distribution and size of the areas in contact as a function of contact

force. The third step determines the contact resistance as a function of the distribution and size of the areas in contact. Majumder *et al.* also theorized and experimentally observed that the contact resistance decreases inversely with the number of contacts meaning that more contacts leads to a decrease in the overall contact resistance [10].

Understanding how contacts deform is important to predict their contact resistance. Contacts can deform elastically, plastically, or a combination of both. Elastic deformation of micro-contacts occurs when they undergo extremely low values of contact force, in the tens of micro-Newtons, and the asperities retain their physical shape once the force is removed [11].

Under elastic deformation, an asperity peak contact area is given by:

$$A = \pi R \alpha \tag{1}$$

where R is the asperity peak radius of curvature, and α is the asperity vertical deformation [12]. The contact force under elastic deformation is given by:

$$F_{cE} = \frac{4}{3} E' \alpha \sqrt{R\alpha} \tag{2}$$

where E' is the effective Hertzian modulus derived in Equation 3. In the effective Hertzian modulus, E_1 is the elastic modulus for the first contact, E_2 is the elastic modulus for the second contact, υ_1 is the Poisson's ratio for the first contact and υ_2 is the Poisson's ratio for the second contact [7].

$$\frac{1}{E'} = \frac{1 - \upsilon_1^2}{E_1} + \frac{1 - \upsilon_2^2}{E_2} \tag{3}$$

The effective contact radius of a micro-contact is important to the calculation of the contact resistance of micro-switches. The effective contact radius is the summation of the asperity peaks over the surface of a micro-contact that come into contact when a micro-contact closes as seen in Figure 1. For circular areas, the effective radius for elastic deformation is derived using Hertz's model:

$$r_{eff} = \sqrt[3]{\frac{3F_{cE}R}{4E'}} \tag{4}$$

Once the contact force between the micro-contacts is capable of causing permanent surface changes by the displacement of atoms in the asperity peaks, it is known as plastic deformation [13]. Under plastic deformation, the model from Abbot and Firestone is used which assumes sufficiently large contact pressure and no material creep [7]. The contact area of the asperity peak is calculated by:

$$A = 2\pi R\alpha \tag{5}$$

The contact force is calculated with the Meyer hardness of the softer material, H, and the contact area, A:

$$F_{cP} = HA \tag{6}$$

The effective contact radius for plastic deformation is then derived by:

$$r_{eff} = \sqrt{\frac{F_{cP}}{H\pi}} \tag{7}$$

Elastic-plastic deformation occurs at the boundary between permanent plastic deformation and temporary elastic deformation. This boundary is when parts of the contact area are plastically deforming but are encased by elastically deformed material [11]. The model provided by Chang *et al.* provide the equations governing the elastic-plastic transition [12]. The elastic-plastic material deformation contact area and force is given by:

$$A = \pi R\alpha\left(2 - \frac{\alpha_c}{\alpha}\right). \tag{8}$$

From this contact area, the elastic-plastic contact force can be calculated by:

$$F_{cEP} = K_Y A \tag{9}$$

where α_c is the critical vertical deformation and K_Y is the yield coefficient where the elastic-plastic transition begins [7], [12]. The effective contact radius for elastic-plastic deformation is given by:

$$r_{eff} = \sqrt{\frac{F_{cEP}}{H\pi\left[1.062+0.354\left(\frac{2}{3}K_Y-3\left(\frac{\alpha_c}{\alpha}\right)\right)\right]}} \tag{10}$$

The contact resistance of micro-switches is determined by whether they are undergoing elastic or plastic deformation as well as the type of electron transport. The electron transport regions are defined by comparing the electron's mean free path, l_e, to the contact area radius, r_{eff}. The region is ballistic when $l_e > r_{eff}$, quasiballistic when $l_e \sim r_{eff}$, and diffusive when $l_e < r_{eff}$. Most metals have a mean free path of approximately 500 Å [11]. The illustration showing the difference between diffusive and ballistic electron transport in a conductor is shown in Figure 2. When micro-contacts operate in the

diffusive electron region, some degree of joule heating occurs and may lead to electromigration. To avoid the effects of joule heating, it is desired to have micro-contacts operate in the ballistic electron region [6].

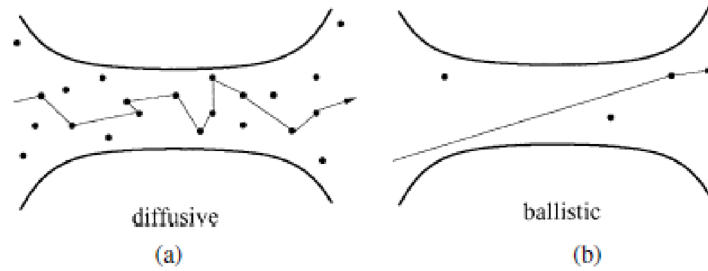

Figure 2. Illustration showing diffusive and ballistic electron transport in a conductor [11].

The contact resistance of circular contact areas undergoing elastic material deformation for diffusive electron transport is given by:

$$R_{cDE} = \frac{\rho}{2}\sqrt[3]{\frac{4E'}{3F_cR}} \tag{11}$$

where ρ is the resistivity of the metal. The contact resistance of circular contact areas undergoing plastic deformation for diffusive electron transport is given by:

$$R_{cDP} = \frac{\rho}{2}\sqrt{\frac{H\pi}{F_{cP}}} \tag{12}$$

When ballistic electron transport dominates during elastic deformation, the contact resistance is given by:

$$R_{cBE} = \frac{4\rho K}{3\pi r_{eff}} \sqrt[3]{\frac{4E'}{3F_c R}} \quad (13)$$

where K is the Knudsen number which is the ratio between the mean free path and the effective contact radius. Reducing the diameter of the contact spot is a method of increasing the Knudsen number and is possible with the use of grayscale lithography. The relationship between the Knudsen number and the region of electron transport is seen with the Gamma function presented by Mikrajuddin *et al.*:

$$\Gamma(K) \approx \frac{2}{\pi} \int_0^\infty e^{-Kx} Sinc(x) dx \quad (14)$$

and is seen graphically in Figure 3.

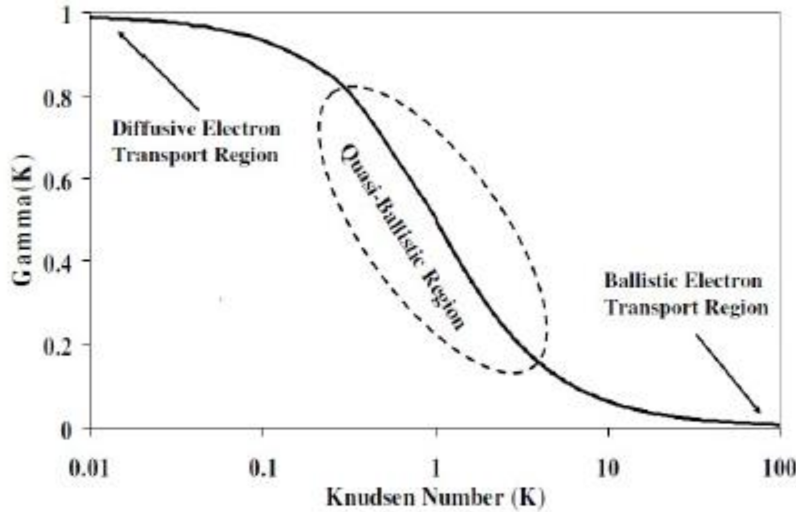

Figure 3. Gamma function from Mikrajuddin *et al.* [11].

The model that combines the resistances from ballistic electron transport and diffusive electron transport for elastic deformation is given by:

$$R_{WE} = R_{cBE} + \Gamma(K) R_{cDE} \tag{15}$$

The model was further improved by Coutu *et al*. to incorporate the effects of elastic-plastic deformation in the ballistic and diffusive electron transport equations for contact resistance. These equations are shown below [11].

$$R_{cBEP} = \frac{4\rho K}{3\pi}\sqrt{\frac{H\pi\left[1.062+0.354\left(\frac{2}{3}K_Y-3\left(\frac{\alpha_c}{\alpha}\right)\right)\right]}{F_c}} \tag{16}$$

$$R_{cDEP} = \frac{\rho}{2}\sqrt{\frac{H\pi\left[1.062+0.354\left(\frac{2}{3}K_Y-3\left(\frac{\alpha_c}{\alpha}\right)\right)\right]}{F_c}} \tag{17}$$

2.2.1 Spreading Resistance Modeling

The spreading resistance of thin films is important to be aware of when dealing with the thin deposition of metals used as contact material in MEMS switches. Karmalkar *et al.* derived a simple closed-form model to predict accurate complex calculations of circular and rectangular spreading resistances having equipotential or uniform current density, *J*, anodes located arbitrarily over the cathode area. They developed the model by solving the three-dimensional (3-D) Laplace equation in Equation 18 when subject to boundary conditions where ∇^2 is the Laplace operator and φ is a scalar function for potential. The model was shown to accurately predict trends of spreading resistance such as the significant variation as a function of the smaller electrode location, dependence on the electrode separation-to-width ratio, and saturation with increase in the larger electrode area for both equipotential and uniform *J* boundary conditions [14].

$$\nabla^2 \varphi = 0 \tag{18}$$

Timsit addressed the effect of film thickness on spreading resistance in a thin conducting layer. In a bulk interface, the electrical spreading resistance of a circular constriction is expressed by the classical relation:

$$R_s = \frac{\rho}{4a} \tag{19}$$

where ρ and a are the resistivity and the radius of the constriction, respectively. In a thin film, the spreading resistance stems from the resistance to electrical flow only in the conducting region where current spreading occurs in the immediate vicinity of the constriction in the film as shown in Figure 4. In this case, the current streamlines bend sharply away from the constriction edge and flow parallel to the film boundaries. This is contrasted in the spreading of current in bulk materials where the spreading occurs over a much larger region shown in Figure 5 [15].

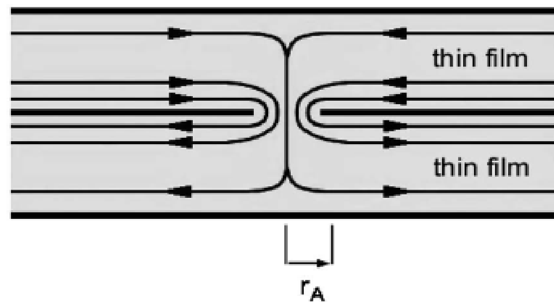

Figure 4. Spreading of current streamlines near a constriction between two thin films with r_A being the inner radius [15].

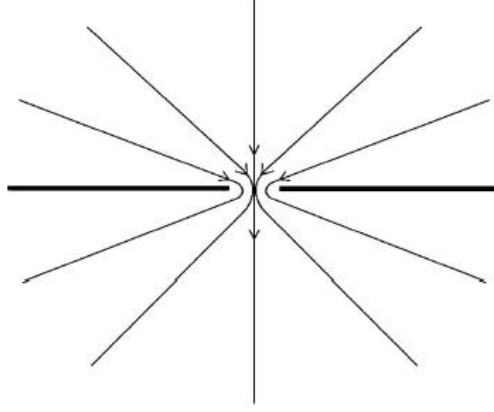

Figure 5. Spreading of current streamlines in two bulk conductors [15].

The bulk resistance, also called the resistance to radial flow in a ring is given by:

$$R_B = \frac{\rho}{2\pi L} \ln\left(\frac{b}{r_a}\right) \tag{20}$$

where L is the thickness, r_a is the inner radius, and b is the outer radius. The total resistance is derived using the equation that describes the distribution of potential within a film and three boundary conditions. The total resistance R_T between the center of the constriction and the outer boundary of the film at $r=b$ is given as:

$$R_T = \frac{V_0 - V(0,0)}{I} = \frac{\rho}{\pi a} \sum_{n=1}^{n=\infty} \coth\left(\frac{\lambda_n L}{b}\right) \frac{\sin(\frac{\lambda_n a}{b})}{J_1^2(\lambda_n)\lambda_n^2} \tag{21}$$

where ρ is the resistivity of the conducting material, a is the constriction radius, b is the outer radius, L is the film thickness, $J_0(x)$ is the Bessel function of the first kind and order zero and λ_n is the nth root of $J_0(\lambda_n) = 0$. The spreading resistance is determined after calculating the total resistance and the bulk resistance where $r_a = a$:

$$R_s = R_T - R_B \quad (22)$$

Timsit's study also observed that the constriction resistance between two identical thin films could be calculated as twice the spreading resistance. Another observation showed that the spreading resistance in a radially-conducting film decreases with decreasing film thickness even though it seems counter-intuitive when compared to a solid conductor which has increasing resistance as thickness decreases [15].

Zhang *et al.*'s study follows onto the work of Timsit to calculate the spreading resistance of an a-spot on a thin film. The study focuses on the thin film geometry that is shown in Figure 6 which has a thickness h, an electrical resistivity ρ, a contact radius a, and a bulk radius b. A voltage V_0 is applied uniformly along the edge of the thin film at $y = \pm b$ $(r=b)$. The top region AB is called the a-spot for the figure and a grounded electrode is attached to it.

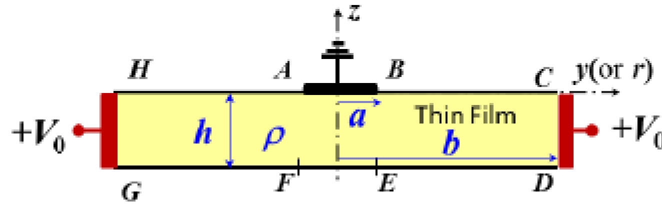

Figure 6. Diagram of a thin film [16].

Like Timsit, Zhang *et al.* use Equation 22 to determine the spreading resistance. They then defined R_{bulk} to be the bulk resistance from BE to CD and from AF to GH which in the Cartesian geometry is given by:

$$R_{bulk} = \rho(b - a)/2hW \quad (23)$$

where W is the channel length. The equation in the cylindrical geometry is given as:

$$R_{bulk} = \left(\frac{\rho}{2\pi h}\right) \ln\left(\frac{b}{a}\right) \tag{24}$$

Next they normalized the spreading resistance to the normalized resistance, which is shown first for the Cartesian geometry:

$$R_s = \frac{\rho}{4\pi W} \bar{R}_s \tag{25}$$

In the cylindrical geometry, the spreading resistance is given by:

$$R_s = \frac{\rho}{4a} \bar{R}_s \tag{26}$$

The normalized resistance depends only on the aspect ratios *a/h* and *a/b*. The normalized resistance referenced in equation 25. in the Cartesian geometry is expressed by:

$$\bar{R}_s = 2\pi \frac{a}{h} - 4 \ln\left[sinh\left(\frac{\pi}{2}\frac{a}{h}\right)\right] \tag{27}$$

The normalized resistance referenced in equation 26 for the cylindrical geometry is expressed by [16]:

$$\bar{R}_s = 1 - 2.2968\left(\frac{a}{h}\right) + 4.9412\left(\frac{a}{h}\right)^2 - 6.1773\left(\frac{a}{h}\right)^3 + 3.811\left(\frac{a}{h}\right)^4 - 0.8836\left(\frac{a}{h}\right)^5, 0 \leq \frac{a}{h} \leq 1;$$

$$\bar{R}_s = 0.28 + 0.0502\left(\frac{h}{a}\right) + 0.0523\left(\frac{h}{a}\right)^2, 1 < \frac{a}{h} < \infty \tag{28}$$

Zhang *et al.* also researched the effects of dissimilar materials on thin film contact resistance. They observed that if the constriction size (a) is small compared to the film

thickness (*h*), the thin film contact resistance is insensitive to the resistivity ratio, which is the ratio between the electrical resistivity of the two materials. If $a/h>1$, the contact resistance varies significantly with the resistivity ratio. Furthermore, the minimum contact resistance was typically realized when $a/h \sim 1$ for both Cartesian and cylindrical cases [17].

2.3 Device Fabrication Used for Research

MEMS devices are typically constructed using either surface micromachining or bulk micromachining. For this research conducted on micro-contacts, the focus will be on using surface micromachining to create the fixed-fixed beam structures. Lee defines surface micromachining as the formation of a structural layer on a sacrificial structure and the removal of the sacrificial layer to form a device. In order to generate patterns onto the structural layers, photolithography is used on light-sensitive materials. A mask is designed with patterns that are transparent or opaque to light which is then used to transfer the design with ultraviolet light [18]. The typical steps for photolithography include cleaning the wafer, coating the wafer with photoresist, soft baking, aligning the wafer to a mask, exposing the wafer to UV light, and then developing the exposed photoresist. The photoresist is applied in liquid form to the wafer which is stuck on a vacuum chuck and spun at a high speed for a specific duration. The thickness of the resist is dependent on its viscosity and is inversely proportional to the square root of the spinning speed [19]. The soft bake step, a drying method, is used to improve adhesion and to remove solvent from the photoresist. After alignment to a mask, the wafer is exposed to high-intensity UV light through the openings in the mask. Any areas of

photoresist exposed to the UV light are washed away with the application of a developer. The places where the photoresist is washed away are then exposed for etching or deposition processes [19]. Following photolithography, the etching away of material, the deposition of material, or the diffusion of elements occurs. With etching, the barrier material not protected by hardened photoresist is removed. The choice of chemicals depends on the material needing to be etched. For the removal of silicon dioxide, a buffered oxide etch containing hydrofluoric acid may be used. To etch gold, aqua regia or potassium iodide may be used. The deposition of material can be done using evaporation or sputtering. With evaporation, metals are heated to the point of vaporization and then are evaporated to form a thin layer on the surface of a wafer. Sputtering is done by bombarding a target with ions. The atoms at the surface of the target are knocked loose and are transported and deposited on the surface of the wafer [19]. The surface micromachining steps are repeated until the desired device is complete.

2.3.1 Fixed-Fixed Beam Structure

The design of the microswitch is modeled by a fixed-fixed beam to be used as an actuator which is shown in Figure 7. During actuation of an electrostatic switch, there is an electrostatic force and a mechanical restoring force that oppose each other and act on the switch. Once the electrostatic force, which is a function of the applied voltage, overcomes the restoring force, the switch closes. The switch is opened when the applied voltage is removed and the restoring force overcomes the adhesion between contacts [3]. The expression for the electrostatic force for a MEMS switch is:

$$F_e = \frac{1}{2}\frac{\varepsilon A V^2}{g^2} \tag{29}$$

where V is the applied voltage, g is the gap between the switch, ε is the permittivity of the medium the switch is contained in, and A is the area that the switch overlaps. The mechanical restoring force is due to the spring effect of the switch and is given by:

$$F_r = k(g_0 - g) \tag{30}$$

Where k is the mechanical spring constant and g_0 is the initial gap between electrodes without voltage applied. The point of instability is found when the sum of the two forces is equal to zero. The voltage as a function of the gap is determined to be at maximum at $g = 2g_0/3$. When this is substituted into Equation 29, the pull-in voltage is derived by:

$$V_{pull-in} = \sqrt{\frac{8\,kg_0^3}{27\varepsilon A}} \tag{31}$$

Figure 7 shows how the fixed-fixed beam can be modeled. A concentrated load is placed at the midpoint while the ends are fixed. Due to beam symmetry and the force being in the vertical direction, the moments on either end of the beam are:

$$M = \frac{Fx}{2} - M_1 \qquad (0 \leq x \leq \frac{L}{2}). \tag{32}$$

The relationship between the moment M, Young's modulus E, Inertia I, and the rate of change for the deflection $\ddot{\delta}$, are given by Mohr's theorems [8].

$$EI\ddot{\delta} = M = \frac{Fx}{2} - M_1 \qquad (0 \leq x \leq \frac{L}{2}). \tag{33}$$

Equation 33 is integrated twice to obtain the deflection:

$$EI\delta = \frac{Fx^3}{12} - \frac{M_1x^2}{2} + C_1x + C_2 \qquad (0 \leq x \leq \frac{L}{2}). \tag{34}$$

Due to boundary conditions and symmetry, the constants of integration are equal to zero and also reveal:

$$C_1 = C_2 = 0 \tag{35}$$

$$M_1 = \frac{FL}{8} = M_2 \tag{36}$$

After substitution, the deflection equation becomes:

$$\delta = \frac{Fx^2}{48EI}(EL - 4x) \qquad (0 \leq x \leq \frac{L}{2}). \tag{37}$$

The maximum deflection occurs when x = $\frac{L}{2}$:

$$\delta = \frac{FL^3}{192EI} \tag{38}$$

The moment of inertia is given by:

$$I = \frac{wt^3}{12} \tag{39}$$

where *w* is the width of the beam and *t* is the thickness [8].

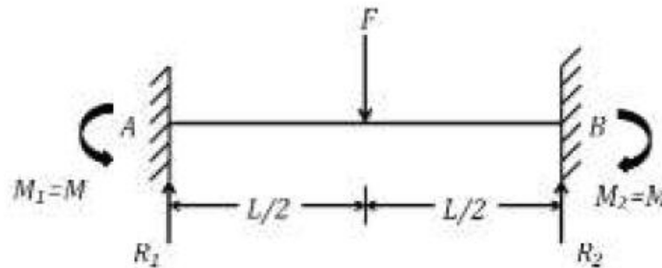

Figure 7. Modeling of a fixed-fixed beam [8].

The fixed-fixed beam micro-contact structure is created using surface micromachining processes shown in Figure 8. This process was previously used by Stilson and Laurvick for their research on micro-contacts [6], [8]. It starts with a clean silicon substrate (a) that has a layer of nitride deposited using PECVD on top which acts as an electrical isolation layer and can be used to create 3-D surfaces with grayscale lithography (b). To prepare the wafer for grayscale lithography, 1818 photoresist is spun onto the wafer. The wafer then undergoes mask writing with a laser followed by RIE to transfer the design of the photoresist to the nitride layer. This creates 3-D surfaces on the wafer that from the basis for the bottom contacts. Next, a layer of SF-11 (c) and 1818 photoresist are spun onto the surface of the wafer (d). The 1818 photoresist is used as a mask for the patterning of the SF-11 photoresist. In (e), the wafer is exposed to ultraviolet light for patterning and then is developed to remove the exposed 1818 photoresist. In (f), the exposed SF-11 is patterned with deep ultraviolet light and then is developed to remove the exposed areas. Next, a gold layer is deposited in (g) and then lifted off in places where it is on top of the photoresist which is then removed. The remaining gold layer forms the bottom metal contact of the fixed-fixed beam micro-contact structure as shown in (h).

The remaining steps form the top contact and the fixed-fixed beam part of the structure. In (i) two layers of SF-11 and 1818 are deposited. The 1818 is then patterned with ultraviolet light in (j) and then developed in (k). The SF-11 is then exposed to deep ultraviolet light and then developed away in (l). The 1818 is removed in (m) and is replaced with fresh 1818 in (n) to pattern the micro-contact bump. The 1818 undergoes UV exposure in (o) and is then developed in (p) to create the micro-contact bump on the

underside. In (q), the 1818 is removed and a layer of gold is sputtered in (r) for electroplating in later steps. During this step, another metal can be deposited instead of gold to coat the bottom contact. AZ 5214 photoresist is applied in (s), exposed in (t), then developed in (u) to prepare for electroplating. The gold undergoes electroplating in (v). The AZ 5214 is removed in (w) once the desired amount of gold is electroplated. Next, the device undergoes a gold etch to remove unnecessary metal in (x). Finally, the device is released in (y) by removing the sacrificial SF-11 [8]. The process follower containing specific instructions for creating these devices containing micro-contacts with 3-D surfaces is found in Appendix B.

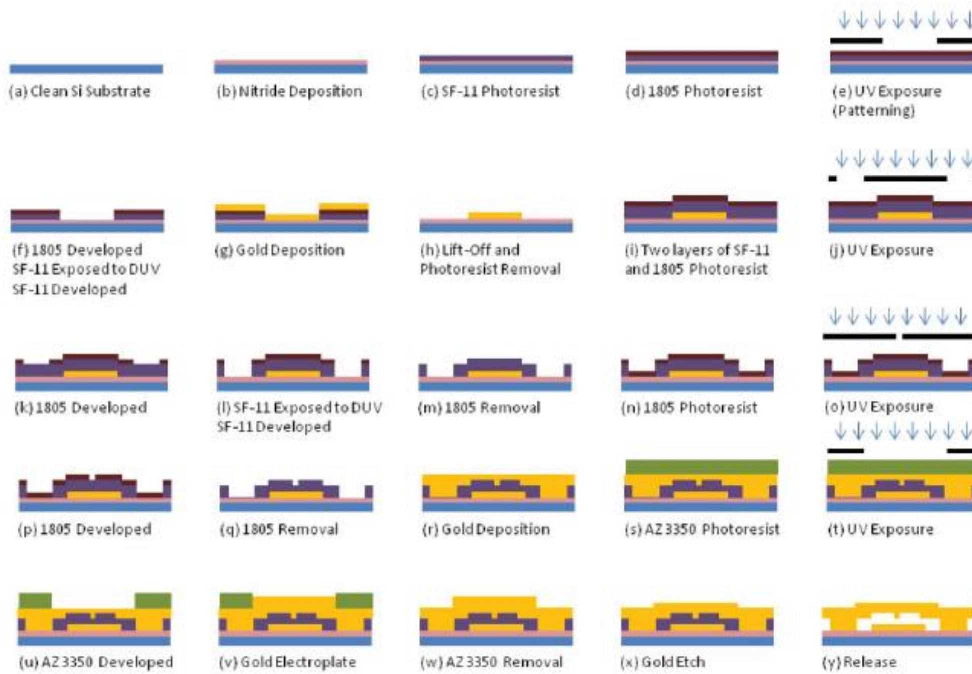

Figure 8. Process to create fixed-fixed beam structures using surface micromachining techniques [8].

2.3.2 Grayscale Lithography

Grayscale lithography is a useful technology to create 3-dimensional MEMS structures. In traditional photolithography, there is a binary exposure of photoresist where certain areas remain after exposure and development while others are developed away. With grayscale lithography, the fabrication of 3-dimensional microstructures is possible by exposing photoresist to a range of varying ultraviolet dosages in a single photolithography step without the use of a mask [20], [21]. With a single exposure process, grayscale lithography does not suffer from potential alignment errors created from using multiple masks and is more time efficient [21]. Following the UV exposure, the structures undergo plasma-based dry etching which transfers the design from the photoresist to the layer underneath [13]. For this research, the photoresist design is transferred to a silicon nitride layer with a height of approximately 1 μm using a Reactive Ion Etching (RIE) machine. When a smooth surface profile is required, the photo-resist can be re-flowed for a few minutes [22]. To generate the grayscale masks, several methods have been designed to automate the process. Loomis *et al.* started by creating a 3-D structure in computer-aided design (CAD) software and then exporting the design to a stereolithography (STL) file. Next, the sample structure is sliced into layers and a 2-D plane is generated above the structure where each layer is projected onto the plane which creates a topographic map of the structure. A N x M array is overlaid on the projection plane which is then converted into a drawing exchange format (DXF) file and is used to generate the grayscale mask by direct writing with a laser pattern generator directly onto a wafer covered in photoresist [21]. An alternate method of generating masks was created by Laurvick and Coutu using the Heidelberg Mask Writers available at AFIT.

The first step is to characterize the power levels and duty cycles necessary to create the desired exposure. Next, CAD files are created for each level of exposure and are stored in the Heidelberg system as seen in Figure 9. A script file is then executed to produce the grayscale mask with the Heidelberg mask writer [23]. This is the method used to create 3-D surfaces for bottom contacts in this research. Two-dimensional pyramids have been created for previous research using grayscale lithography and are shown with an SEM image in Figure 10 [8].

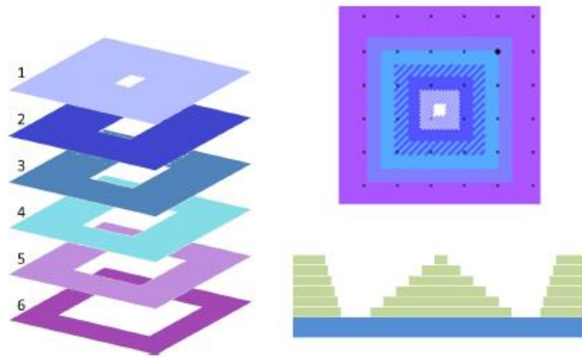

Figure 9. CAD designs used for different exposure amounts [23].

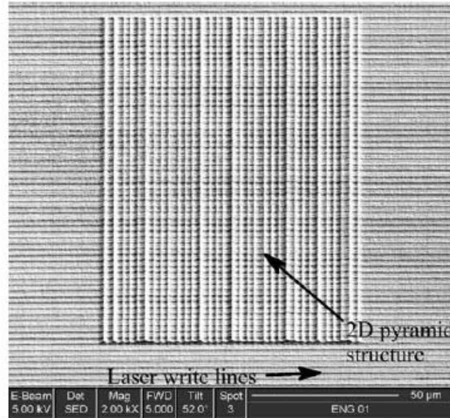

Figure 10. 2D pyramid structures created using grayscale lithography and RIE [8].

2.4 Micro-contact Causes of Failure

There are many different causes of failure for micro-contacts, including stiction, fretting, and material transfer. A failure mechanism is defined as the actual physical phenomenon behind a failure occurrence [24]. Understanding the various failure mechanisms and why they occur is important to reduce their effects and create micro-contacts that are capable of lasting for billions of switching cycles. Different causes of failure are dependent on a switch undergoing cold or hot switching. Cold switching is when an electrical signal is applied only when the switch is fully closed. Hot switching is when the signal is applied while the switch is being opened and closed [5]. Leading edge hot switching occurs when the signal is applied as the switch closes while trailing edge hot switching refers to the application of the signal when the switch opens. With cold switching, there are two types of contact failure: stuck-open failure and stuck-closed failure. Stuck-open failure occurs when the contact resistance of the switch becomes too

high to function properly and is usually caused by contamination or wear. Stuck-closed failure occurs after the switch remains permanently in the closed state, even without the application of an actuation voltage. This failure is typically caused by stiction, welding, or bridge transfer. With hot switching, there are four categories of material transfer mechanisms known to cause damage to switches: field evaporation, field emission, arc transfer, and ohmic heating/bridge transfer [5]. It has been suggested that materials with a higher melting and boiling point are an ideal contact material because all damage mechanisms except for field evaporation are either directly or indirectly related to melting and boiling of the contact material [3].

2.4.1 Stiction

Stiction is when two surfaces come into contact and stick together due to their atomic bonds. Stiction occurs when the adhesion force in the contact is greater than the restoring force of the actuator which prevents the switch from opening even in the absence of an actuation voltage [3]. This failure mode is caused by capillary, electrostatic, and chemical and van der Waals forces. Stiction generally occurs to switches undergoing cold switching and is a form of stuck-closed failure. It is described by the Hertz, Johnson-Kendall- Roberts (JKR), or Derjaguin-Muller-Toporov (DMT) models. A model developed by Wu *et al.* is used to predict stiction due to van der Waal Forces [8]. An example of stiction causing the failure of a cantilever beam is shown in Figure 11.

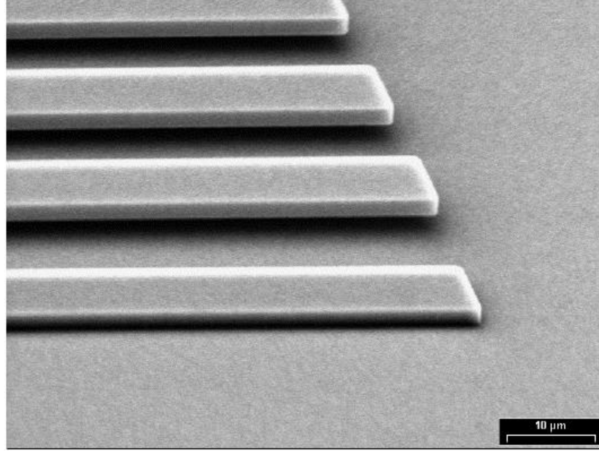

Figure 11. SEM image showing the stiction failure of the bottommost cantilever beam [25].

2.4.2 Fretting

Fretting is another cold switch failure that is a form of structural fatigue defined as accelerated surface damage at the interface of contacting materials subjected to small oscillatory movements [24]. Two basic conditions necessary for fretting to occur are relative moment or slip and amplitude of motion sufficient enough to cause damage. It has been shown that amplitudes as small as hundreds of nanometers are capable of producing fretting. The minimum slip amplitude for fretting to occur is given by:

$$\delta = \frac{[3(2-v)(1+v)]}{8Ea}\mu P[1-(1-\frac{T}{\mu P})^{\frac{2}{3}}] \tag{40}$$

where a is the diameter of the outer contact radius, E is the Young's Modulus, v is the Poisson's ratio, P is the normal force, μ is the static coefficient of friction between the contact surfaces, and T is the tangential force.

While there is no complete consensus on the mechanisms of fretting, there are several processes that are present. The disruption of the oxide film on the surface by the mechanical action exposes clean and strained metal which reacts with the environment and rapidly oxidizes. There is the removal of material from the surfaces by adhesion wear, delamination or by shearing the microwelds formed between the asperities of the contact surfaces when the contact is made. There is oxidation of the wear debris and formation of hard abrasive particles that will continue to damage the surfaces by plowing. Another process is the formation of a thick insulating layer of oxides and wear debris between the contacting surfaces. Another observation on fretting is that as contact force increases, the contact resistance decreases until the insulating layer forms from wear debris and the formation of an oxide [24]. An example of fretting is shown in Figure 12.

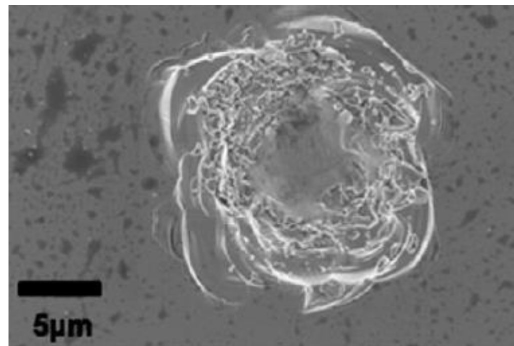

Figure 12. SEM image showing fretting wear scars [26].

2.4.3 Material Transfer and Electromigration

The transfer of material between surfaces is a serious issue affecting micro-contacts. Electromigration is one of the forms of material transfer that causes device failure. It is defined as “the forced motion of metal ions under the influence of an electric field” which causes voids to occur that ultimately cause device failure [27]. The damage

caused by electromigration can be severe enough that noticeable physical damage can be observed using a scanning electron microscope [28]. The migration occurs predominantly via grain boundaries which lead to voids and extrusions near the grain boundary triple points and failure of the device. As a result of electromigration, small mounds or voids form that eventually coalesce and grow leading to failure. As active elements on chips become smaller and the connecting stripes made narrower, there is an increase in current density which has a greater potential for electromigration induced failure. Due to the small size of a-spots, the current density can be substantial which creates favorable conditions for electromigration to occur. For DC conditions, the high current densities found in the contact spots were shown to cause a net mass transport by electromigration parallel to the electron flow. Atoms migrated out of the cathode and into the anode, leaving behind vacancies and voids that clustered to crevices and cracks and yielded an asymmetric fracture characteristic. Under AC conditions, the conditions are symmetric and cracks are found inside both electrodes. The observed fracture features were attributed to the cyclic mechanical stress and strain induced by thermal expansion and contraction in the contact spot region [24].

The mechanical transfer of material through adhesion and cold welding appears during low voltage hot switching. It is hypothesized that when the contact temperature is not high enough to cause melting, but high enough for softening, material scatter can be expected. Higher contact temperatures at the point of initial contact can cause contact melting which can also lead to material transfer [3]. Results from Basu and Hennessy's research suggest that there are at least two mechanisms that lead to material transfer during hot switching of devices. The first mechanism is polarity driven and independent

of contact closure rate. This mechanism was observed for leading-edge DC hot switching. The second mechanism was also polarity driven but depended on the contact separation rate. This was observed in trailing-edge DC hot switching. The amount of material transfer was shown to increase as the contact opens at a slower rate [4]. An example of material transferring from a micro-contact resulting in a void is shown in Figure 13.

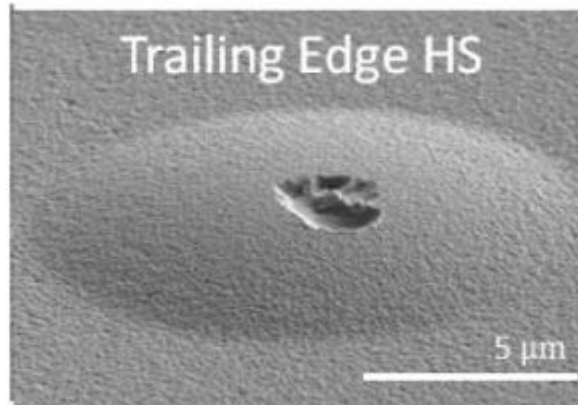

Figure 13. SEM image of a Ruthenium micro-contact after undergoing trailing edge hot switching showing a void caused by material transfer [4].

2.4.4 Field evaporation

Field evaporation is the removal of a surface molecule, such as an ion, by a strong local electrical field [5]. The material transfer direction is dependent on the orientation of the electric field as well as the type of material. The transfer takes place from anode to cathode and occurs when there is a separation on the order of a few angstroms. The small separation allows the electrons to tunnel from one surface to another [3].

2.4.5 Surface Contamination

Surface contamination negatively affects MEMS contacts by physically separating the conductive electrode surfaces. Unless under an ultra-high vacuum, there

will be some amount of surface contamination present on MEMS contact surfaces. A contact showing an increased contact resistance as well as a decrease in the pull-off force suggests that the surfaces are becoming covered with a nonmetallic species that inhibits electrical conduction and decreases the adherence of the contacts. A sudden and large increase in the contact resistance can be an indicator that a contact has been completely covered and has reached a critical contamination threshold [29]. When surface contamination causes failure, a frictional polymer appears on a circular perimeter below the contacting surface of a microcontact. An explanation for this is that when the contacts are rubbed against each other, the layers adjoining the contact surfaces experience shear which produces charged radical ions. The radical ions react with organics present in the atmosphere which create the frictional polymer. This frictional polymer formation is an important issue in the platinum-group metals such as Pt, Pd, Ru, and Rh [3]. An example of frictional polymer formation on a micro-contact is shown in Figure 14.

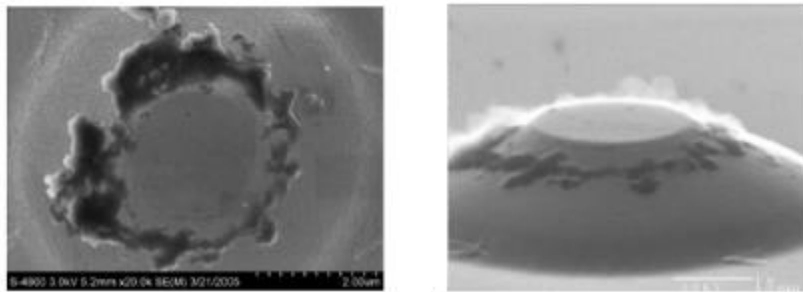

Figure 14. SEM images showing frictional polymer formation on a Ruthenium contact where the polymer appears from the surface adjoining the contact site [3].

2.4.6 Molten Metal Bridge

During hot-switching, molten metal bridge (MMB) phenomena are common. When contacts experience greater than 1 V, the melting voltage for many metals is reached causing MMB phenomena. Immediately prior to contact opening, the reduction in contact area results in a constriction of current flow lines, an increase in Joule heating at the a-spots and the formation of a microscale MMB. This results in the transfer of molten contact material between contacts. An MMB event can be described by the transient voltage waveform just before the contact opening. A second waveform observed by Bull and McBride is an abrupt and instantaneous rise in contact potential to the full open circuit voltage which they termed a "delamination" type. The delamination event is linked to a greater surface roughness change than the MMB event. Delamination events result from the cold welding of the Au layers, and the subsequent tearing of the surface. A toroidal wear scar is a sign that delamination occurred and is significant because the maximum current density occurs at the edges of the contact region. Bull and McBride observed that delamination events cause a higher level of damage to an Au film while MMB events correlated to decreased damage, film smoothing, and possibly the repair of the film [30].

2.4.7 Corrosion

Corrosion is a chemical or electrochemical reaction between a metallic component and the surrounding environment causing detectable changes that lead to a deterioration of the component. It begins at an exposed metal surface and degradation initiates with the formation of a corrosion product layer. The degradation continues as long as at least one of the reactants can diffuse through the layer and sustain the reaction. There are many different types of corrosion that can affect MEMS devices. Atmospheric

corrosion is the gradual degradation of a material by contact with substances present in the atmosphere. The rate of atmospheric corrosion is dependent on the humidity, temperature, and levels of atmospheric pollutants. Localized corrosion is very similar to the general form of corrosion except that the rate of attack is usually faster and the affected area is smaller. Specific forms of localized corrosion include crevice, pitting, and biological. Creep corrosion is another form that can occur when a reactive substrate metal like copper is located next to and in physical contact with a noble metal or a noble alloy such as gold. The substrate metal corrosion products creep over the noble metal surface. It can also be initiated from the pores in thin gold plating. Galvanic corrosion occurs when a metal or alloy is electrically coupled to a more noble metal. Whenever dissimilar metals are coupled in the presence of a solution containing ionized salts, galvanic corrosion occurs. The requirements for galvanic corrosion are materials with different surface potentials, a common electrolyte, and a common electrical path. The more active metal becomes anodic and corrosion occurs while the less active metal becomes cathodic [24].

2.5 Micro-contact Reliability

The usefulness and life expectancy of a device can be expressed by a "bathtub" reliability curve as shown in Figure 15. There is a high probability of failure in the first cycles of operation which is called the break-in period or wear-in period. This is usually caused by manufacturing or installation problems. Following the break-in period, the probability of failure is low for an extended period until it increases sharply at the end of the device's lifetime, which is known as the wear-out period. A probabilistic approach

can be used to determine the useful life of electrical components which reflects the uncertainty in its reliability [24]. Reliability can be defined as the probability of a component to perform its designed function over the period of time under operating conditions as given by:

$$R(t) = 1 - F(t) = e^{-\lambda t} \quad (41)$$

where λ is the failure rate and t is the operating time. $F(t)$ is called the probability of failure and is defined as:

$$F(t) = 1 - e^{-\lambda t} \quad (42)$$

The probability density function, provided the random variable is time to failure is defined as:

$$f(t) = dR(t)/dt \quad (43)$$

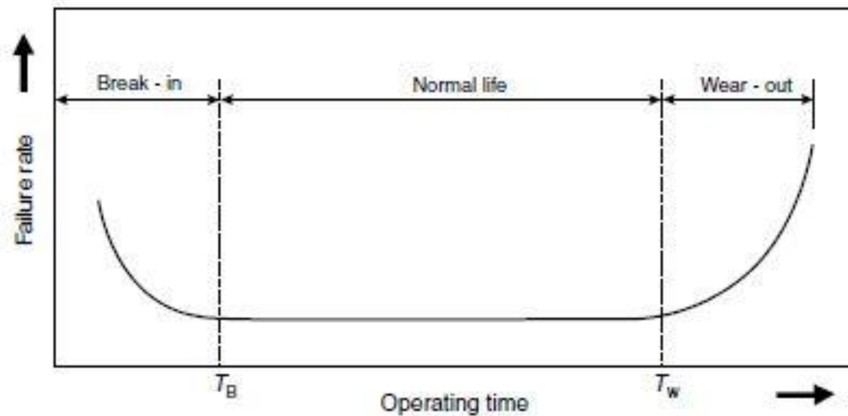

Figure 15. "Bathtub" reliability curve to model the failure rate of devices [24].

2.5.1 Contact Materials

The choice of contact materials is an important decision when designing micro-contacts. Metals are selected for various characteristics, such as their hardness, conductivity, susceptibility to oxidation or polymer formation, melting temperature and other material features. They may also be selected to avoid the effects of common failure mechanisms. Gold is a common choice for micro-contacts due to its strong resistance to oxidation, relatively high conductivity, and low material hardness. A low hardness enables reasonable micro-switch performance with low contact forces [31]. Arrazzat *et al.* showed that the shallow implantation of boron and nitrogen on thin films of gold increased their surface hardness while not having a significant impact on the contact resistance [32]. Silver is also resistant to oxidation but reacts with any amount of hydrogen sulfide and other gaseous forms of sulfur. This results in tarnish which is non-conductive and makes silver a poor choice for a MEMS micro-contact. The use of metal alloys is a common method to avoid unwanted oxidation [6]. Coutu *et al.* alloyed gold with Platinum (Pt) and Palladium (Pd) which was shown to reduce contact resistance and to extend their lifetime. Ruthenium (Ru) contacts treated in oxygen plasma also show excellent contact properties. Ru contacts with a layer of RuO2 were shown to have less susceptibility to contamination and lower adhesion. It has also been observed that RuO2-Au contacts have an increased lifetime compared to MEMS switches using Pt-Au, Ir-Au, and Au-Au as contact materials [11]. Another possible candidate for MEMS contact surfaces is Tungsten (W), which has a very high melting point at 3422 C when compared to Pt and Ru and has a suitable hardness for MEMS switches. The issue keeping W from being used as a contact material is its rate of oxidation which leads to reliability issues. A

possible solution for using W as a contact material is to package switches in a pressurized nitrogen environment [3].

2.5.2 Micro Bounce Phenomena

Contact bounces are an undesirable phenomenon that can affect the lifetime and reliability of MEMS switches. They generally result from the collision of the mobile contact part to the fixed contact part. When a contact bounce occurs, the closing time of the switch increases and the impact on metal surfaces can lead to wear or other mechanical degradations. Micro-contact bounce theory is different from classical bounce theory due to the small gap distance that enhances the relative influence of forces, such as electrostatic forces, that are negligible at the macroscopic level [33]. Peschot *et al.* came up with five steps to explain the occurrence of a contact bounce:

1. At the initial stage, the beam is in equilibrium between the actuation force and the restoring force.
2. When the distance between the two contacts reaches the critical distance, the equilibrium state is reached and the electrostatic force equals the restoring force. As the distance decreases, the mobile electrode is attracted towards the fixed contact.
3. When the contact is closed, voltage across the two contact parts and the electrostatic force rapidly decrease down to nearly zero. The restoring force of the beam is at its maximum and competes with the adhesion force.
4. Once the restoring force of the beam is higher than adhesion force, the mobile part is repulsed from the surface and the contact opens.

5. As the mobile part moves away, a differential potential is generated across the contact and the electrostatic force increases until it overcomes the restoring force. The mobile part is then attracted toward the fixed part leading to the closing of the contact. The contact is definitively closed when the restoring force and the actuation force prevent the contact from reopening.

2.5.3 Circuit Protection

The polarity of a DC load applied to a micro-contact can be critical to its reliability. Additionally, material transfer due to electromigration can be induced under low-frequency AC loads. Damage during leading edge hot-switching was due to transient charge on the contacting surface. During contact closure, this charge leads to regions of extremely high current density followed by contact closure over the weakened material. The charge is a result of the capacitive nature that a pair of contacts have prior to closure. In trailing edge hot-switching, potential damage occurs from the transient current flowing through a contact, which attempts to continue to flow after the contact begins to open. This can lead to regions of extremely high current density which is a form of inductance. Both effects can be mitigated with the application of external circuitry that reduces their capacitive or inductive effects. The most stable damage mitigating external circuit was determined to be a series RC configuration [28].

2.6 Test Fixture

The test stand used for characterizing the performance over the lifetime of a micro-contact utilized in this research has been developed and modified by Toler, Stilson,

and Laurvick. The test stand consists of a nitrogen environment which reduces the opportunity for oxides and other organic films to develop prematurely and is used to simulate a hermetic environment a micro-contact would normally operate in. A FemtoTools FT-5270 force sensor is used to determine the amount of force applied to the micro-contact test structure. A Thorlabs BPC301 piezo motor and controller is used to apply force to the micro-contact and to actuate the sensor towards the support structure. There are micro-manipulators in the x, y, and z planes to align the force sensor with the micro-contact support structure. The test fixture is a fabricated device on a diced wafer that is attached to a carrier using crystal bonder and then wire bonded to the breakouts of the carrier. The carrier is placed into a carrier socket which has pins for every wire bond. The pins facilitate voltage and current measurements to determine the contact resistance. The use of the carrier and the micro-manipulators reduces the probability of physically interacting with and changing the surface of the devices and eliminates the necessity of probes. During Stilson's research, several upgrades were done to improve the test stand. The previous research showed that the minimum contact value was around 0.2 Ω which was thought to be due to the measurement floor of the Agilent equipment. The equipment was upgraded to National Instrument (NI) devices which allow for the integration between NI and LabVIEW software. New NI equipment was bought for this upgrade. A NI-4070 digital multimeter which is used to measure the voltage across the contact with a resolution of 1 μV. A NI-4072 digital multimeter that measures current with a resolution of 10 nA. Two NI-5402 arbitrary function generators were purchased. One drives the piezoelectric actuator during cycle testing while the other drives the signal across the

micro-contact during cycling. The last apparatus purchased was a NI-4110 programmable DC power supply which applies potential across the micro-contact [8], [34].

Laurvick utilized the test stand after Stilson and further improved on its capabilities. A ThorLab PAZ005 piezoelectric actuator was installed which is capable of oscillating at 2 kHz. The software was upgraded as well. With Toler's research, the test stand was originally designed to conduct a single initial contact cycle in which the probe tip slowly approaches the device until either a safety limit is reached or a force is measured. If a force is measured, the probe tip advances while continually recording position and force until the current and voltage change which indicates electrical contact of the beam to the bottom contact was made. The point of electrical contact is marked and the probe continues until a preset contact force is reached. The force and position are still recorded as well as the current through and the voltage across the contact. During Stilson's research, the software performed this measure process semi-automatically, with contact cycling added. This process involves the cycling of the piezo-actuator synchronized with the application and removal of a 1 V DC load to the contact during the closed portion of the cycle. While this was being done, the current, voltage, force, and position were all measured and recorded simultaneously. This process continued until contact failure is detected, a number of cycles is reached or a hardware error occurs. Laurvick modified the software to reduce the likelihood of error during operation by removing unused code and simplifying the graphical user interface. Laurvick also improved upon the automation controls during long periods of testing. It is now possible to specify the starting and ending number of cycles to test between, the number of test points per decade, the number of measurements per test point, and settings to allow for

lower frequencies early in testing and higher frequencies for sufficiently large number of cycles. For a single test cycle, a file is produced which contains current, voltage, calculated contact resistance, displacement and the absolute and relative contact force. After each cycle, a new file is created for each test point taken with an increment index in the filename [6], [35]. The test stand during Laurvick's research is shown in Figure 16.

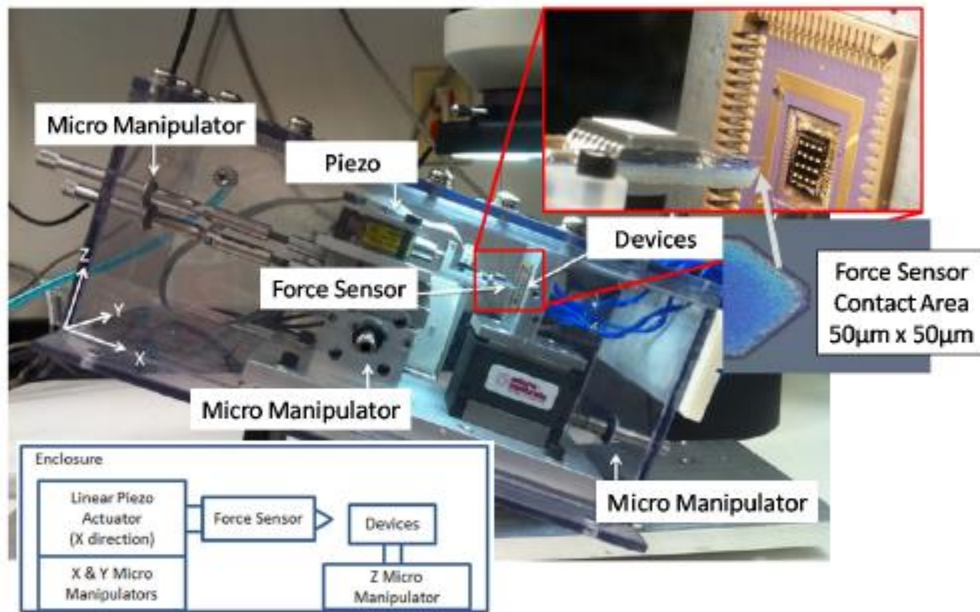

Figure 16. Test stand for testing micro-contacts [6].

2.7 Chapter Summary

This chapter discussed relevant literature concerning micro-contacts and MEMS fabrication techniques to be used in this research. Understanding the modeling of the contact resistance of micro-contacts as well as the method of fabricating the contacts and fixed-fixed beam support structure is important for designing micro-contacts that can perform in the ballistic electron transport region. This chapter went over contact

resistance modeling, surface micromachining, failure mechanisms, the selection of contact materials and the test stand equipment used during experiments.

III. Methodology

3.1 Chapter Overview

The purpose of this chapter is to describe the research methodology used to design, test, and analyze the performance of micro-contacts. The methodology will discuss the fabrication of the micro-contacts, the characterization of grayscale lithography, design of experiments, resistance modeling, and the post-test inspections performed after testing.

3.2 Micro-contact Fabrication

The micro-contacts are fabricated using the surface micromachining MEMS techniques mentioned previously in section 2.3.1 and are explicitly listed out in the process followers found in Appendix B. The start of fabrication begins with a silicon wafer with a layer of silicon nitride deposited on top. In order to use grayscale designs for bottom contacts, the second mask mentioned in the research done by Stilson and Laurvick is not used. As a first step, the wafer has S1818 photoresist spun on for 30 seconds at 4000 RPM to create a 2 μm layer which is then soft baked. This wafer then is placed on the Heidelberg mask writer where the grayscale designs are direct written into the wafer. Following the development of the photoresist, the wafer is placed into the Trion RIE and undergoes RIE to transfer features from the photoresist to the substrate. These transferred designs make up the unique 3-D surface features for the bottom contacts of the microswitches. Following the RIE, the remaining photoresist is removed with acetone and the wafer undergoes the rest of the steps in the process follower to create the fixed-fixed beams and the upper contact bump. The design of the beam is

shown in Figure 17 with its dimensions labeled. After completing the steps found in the process follower, the wafer is diced and the chips are mounted to carriers and wire bonded for use with the test stand.

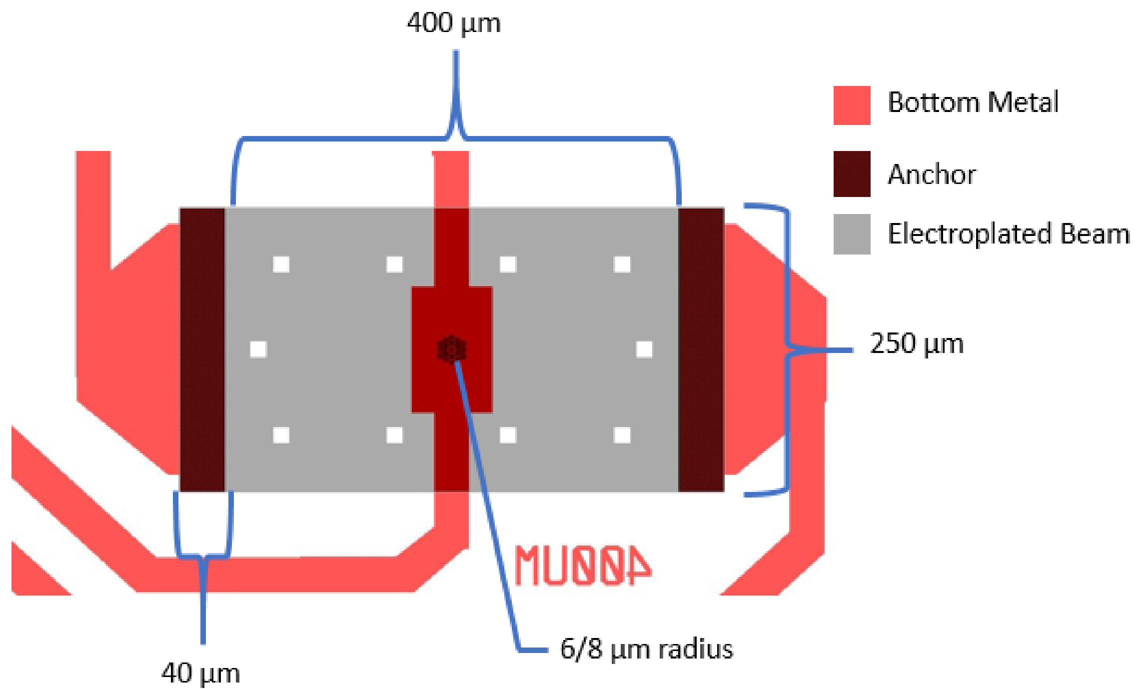

Figure 17. Design of the fixed-fixed beam created using L-Edit software with its dimensions labeled. There is a 3 µm gap between the electroplated beam and the bottom metal.

3.3 Grayscale Lithography

Since the last characterization of grayscale lithography on S1818 photoresist at AFIT, there have been differences in the expected photoresist heights due to degradation of the Heidelberg mask writer's laser. In order to accurately predict the contact area of the micro-contact and create linear step heights, it is desired to characterize the grayscale

lithography by adjusting the power and duty cycle of the laser. A square pyramid featuring 6 distinct step heights was created in L-Edit software and was repeated numerous times with varying laser power and duty cycle with the direct write capabilities of the Heidelberg mask writer. The laser power started at 50 mW up to 120 mW in 5 mW increments and used duty cycles of 50, 60, 70, 80 and 90 for each level of the pyramid. After writing, the wafer was developed with 351 developer and the photoresist step heights were measured using the Tencor profilometer. The best duty cycle and power were picked to make 3 level and 6 level micro-contacts based on the measurements. The settings shown in Table 1 were used throughout the research to create 3 level micro-contacts.

Table 1. Settings used to create grayscale micro-contacts with the Heidelberg Mask Writer.

Level	Laser Power (mW)	Duty Cycle	Depth (μm)
Top (No laser used)	0	0	0
Middle	65	50	0.77
Bottom	65	90	1.31

RIE characterization was done to see if the formulas from previous research could be used again. RIE combines the plasma and sputter etching processes and is anisotropic. Plasma systems are used to ionize reactive gases and the ions are accelerated to bombard the surface. Etching occurs through a combination of the chemical reaction and the momentum transfer from the etching species [19]. It is desired to have a formula that gives a selectivity of 1 which etches the photoresist and the silicon nitride at the same rate. This transfers unaltered features from the developed photoresist into the substrate. The previous formula that gave a selectivity of 1 used 26 sccm of O_2 and 45 sccm of CF_4

for 90 seconds. Figure 18 shows several of the measurements that determine the selectivity. The thickness of the photoresist, denoted *a* in Figure 18 is found from the spin speed and the duration of the spin. The height difference between the photoresist and the nitride, denoted *b*, is found using a profilometer after RIE is done but before the remaining photoresist is removed with acetone. The amount of nitride removed, denoted *c*, is found using a profilometer after the remaining photoresist is removed with acetone. Together, these three measurements allow the selectivity to be calculated using Equation 44.

$$Selectivity = \frac{Nitride}{Photoresist} = \frac{c}{a - (b - c)} \tag{44}$$

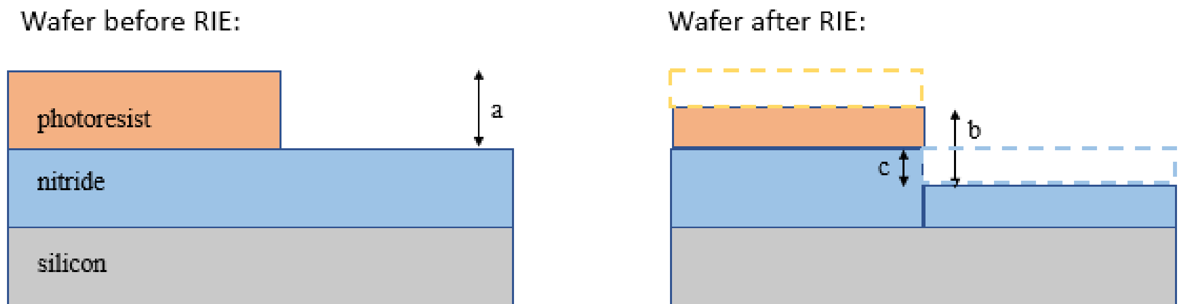

Figure 18. Cross section of a wafer to determine the selectivity.

3.4 Design of Experiments

3.4.1 Factor Selection

The design of experiments was planned in order to use statistics to determine if certain factors are significant to have micro-contacts operate within the ballistic electron

transport model. In order to create the experiment, factors needed to be picked that had a low and high value but could be either quantitative or qualitative. Additionally, these factors needed to be designable using L-Edit software or through the manipulation of the masks. Four factors were ultimately picked for the scope of the experiment, each with two possible values. The first factor, the surface area of the tallest point, was set at either 0.81 μm^2 or at 3.24 μm^2. The second factor, the shape of the tallest point was set to be either a circle or a square. The third factor was the closest distance between two of the tallest points. The minimum distance was 4 µm and the maximum distance was 6 µm. The fourth factor was the size of the contact bump that is underneath the fixed-fixed beam that makes contact with the grayscale contact. The minimum bump size radius was 6 µm and the maximum size was 8 µm. This final factor was determined by the specific chip used for experimentation as half of the chips were made with 6 µm bumps and the other half were made with 8 µm bumps.

3.4.2 Responses

With the initial experiment, there are two responses that will be observed in order to determine if any of the factors are significant. The first is the resistance of the micro-contact after 10,000 cycles. At this point, the micro-contacts will have passed the wear-in period and it will be possible to determine if the micro-contact has a resistance indicating that it is in the ballistic electron transport model. The second response is the standard deviation in the measured contact resistance which would determine whether a contact appears be stable. This is calculated from resistances measured between the 100th and millionth cycle to avoid including the wear-in period resistances in the calculation.

3.4.3 Initial Design

The initial design is a 2^4 full factorial due to having four factors resulting in 16 experimental runs for each chip created. The runs were randomly generated using Minitab software and are shown below in Figure 19. Having randomized runs makes the runs as uniform as possible and also allows for the assumption of equal variance.

StdOrder	RunOrder	Surface Area	Shape	Distance Between Points	Contact Bump Size
9	1	-1	-1	-1	1
15	2	-1	1	1	1
14	3	1	-1	1	1
8	4	1	1	1	-1
11	5	-1	1	-1	1
12	6	1	1	-1	1
2	7	1	-1	-1	-1
7	8	-1	1	1	-1
10	9	1	-1	-1	1
13	10	-1	-1	1	1
3	11	-1	1	-1	-1
6	12	1	-1	1	-1
5	13	-1	-1	1	-1
1	14	-1	-1	-1	-1
16	15	1	1	1	1
4	16	1	1	-1	-1

Figure 19. Experimental runs for the initial design.

The specifications for the design of each run were then created using L-Edit software and are shown in Figure 20. Each design fits within a 32 µm by 32 µm square and is aligned with the hemispherical bump on the underside of the beam. After data is recorded from all the runs, analysis of variance (ANOVA) will be performed using Minitab software. A factor will be determined to be significant if it has a p-value less than 0.05, meaning that the null hypothesis is rejected. It may also be desirable to perform confidence intervals as well. The residuals of this design will be checked to look

for outliers, violations of independence assumptions such as correlation, and nonconstant variance. If there is seen to be nonconstant variance, a variance stabilizing transform will be applied to have the model meet all assumptions [36].

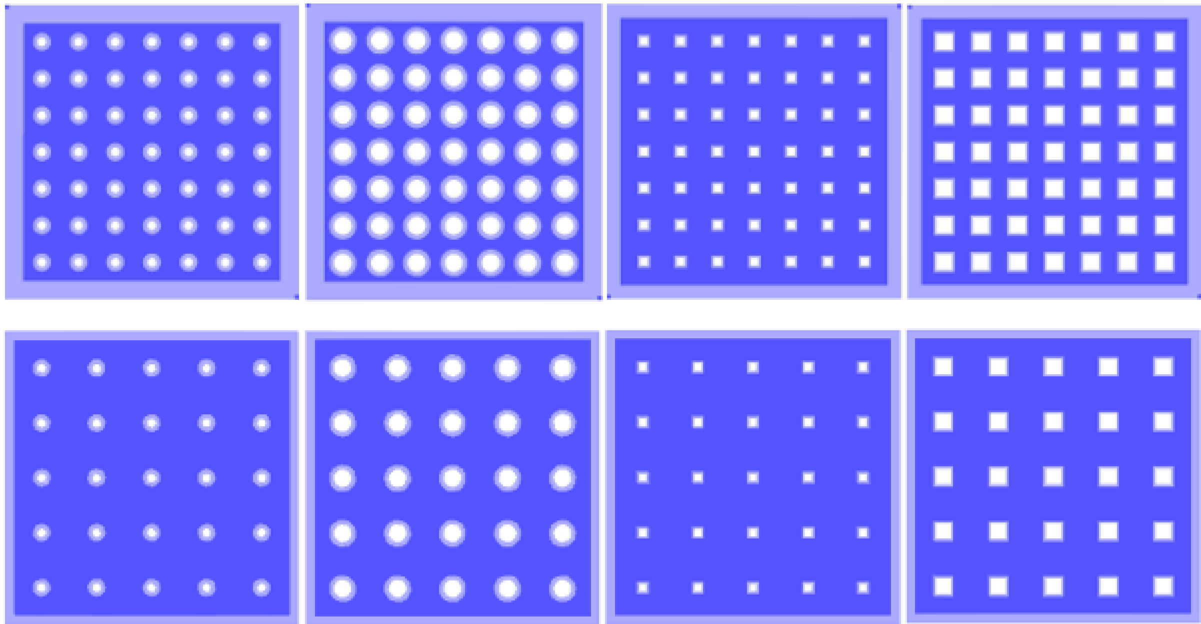

Figure 20. L-Edit designs for the 2^4 factorial experiment. Each design is 32 µm by 32 µm. The white denotes the highest point of the micro-contact and the dark blue denotes the lowest point of the contact.

3.4.4 Additional Experiments

A look into the effects of the voltage on the micro-contacts is one of the effects to be tested. While a 1 V source has been used for testing of micro-contacts in Stilson and Laurvick's research based on ease of testing, there was never any validation done to determine an optimal voltage to produce better results or to have contacts with greater

longevity. For this investigation, testing will be done to compare contacts cycled 1 million times at either 1 V or 0.5 V.

A comparison between grayscale micro-contacts and a micro-contact without any 3-D surfaces will be done as a baseline. The micro-contact with the flat bottom will be a control to determine if there is a negligible difference in the characteristics of 3-D grayscale microcontacts.

In addition to the designs for the planned factorial experiments are other designs that may show merit in extending the lifetime of grayscale contacts but do not meet the requirement of having two level factors. Additional designs include micro-contacts made of hemispherical bumps, crosses, and grids of pyramids with alternating heights. These designs are shown in Figure 21. The complete set of designs is found in Appendix C.

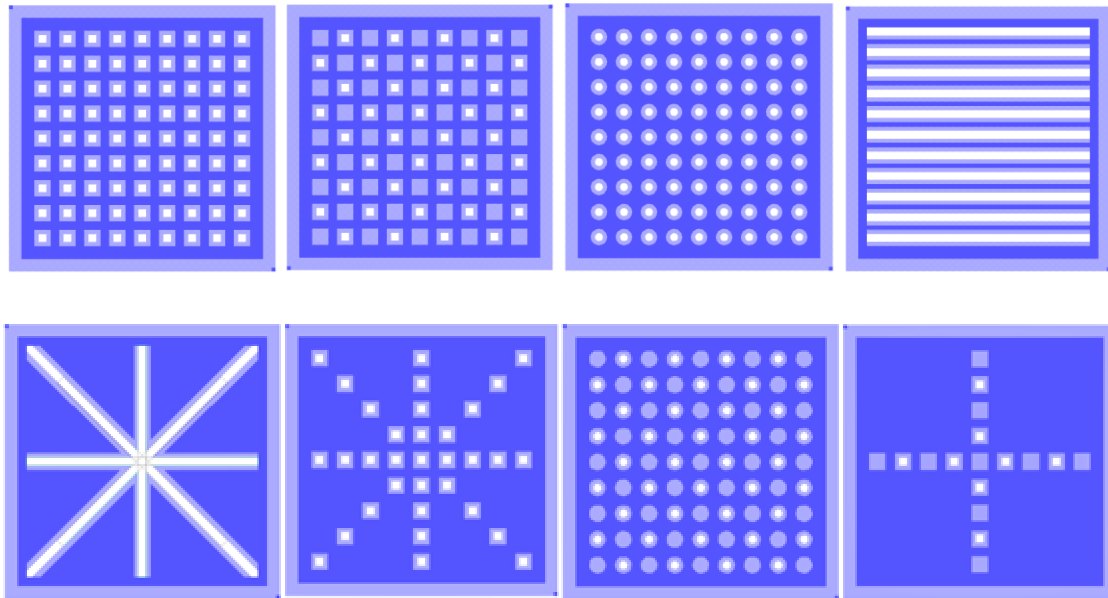

Figure 21. Additional designs created in L-Edit for fabrication and testing.

3.5 Resistance Modeling

The models for the contact resistance of the micro-contacts were created using the equations from Section 2.2 as well as previously measured values for resistivity, hardness, and the Young's modulus of gold. The resistivity, ρ, was 28.505 nΩ-m, the hardness was 2.45 GPa, and the Young's modulus was 78 GPa. The elastic and plastic model was done using Equations 11 and 12 for a 6 µm and 8 µm radius contact bump and is shown in Figure 22.

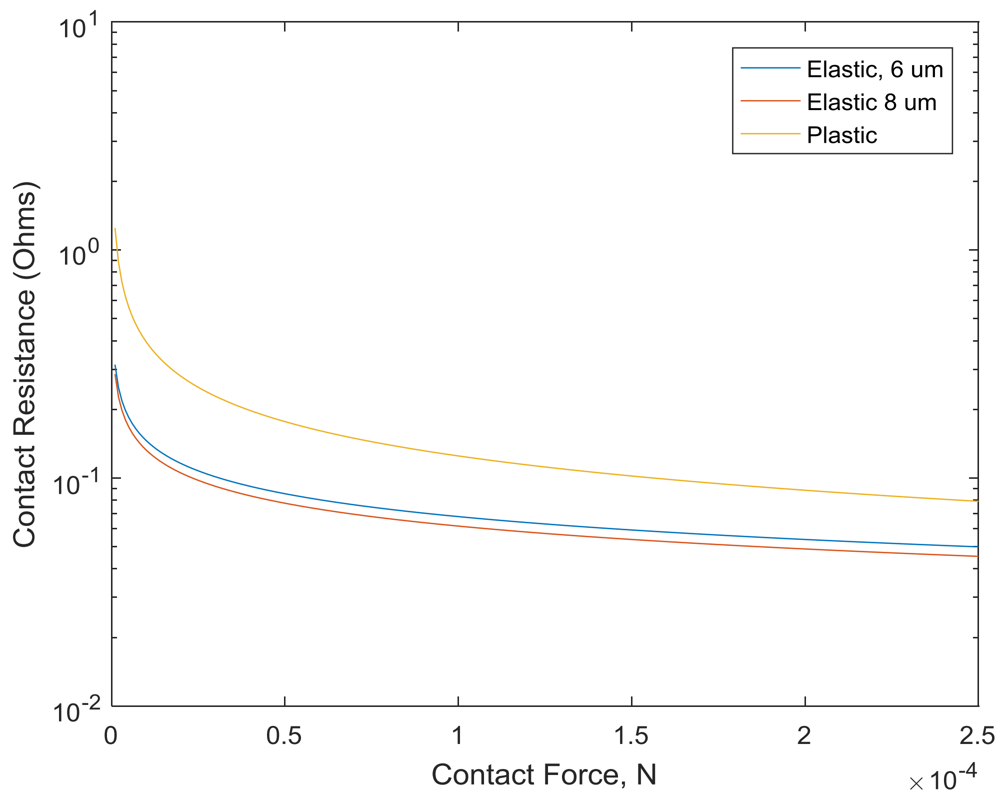

Figure 22. Contact Resistance model created with MATLAB to show the differences between contacts undergoing plastic or elastic deformation.

Incorporating the possibility of ballistic electron transport into the contact resistance model involved using Mikrajuddin *et al.*'s Gamma Function given a Knudsen number. Using this gamma function and various values for the Knudsen number, a model was created using Equations 11, 13, 14, and 15. It compares the theoretical resistance of a contact under only diffuse electron transport to a contact under only ballistic electron transport. This is shown in Figure 23. It is interesting to note that the area of the micro-contacts causes the ballistic resistance to be two orders of magnitude larger than the diffuse resistance. These models will provide a way to compare experimental data to the model in Chapter 4 [8], [11], [37].

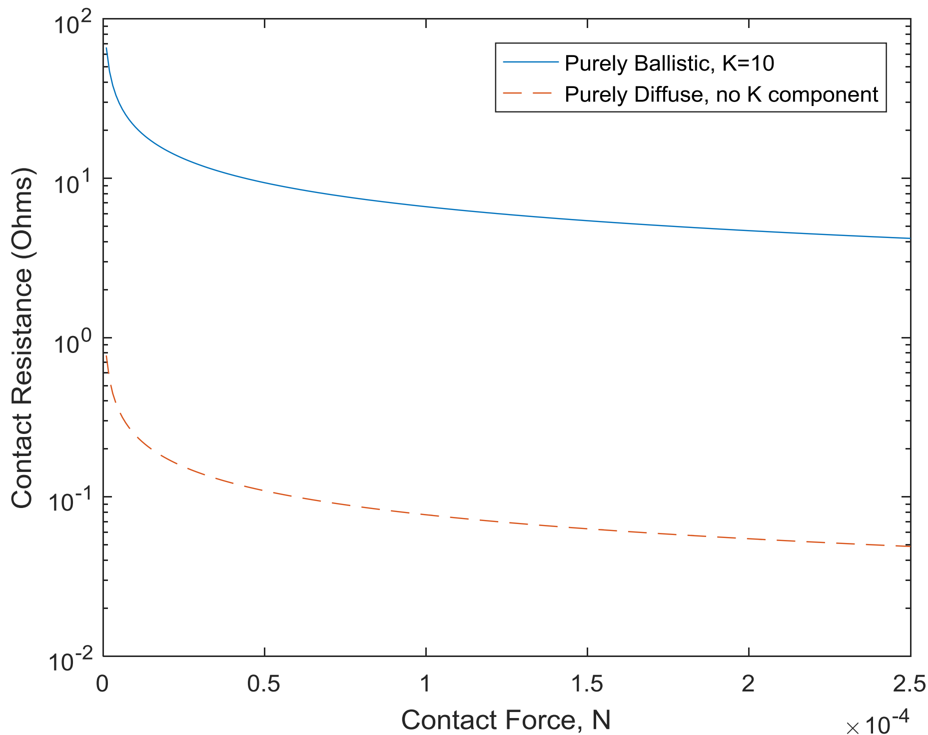

Figure 23. Contact Resistance model created with MATLAB to compare the resistance of contacts with ballistic electron transport to contacts with diffusive electron transport.

3.6 Test Stand

The test stand previously mentioned in the Literature Review is an enclosure that uses gaseous nitrogen to keep a hermetic environment for testing to reduce the incidence of thin films developing on contacts and to minimize moisture. The test stand is run with a Labview controlled National Instruments rack. It uses a NI 4070FLEXXEMM module which measures currents and voltages. These currents and voltages are capable of providing contact resistance measurements accurate to within +/- 110 nΩ. A THORLab PAZ005 piezo-actuator applies contact force during the measurements and to externally actuate the micro-contacts. A piezo-actuator is used to externally actuate the devices rather than using electrostatic actuation to apply a known contact force in addition to known current which provides a method to determine micro-contact resistance with great accuracy. The piezo-actuator is used in place of an atomic force microscope (AFM) because cycling rate of the piezo-actuator is much greater than an AFM [13]. The actuator has 20 µm of travel, 5 nm of resolution, and is capable of oscillating at up to 2 KHz. The force placed onto the contacts is measured by a FemtoTools model FT-5270 which is capable of measuring contact force to an accuracy of 50 nN. Three micromanipulators provide movement in three dimensions to align the force sensor and each micro-contact. The fixed-fixed beam that makes up the support structure for the contacts is created to utilize the Holm crossbar technique. This technique uses a known current flowing through the contact while measuring the voltage across the contact. This allows the contact resistance to be calculated. The micro-contact support structure is

shown in Figure 24. The micro-contacts are designed so that there are 16 devices on a single chip that is wire bonded to a carrier placed inside the test stand enclosure as seen in Figure 25. The carrier connects the devices on the chip to a breadboard on the outside of the enclosure so that the DUT can be wired to utilize the Holm crossbar technique. The Labview instruments are also connected to the DUT as shown in Figure 26 to take measurements and supply voltage to the beam.

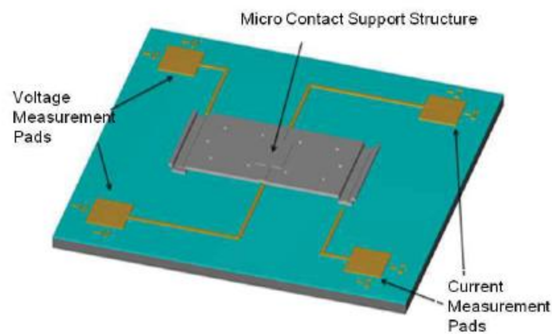

Figure 24. Micro-contact support structure that enables the Holm crossbar technique to be used to determine the contact resistance [8].

.

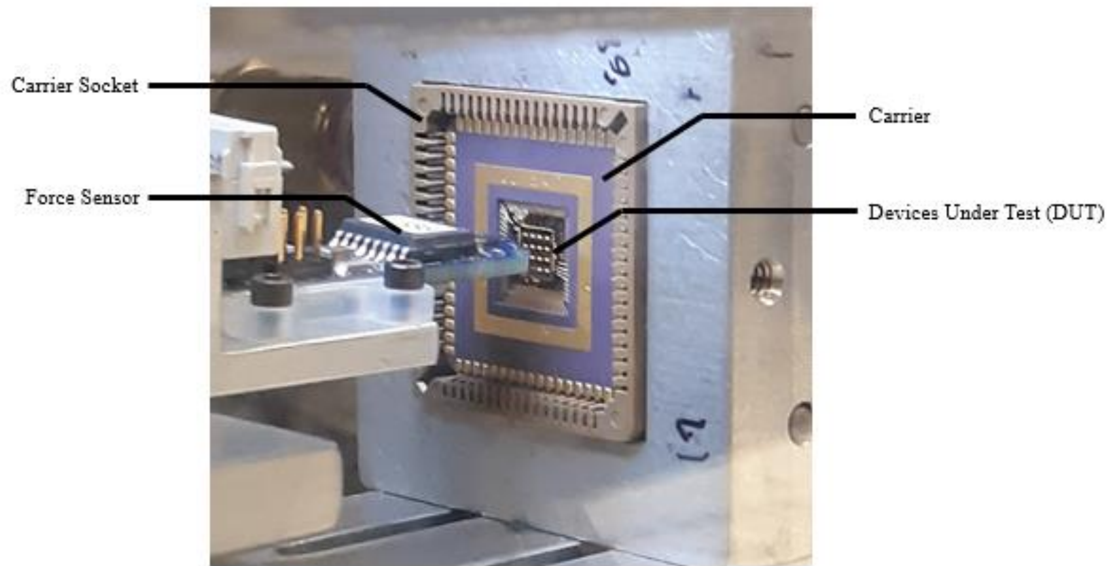

Figure 25. Image of the carrier with a chip having devices under test.

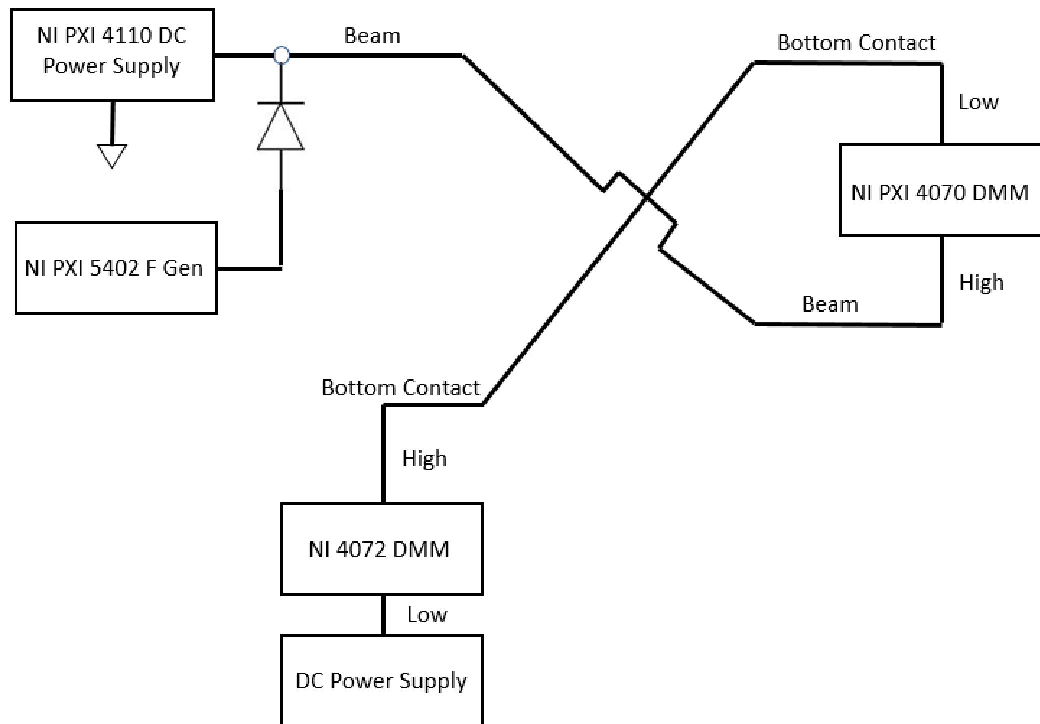

Figure 26. Schematic of a DUT connected to the test stand equipment.

3.6.1 Test Stand Modifications

At the beginning of this research, two new AmScope Microscope Digital Cameras utilized via a Universal Serial Bus (USB) connection to a laptop were acquired and installed to assist in visually aligning the force sensor to the center of a beam. The new cameras made the original camera setup and the wedge underneath the test stand obsolete so they were removed. The latest image of the test stand is shown in Figure 27.

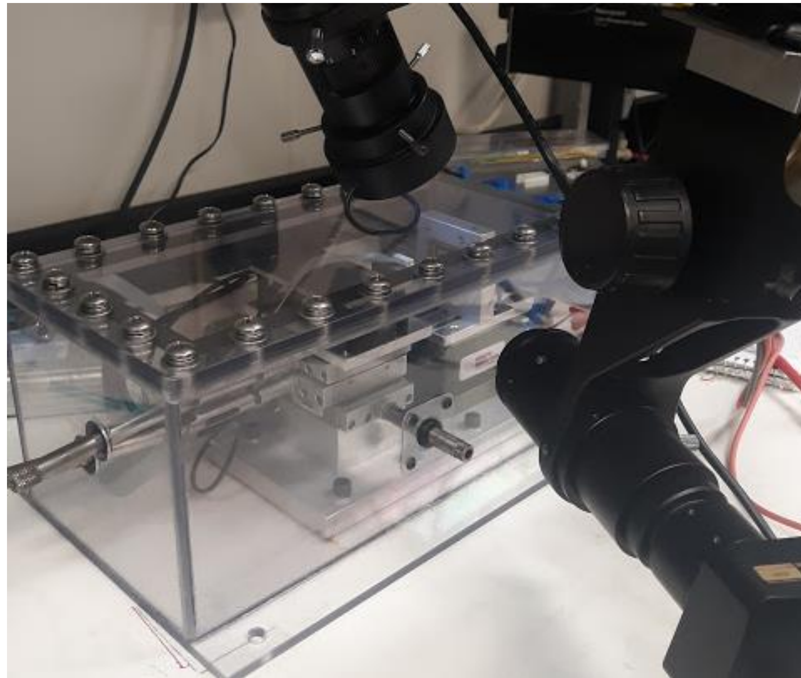

Figure 27. Current version of the test stand with new cameras mounted around it.

3.7 Types of Testing

3.7.1 Initial Contact Testing

Sixteen devices are contained on a carrier mounted in the carrier socket within the test stand. The first test a device undergoes is initial contact testing. A 1 V DC load is

applied to the beam while the force sensor moves the piezo-actuator in 20 nm increments until contact is made. The sensor continues to move until current is detected through the micro-contact and a voltage drop is observed. The force is then recorded as an offset and is effectively reset to zero. Once this occurs, the piezo-actuator advances until the desired contact force is achieved. At the same time, the current through the micro-contact, the voltage across it, and the applied force are recorded. The current and the voltage allow the contact resistance to be calculated using the Holm crossbar technique [35].

3.7.2 Cold Switch Testing

Cold switch testing for a specified number of cycles is done after the initial contact testing. The piezo-actuator is cycled at frequencies up to 2.5 kHz to induce wear on the contact. During a specific time during the cycle, a load is applied and removed to simulate the operation of a contact being switched open and closed. The load normally is 1 V except for one part of testing where it will be set to 0.5 V. Data collection for the contacts takes between 2 and 10 minutes. Testing contacts for millions of cycles or greater requires collecting data a set number of times per decade to balance the amount of time spent cycling and collecting data [35]. Testing to a billion cycles will be done to at least one micro-contact with a 3-D surface and will be compared to a micro-contact with a flat bottom also cycled a billion times as a control.

3.8 Examination of Contacts

The scanning electron microscope (SEM), the Leica DVM6 3-D microscope, the Zygo interference microscope, and the Tencor profilometer are available in the lab to use for examination of micro-contacts before and after reliability testing. The SEM is useful

to visually observe a micro-contact's cause of failing. It is capable of revealing switch failure due to an isolating layer developing in the form of a thin film or from the effects of electromigration. A switch that fails to open can be observed with the SEM to see whether the cause is from stiction or from plastic deformation. The profilometer and the Zygo interference microscope enable the height profiles of the grayscale micro-contacts to be measured. As mentioned earlier, the profilometer is used in determining the heights of the developed photoresist after direct writing with the Heidelberg Mask Writer as well as determining the heights of the grayscale micro-contacts after RIE. The Zygo interference microscope and the Leica 3-D microscope provide a three-dimensional view of the devices without damaging the surface of the micro-contacts.

3.9 Chapter Summary

This chapter discussed the methodology behind designing and fabricating micro-contacts made with grayscale lithography. First, the methods used to create the micro-contact and the fixed-fixed beam were discussed. The fabrication process uses both grayscale lithography and reactive ion etching which required characterization to be able to produce desired height profiles with a selectivity of 1 in the micro-contacts. The design of the experiments was discussed in depth to provide insight into the picking of factors and responses and how they can be used to determine statistical significance. The models for contact resistance are introduced in this section to be used again in the next section. The test stand was covered which will be used to perform the reliability testing as well as providing the contact resistance and the contact force. Finally, the testing and

examination procedures were covered to explain the data that would be measured and then analyzed later on.

IV. Analysis and Results

4.1 Chapter Overview

This chapter starts by discussing the results from the fabrication runs. Following fabrication, devices underwent testing to determine their contact resistance. Devices underwent initial contact testing to determine whether they matched the ballistic electron transport model. Devices then underwent cold switch testing for a set number of cycles to observe whether they had a stable contact resistance that fit one of the models or effects caused by a failure mechanism. Following the testing of all the designs, comparisons were done to see if any factors were significant. Some of the contacts were opened up using probe tips and observed with an SEM and 3-D microscope to determine whether a failure mechanism was occurring during testing.

4.2 Fabrication Analysis

The fabrication of the micro-contacts and the beam support structure underwent many iterations to produce working devices. The results from the fabrication runs are discussed in this section.

4.2.1 Grayscale Fabrication

A total of 9 wafers were created with grayscale 3-D surfaces using the Heidelberg mask writer. The last two wafers did not show any discernable height differences when using the Tencor profilometer in places where the laser hit the photoresist. Because of this, any future fabrication of wafers would require another characterization of the Heidelberg laser to create 3-D surfaces.

A new version of alignment marks was designed using L-Edit software to be used to align the micro-contacts to the first lithography mask used to pattern the lower metal. The numbers and shapes were reduced in size from the original alignment marks to be visible underneath the numbers and shapes of the first lithography mask. This version featured a long vertical bar and a long horizontal bar to make it easier to find the numbers and shapes on the EVG Mask Aligner since the wafer did not have any bright surfaces on it. The new alignment marks are shown in Figure 28.

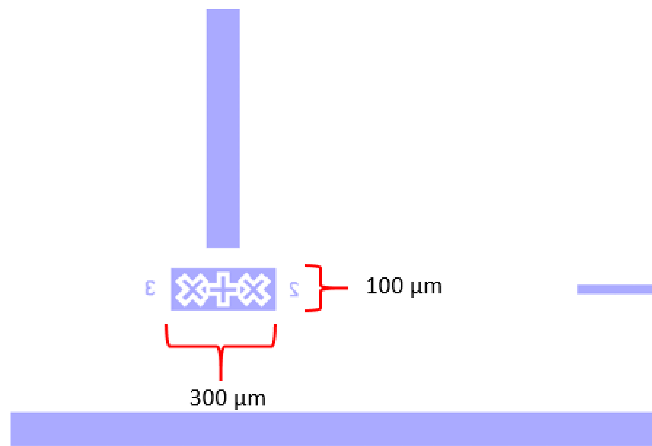

Figure 28. New Alignment marks designed using L-Edit software to align the wafer to the bottom metal patterns.

4.2.2 RIE

Repeated exposure with the RIE was necessary to transfer features etched into the photoresist into the nitride layer. A selectivity close to 1 was desired when doing this. Measurements of the two step heights of a three-step pyramid created with grayscale lithography were done using the Tencor Profilometer to determine the selectivity. The selectivity was calculated using Equation 44 and is shown in Table 2. The desired

selectivity close to 1 was achieved by running the RIE process three times for 90 seconds each with 26 sccm of O_2 and 45 sccm of CF_4. This produced micro-contacts with a maximum height of 1 µm.

Table 2. Measurements taken after grayscale lithography and after RIE exposure to calculate the selectivity.

	Measurement #1	Measurement #2
a	1.4	0.95
b	1.45	0.9
c	1	0.5
Selectivity	1.0526	0.9091

Following the RIE exposure to transfer the designs etched into the photoresist to the nitride layer, the photoresist was removed using acetone and the first deposition of gold was evaporated onto the wafer. Images were taken of the micro-contacts using the 3-D microscope to compare them to the designs created with L-Edit software. Two of the micro-contacts are compared to their designs in Figure 29 and Figure 30. The images of the actual micro-contact show that there are discrepancies between the designs and the fabricated micro-contact. The variability in the designs was observed previously in research by Coutu and Laurvick and is likely caused by the mask writing laser [23]. The complete comparison of all designs is found in Appendix C.

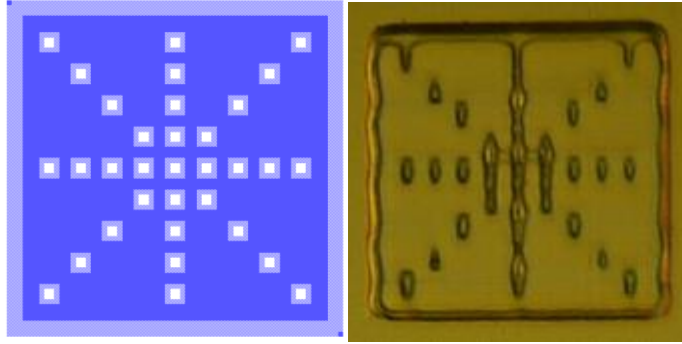

Figure 29. Comparison between the L-Edit design of the micro-contact and the actual micro-contact after fabrication.

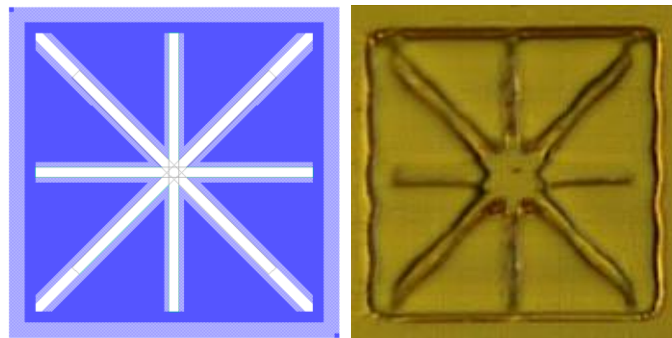

Figure 30. Comparison between the L-Edit design of the micro-contact and the actual micro-contact after fabrication.

4.2.3 Electroplating Beams

The maximum thickness of the beams created using electroplating required using Equation 38 and Equation 39. The maximum thickness was based on the dimensions of the beam and the maximum force that the force sensor can apply to the beam. The length of the beams are 400 µm, the width of the beams are 250 µm, and the maximum deflection of the beams is 3 µm. The maximum force that the force sensor can apply is 2500 µN and the Young's modulus for electroplated gold is 79.42 GPa [8]. The

maximum thickness of the electroplated beams, given these constants, was determined to be 5.519 μm. Exceeding this thickness meant that the beams would be unusable with the force sensor and would require gold etching before the sacrificial layer is released to reduce the thickness. The first wafer that was electroplated resulted in having thin beams that were still usable but not ideal. The second wafer used the same settings but failed to electroplate evenly, making the beams and devices unusable. This issue was resolved by developing the exposed AZ 5214 photoresist for an extra 10 seconds, from 60 seconds to 70 seconds to ensure that it would be developed away to the surface of the wafer to provide the places for the electroplated gold to attach itself to the wafer. The third and fourth wafer electroplated used too high of a setting to try and correct for the thin beam issue of the first wafer. This resulted in beams that were too thick for the force sensor. It was determined that the beams were about 2 μm too thick and needed a gold etch before the chips were released. The gold etchant, potassium iodide, etched at a rate of 28 angstroms/second which required an etch time of about 12 minutes to achieve the 2 μm reduction. Following the gold etch, the beams worked as expected with the force sensor during testing. The difference between a beam that did not need etching and a beam that underwent the 12 minutes of etching is shown in Figure 31 and Figure 32.

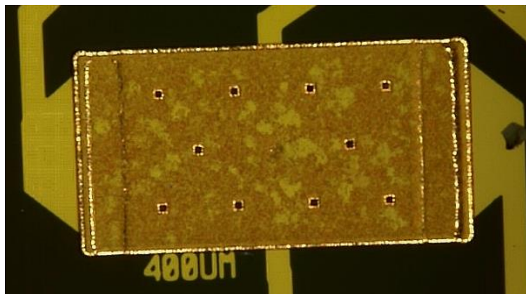

Figure 31. Electroplated beam that did not need gold etching.

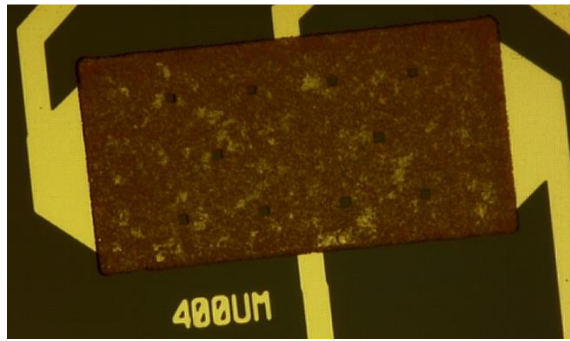

Figure 32. Electroplated beam after 12 minutes of gold etching to make it thinner.

4.3 Micro-contact Design #1 with 6 µm Bump

The micro-contact design shown in Figure 33 was cycled 200 million times before testing was ended. The design consisted of small circles spaced 4 µm apart with a 6 µm radius upper hemispherical bump as specified by the first DOE run shown in Figure 19.

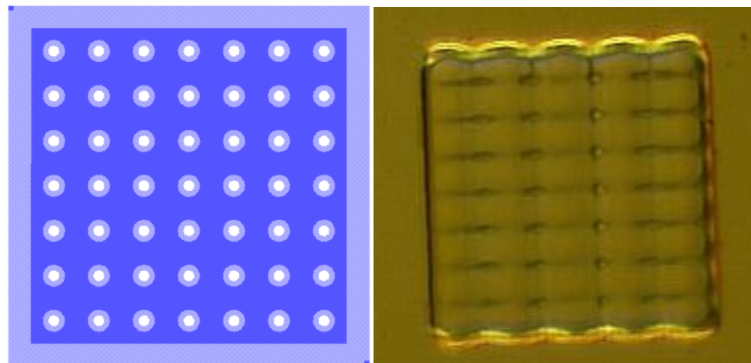

Figure 33. Micro-contact design in L-Edit specified by DOE run #1 and the resulting design after fabrication.

4.3.1 Initial Contact Testing

Figure 34 shows the measured micro-contact resistance for forces up to 200 µN after only 10 cycles. The graph shows that the resistance of the micro-contact is

comparable to the modeled resistance for ballistic electron transport with the Knudsen number equal to 10.

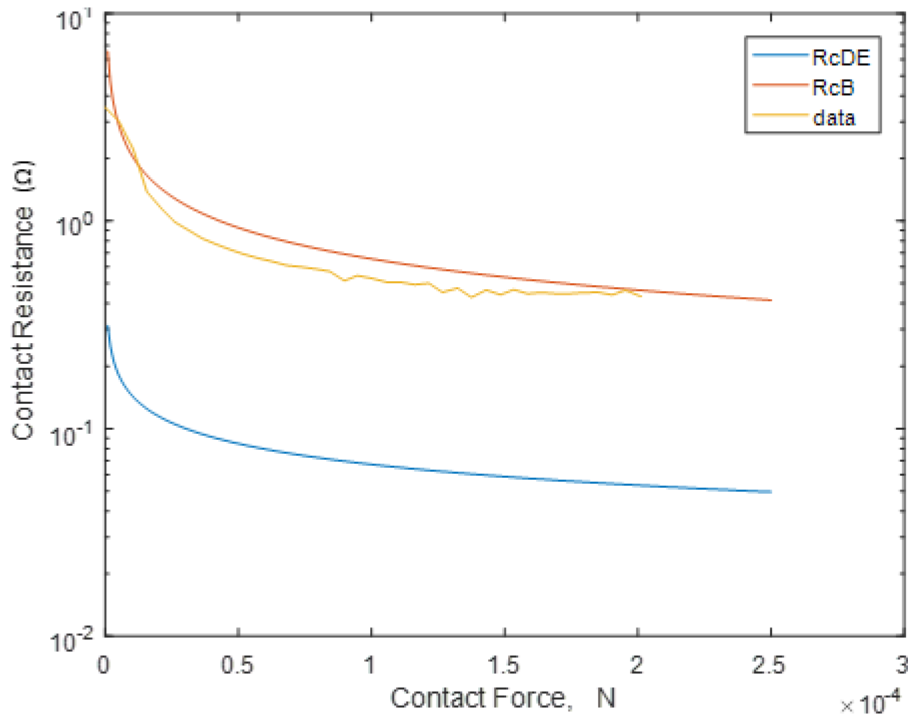

Figure 34. Contact resistance of DOE design #1 after 10 cycles compared to models for ballistic electron transport with a Knudsen number of 10, labeled as RcB and diffuse electron transport, labeled as RcDE.

4.3.2 Cold Switch Testing for 10^8 cycles

The micro-contact was cycled for 10^8 cycles and the resistance for forces up to 200 μN was recorded three times per decade. Figure 35 shows the resistance of the micro-contact when approximately 100 μN was applied over the 10^8 cycles. The figure compares the measured resistance to the resistance given by the ballistic electron transport model for Knudsen numbers of 10 and 100. Figure 36 shows the lowest

resistance measured during each recording, which was approximately 200 μN and compares it to the resistance given by the ballistic electron transport model. Both Figure 35 and 36 show that the micro-contact followed the model for ballistic electron transport until around 10^5 cycles where the resistance spikes and then continues to increase. This increase in the resistance is likely due to the effects of electromigration that were observed after testing.

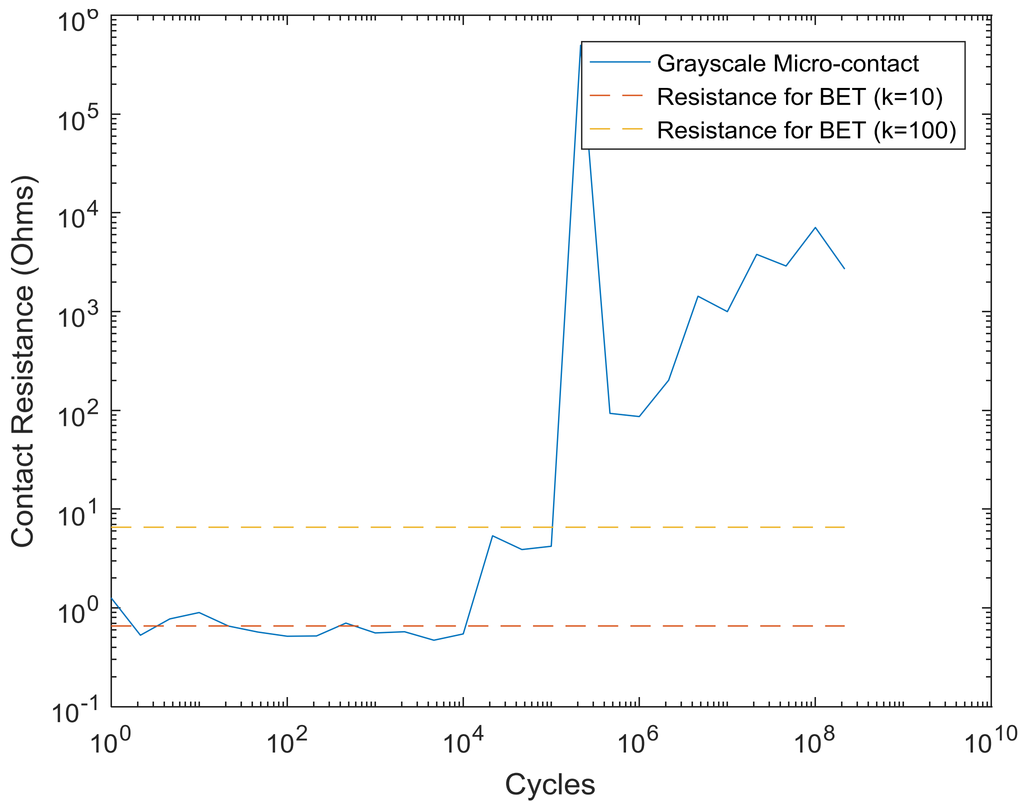

Figure 35. Resistance of the micro-contact while 100 μN were applied for the duration of testing, where BET stands for ballistic electron transport. An increase in resistance is thought to be because of electromigration.

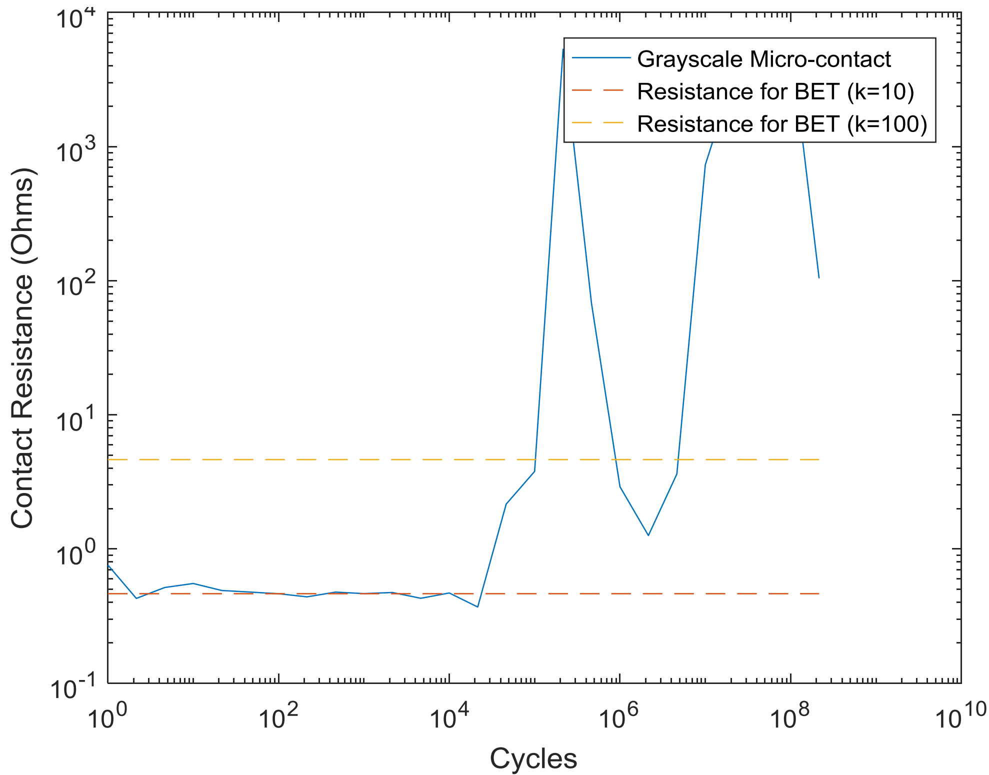

Figure 36. Lowest resistances recorded of the micro-contact for the duration of testing.

4.3.3 Post-test Imaging

Following the testing of the micro-contact in the test stand, the chip was removed from the carrier and placed onto a glass slide. A probe tip was used to flip open the beam covering the micro-contact and made it possible to see the micro-contact with a microscope. Figure 37 shows the micro-contact after testing that was photographed using the 3-D microscope. Figure 37 shows a small dark area near the center of the micro-contact where it appears that the upper hemispherical bump made contact and began to electromigrate material. Figure 38 show the same micro-contact as seen with an SEM to

focus on the dark spot. The electromigration of material seen with the microscopes is likely to be the reason the resistance started to increase after 10^5 cycles.

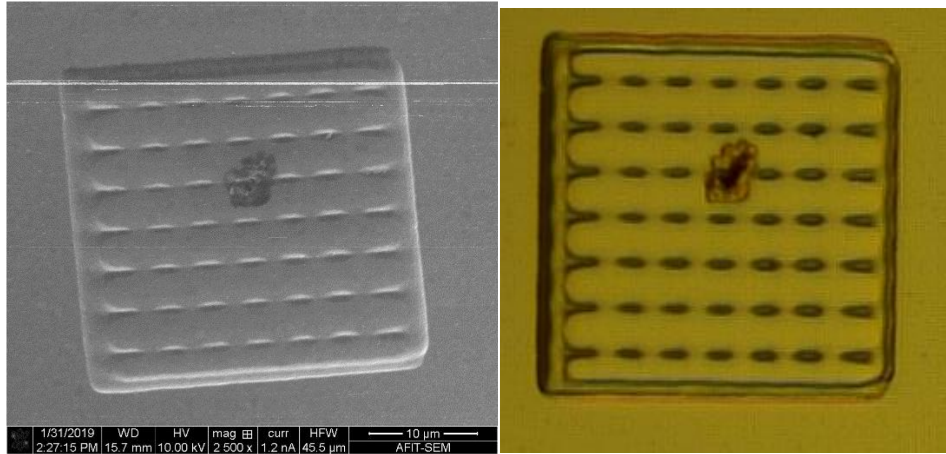

Figure 37. SEM image of the micro-contact after testing on the left, and image taken with a 3-D microscope on the right.

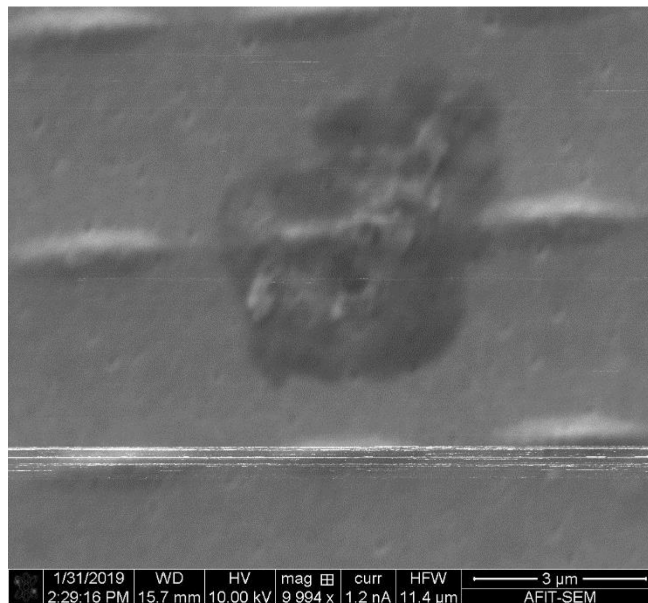

Figure 38. SEM image of the damage caused by electromigration on the micro-contact.

4.4 Micro-contact Design #4 with 6 µm Bump

The micro-contact design shown in Figure 39 was tested for 1 million cycles. The design featured large squares spaced out by 4 µm and an upper bump with a 6 µm radius. The testing showed strong evidence that the micro-contact underwent ballistic electron transport.

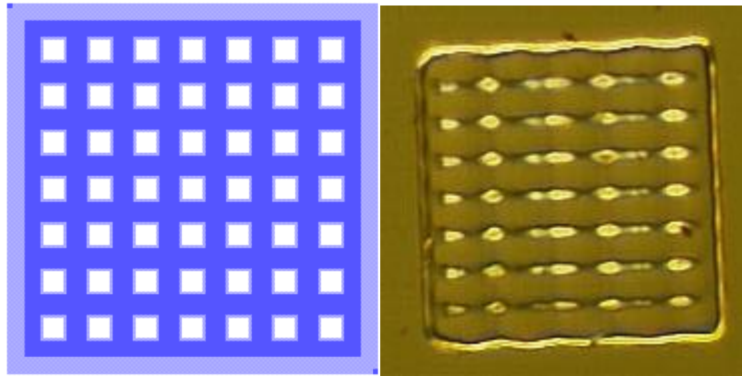

Figure 39. Micro-contact design in L-Edit specified by DOE run #4 and the resulting design after fabrication.

4.4.1. Initial Contact Testing

Figure 40 shows the measured micro-contact resistance for forces up to 200 µN after only 10 cycles. The graph shows that the resistance of the micro-contact is comparable to the modeled resistance for ballistic electron transport with the Knudsen number equal to 10.

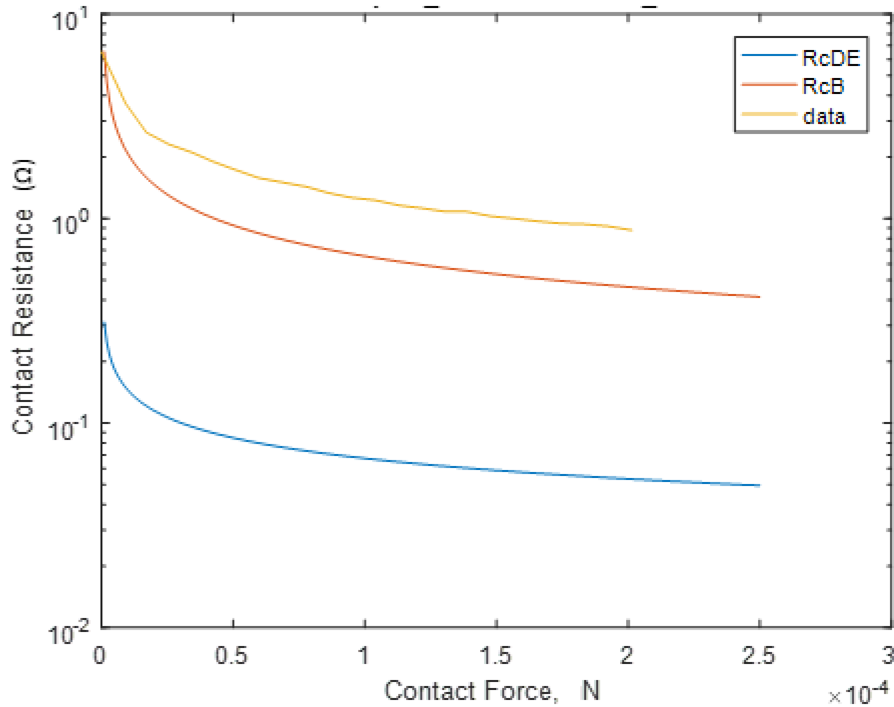

Figure 40. Resistance of the micro-contact for forces up to 200 µN after 10 cycles compared to models for ballistic electron transport with a Knudsen of 10, labeled as RcB and for diffusive electron transport labeled as RcDE.

4.4.2 Cold Switch Testing for 10^6 cycles

The micro-contact was tested for 10^6 cycles with three test points recorded per decade. Figure 41 shows the resistance of the contact with 100 µN applied for all the test points. Figure 42 shows the lowest resistance recorded of the contact while a force was applied for all test points. Both figures show that the micro-contact had a fairly stable resistance and remained within the model for ballistic electron transport after the initial wear-in period.

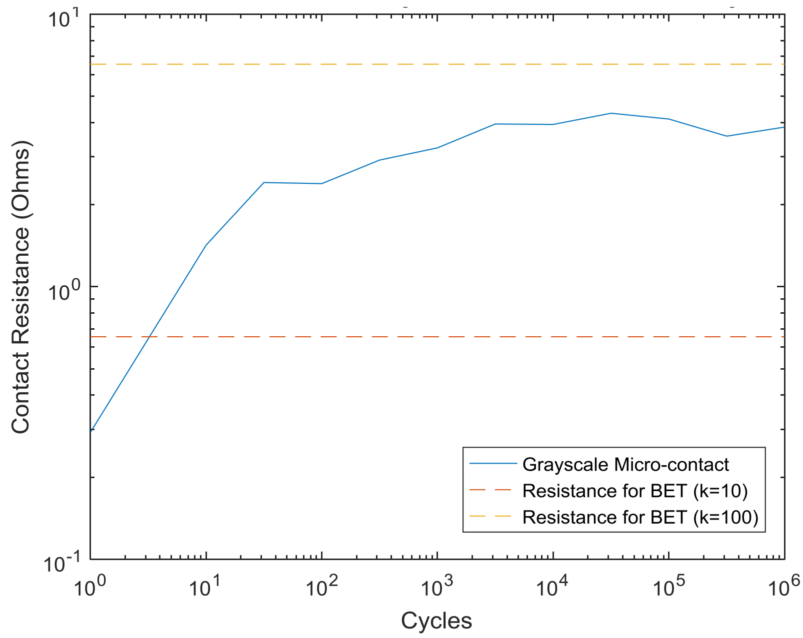

Figure 41. Resistance of the micro-contact while 100 µN was applied at each test point. The micro-contact underwent 10^6 cycles.

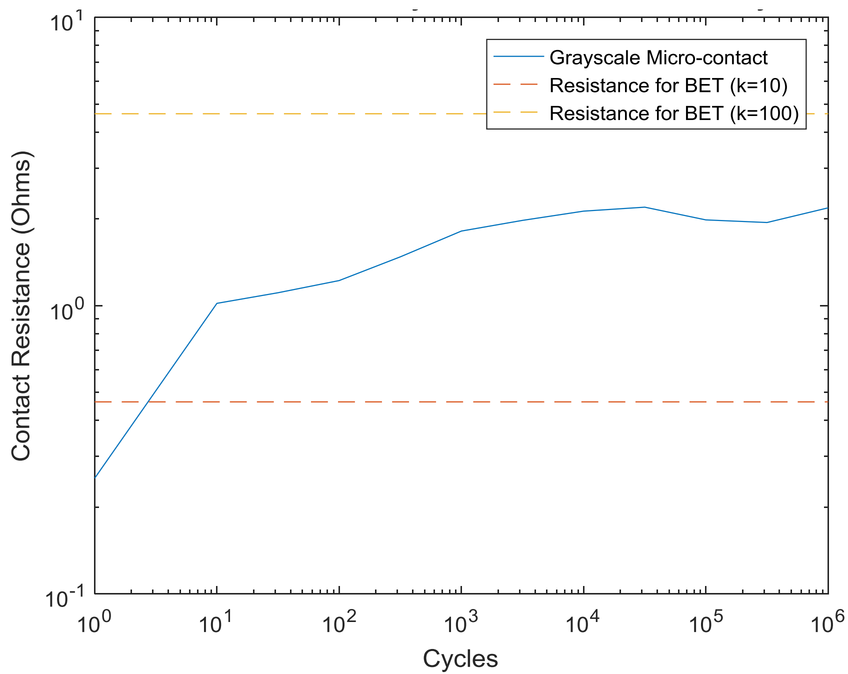

Figure 42. Lowest resistance recorded while a force was applied for each test point. The micro-contact underwent 10^6 cycles.

4.5 Micro-contact Design #1 with 8 μm Bump

The micro-contact design shown in Figure 43 was cycled 10^6 times. The design consisted of small circles spaced 4 μm apart and an upper bump with an 8 μm radius. The results of this testing showed evidence of a contact beginning to have effects from a failure mechanism.

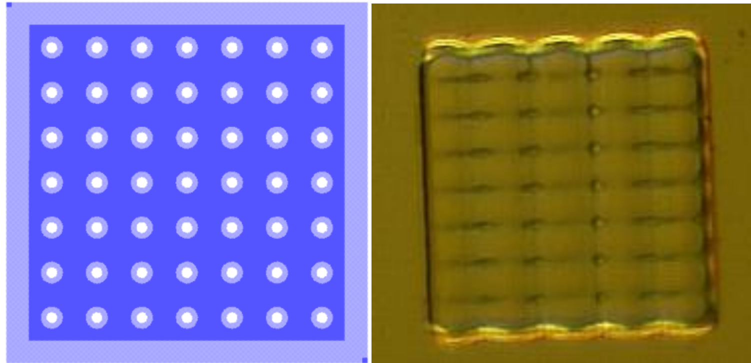

Figure 43. Design of the micro-contact as well as an image of the actual contact.

4.5.1 Cold Switch Testing for 10^6 cycles

Figure 44 and Figure 45 show the resistance of the micro-contact for forces up to 200 μN for the 39,810th cycle and the millionth cycle, respectively. Figure 44 shows the beginning of irregular resistance curves which is a sign that a failure mechanism is beginning to occur. Once the contact reached 10^5 cycles, it began to have a high resistance for the remainder of testing which is shown in Figure 46 and Figure 47.

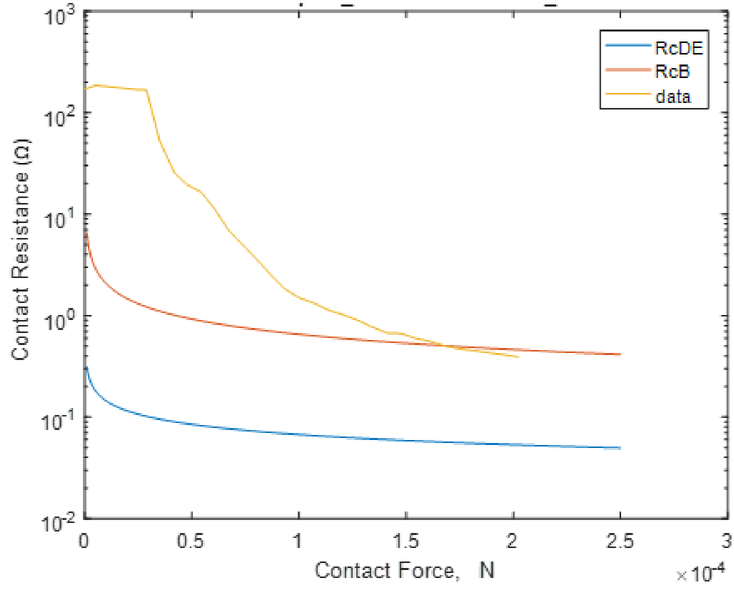

Figure 44. Resistance of the micro-contact for forces up to 200 µN after 39,810 cycles. The irregular shape of the curve does not match either model and is an indication that a failure mechanism is occurring.

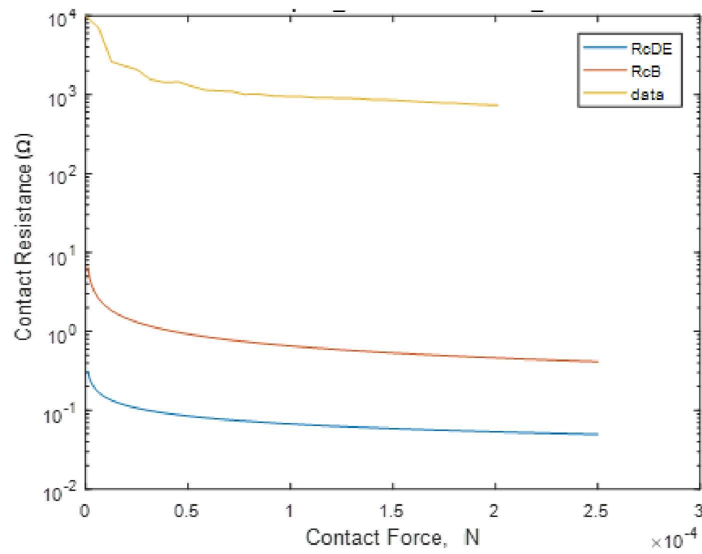

Figure 45. Resistance of the micro-contact after a million cycles for forces up to 200 µN.

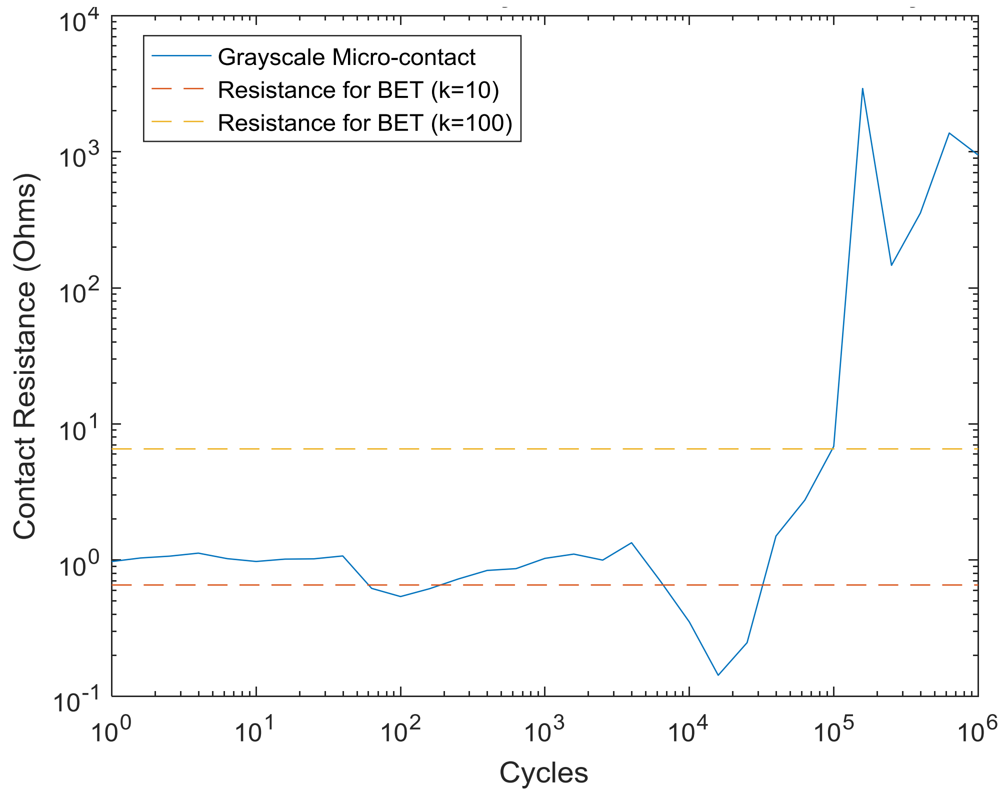

Figure 46. Resistance of the micro-contact while 100 µN is applied taken at test points spread out over the duration of testing. The sharp increase in resistance near the end of testing is an indicator of a failure mechanism.

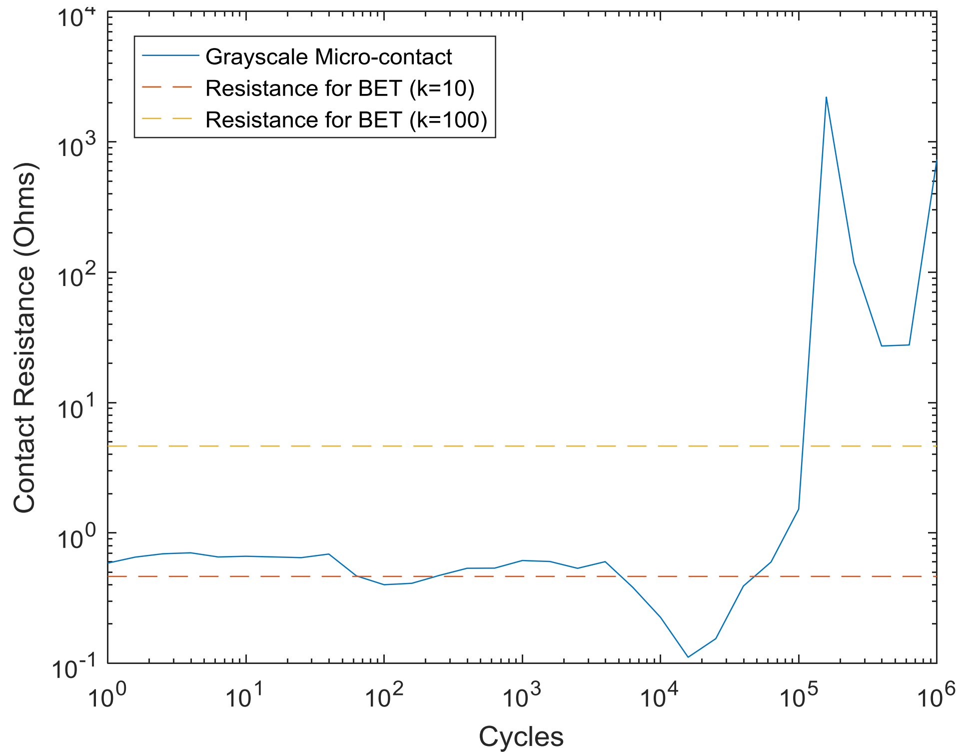

Figure 47. Lowest resistance recorded of the micro-contact measured at test points for the duration of testing.

4.6 Micro-contact Design #5 with 8 µm Bump

Figure 48 shows the design of the micro-contact that was tested for 10^6 cycles. The design consisted of small circles spaced out by 6 µm along with an upper bump with an 8 µm radius. This contact demonstrated the most stable contact resistance throughout the duration of testing. Additionally, it remained in the ballistic electron transport region for the entirety of testing.

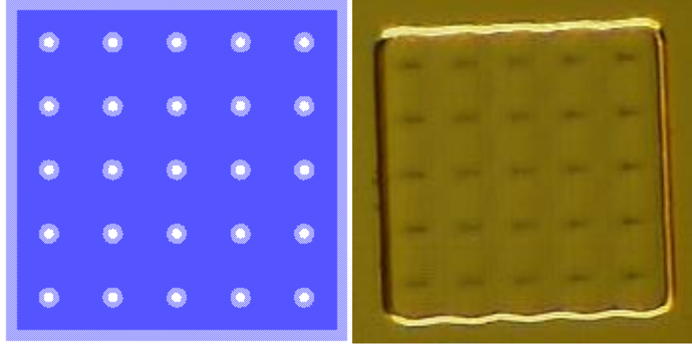

Figure 48. Design of the micro-contact and an image of the actual micro-contact.

4.6.1. Contact Switch Testing for 10^6 cycles

Figure 49 shows the resistance of the micro-contact for forces up to 200 µN after the millionth cycle. Throughout testing, the shape of the curve shown in Figure 49 was present in all other test points. Figure 50 and Figure 51 show the resistance of the contact over the duration of testing and reveal that the contact underwent ballistic electron transport for the entirety of testing. It also revealed that the micro-contact had an extremely stable contact resistance.

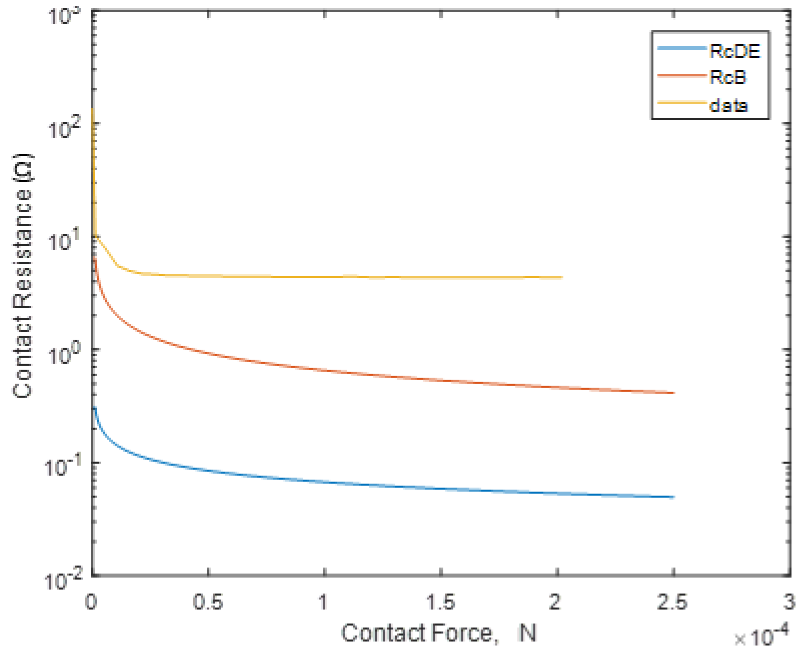

Figure 49. Contact resistance for forces up to 200 µN after the millionth cycle.

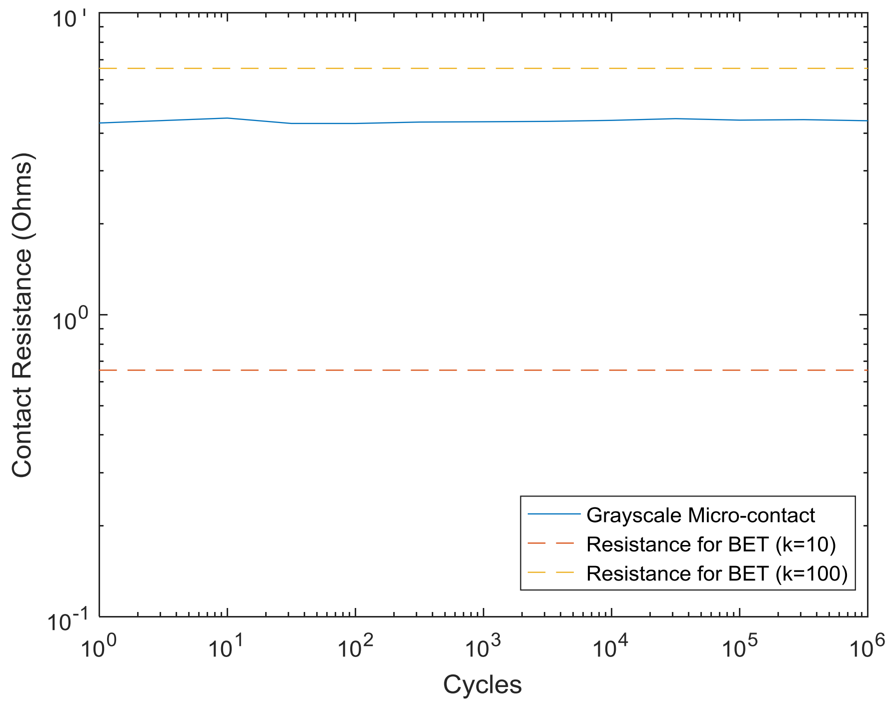

Figure 50. Contact resistance measured while 100 µN was applied to the beam taken at test points throughout testing.

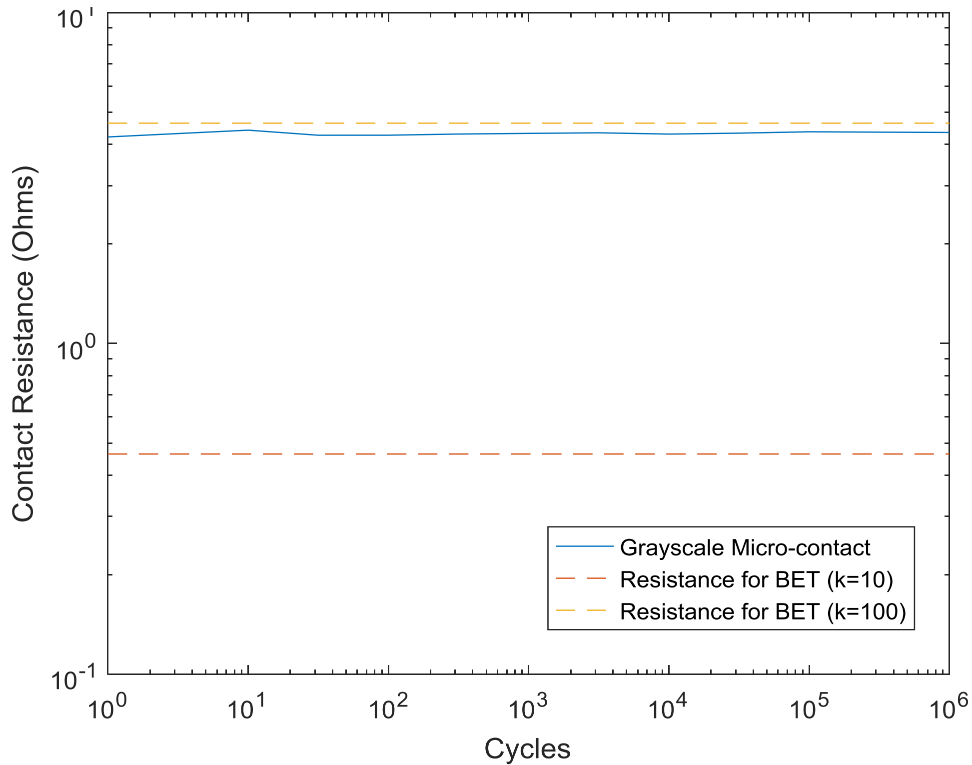

Figure 51. Lowest contact resistance measured while a force was applied taken at test points during testing. The resistance shows that the micro-contact underwent ballistic electron transport for the duration of testing.

4.7 Micro-contact Failure Prediction: Design #8 with 6 μm Bump

Figure 52 shows the design of a micro-contact tested for a million cycles. This design consisted of large squares spaced apart by 6 μm and an upper bump with a radius of 6 μm. This micro-contact began to have a large resistance after 100 cycles and began to have irregular resistance curves as seen in Figure 53. This micro-contact was likely affected by a failure mechanism that started in the beginning of testing.

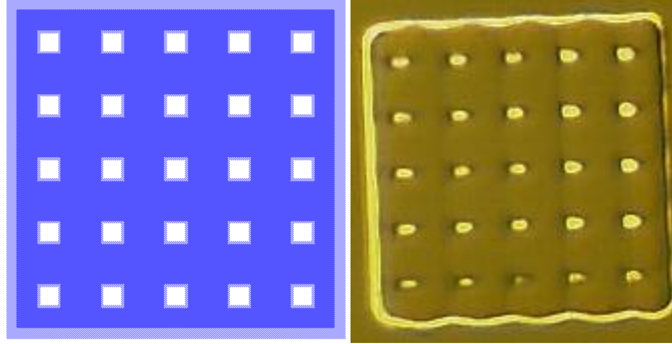

Figure 52. Design and image of the micro-contact that was tested for a million cycles.

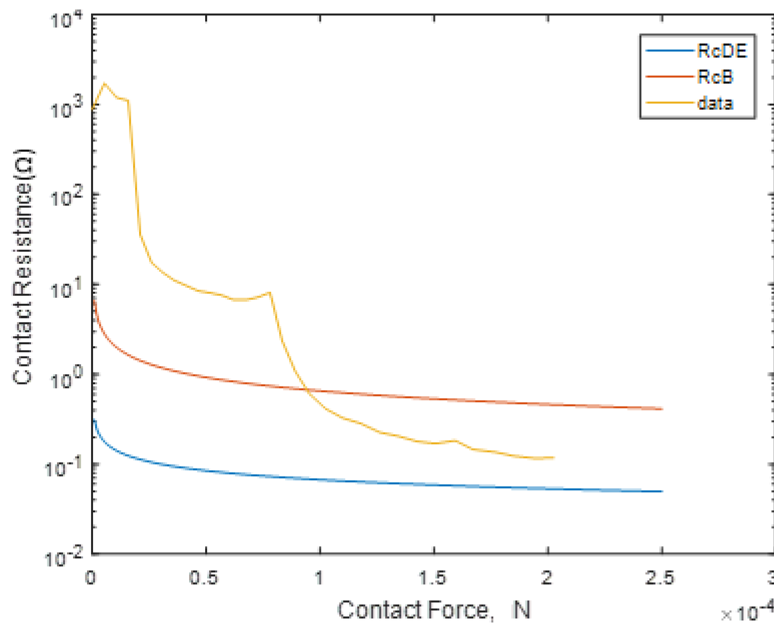

Figure 53. Resistance of the micro-contact for forces up to 200 µN after 10 cycles. The irregular shaped curve is an indicator that the contact is being affected by a failure mechanism.

4.7.1 Contact Switch Testing for 10^6 cycles

Figure 54 and Figure 55 show how the resistance of the micro-contact began to increase early on in the testing. The sudden increase is likely due to a failure mechanism taking effect.

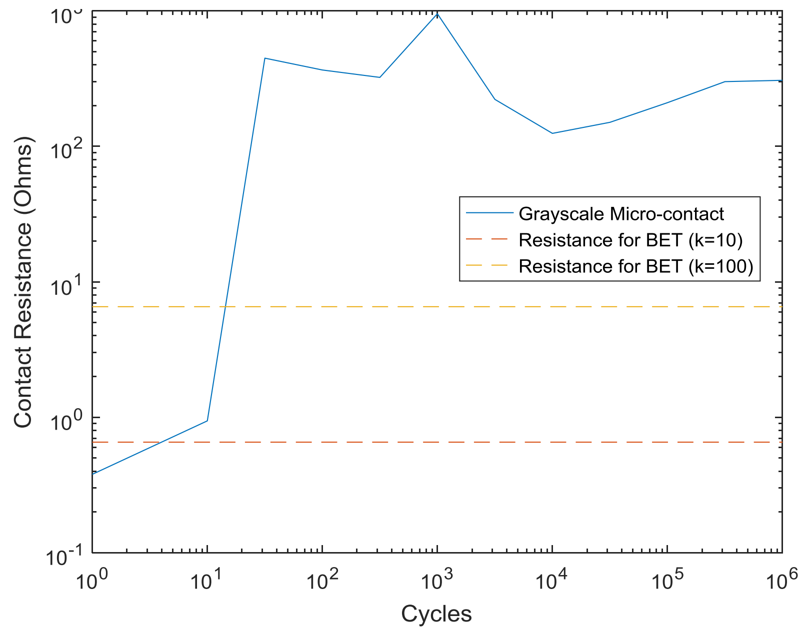

Figure 54. Resistance of the micro-contact with 100 µN applied to the beam taken at test points throughout testing.

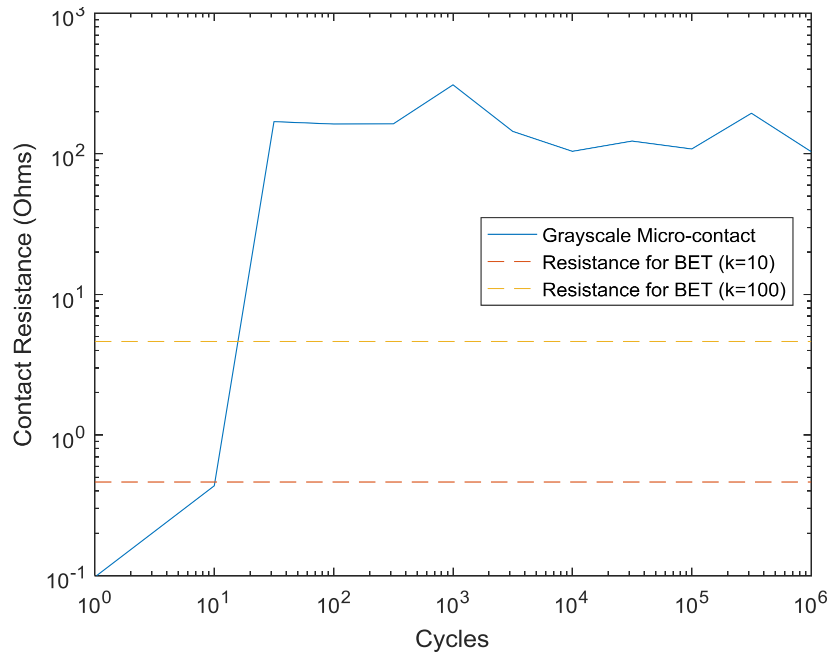

Figure 55. The lowest resistances measured while a force was applied to the beam for the micro-contact taken at test points throughout testing.

4.8 Micro-contacts used as Controls

Two micro-contacts were tested and used as controls. These micro-contacts had flat bottoms and an upper bump with a 6 μm radius. The first contact was cycled a million times and the second contact underwent testing for 10^8 cycles.

4.8.1. Results from control micro-contact after 1 million cycles

The resistance over the duration of the million cycles is shown in Figure 56 and Figure 57. Both figures show that after the wear-in period, the micro-contact remains near the model for diffuse electron transport.

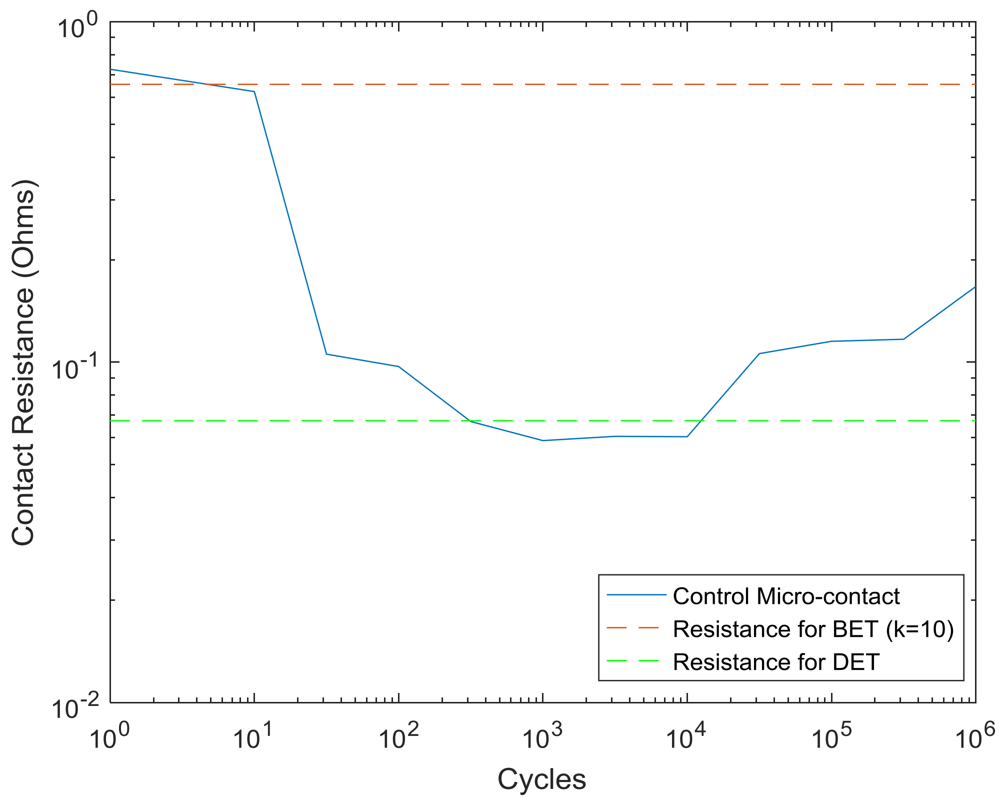

Figure 56. Resistance of the micro-contact with 100 µN applied to the beam taken at test points throughout testing. BET stands for ballistic electron transport and DET stands for diffusive electron transport.

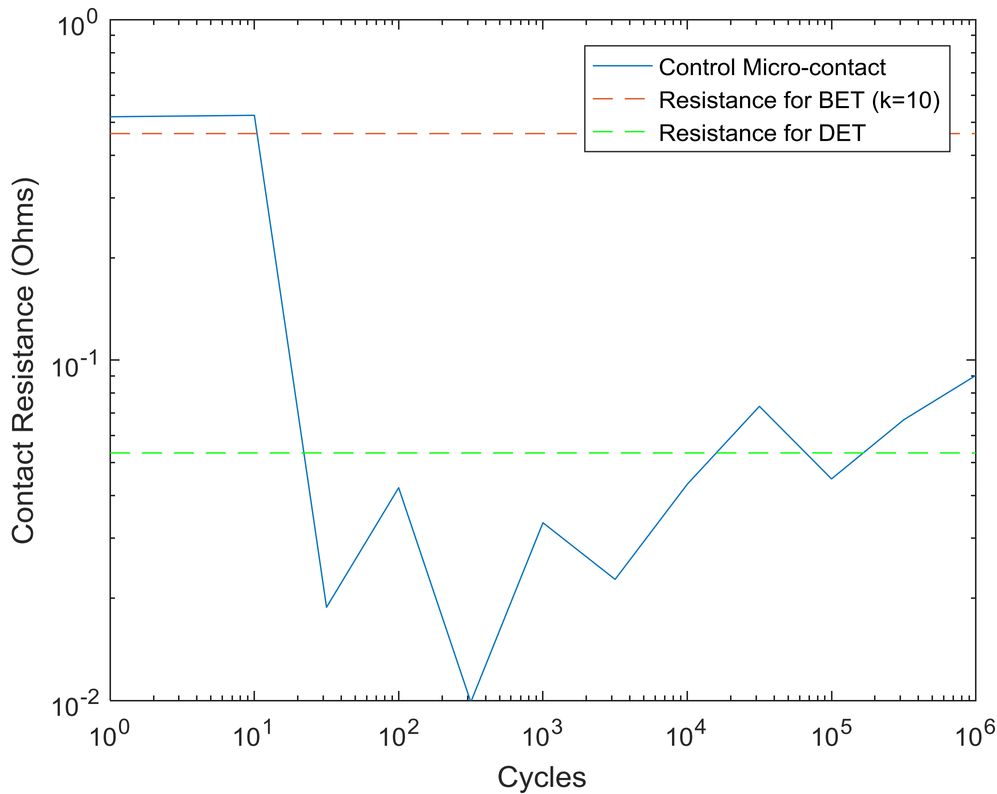

Figure 57. The lowest resistances measured while a force was applied to the beam for the micro-contact taken at test points throughout testing. The control micro-contact remained diffuse after the initial wear-in period.

4.8.2. Results from control micro-contact after 100 million cycles

A separate micro-contact with a flat bottom was used as a control to investigate the reliability after 100 million cycles. Figure 58 and Figure 59 show that the micro-contact had resistances in the ballistic electron transport region for the first hundred cycles and then had resistances indicative of diffuse electron transport until a million cycles. After a million cycles, the contact had large increases in resistance which was an indicator that a failure mechanism was occurring. After testing, a probe tip was used to

open up the beam and expose the micro-contact. Figure 60 and Figure 61 show the images of the micro-contact after testing and indicate that there was some electromigration happening where the upper bump met the contact.

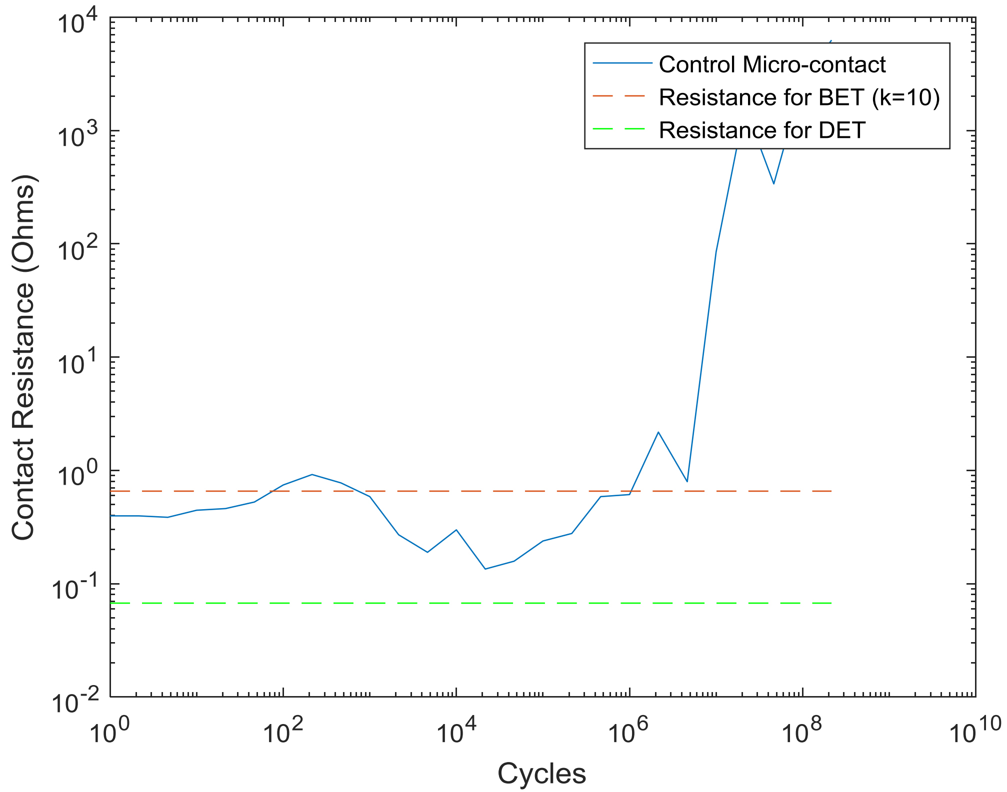

Figure 58. Resistance of the micro-contact with 100 µN applied to the beam taken at test points throughout testing.

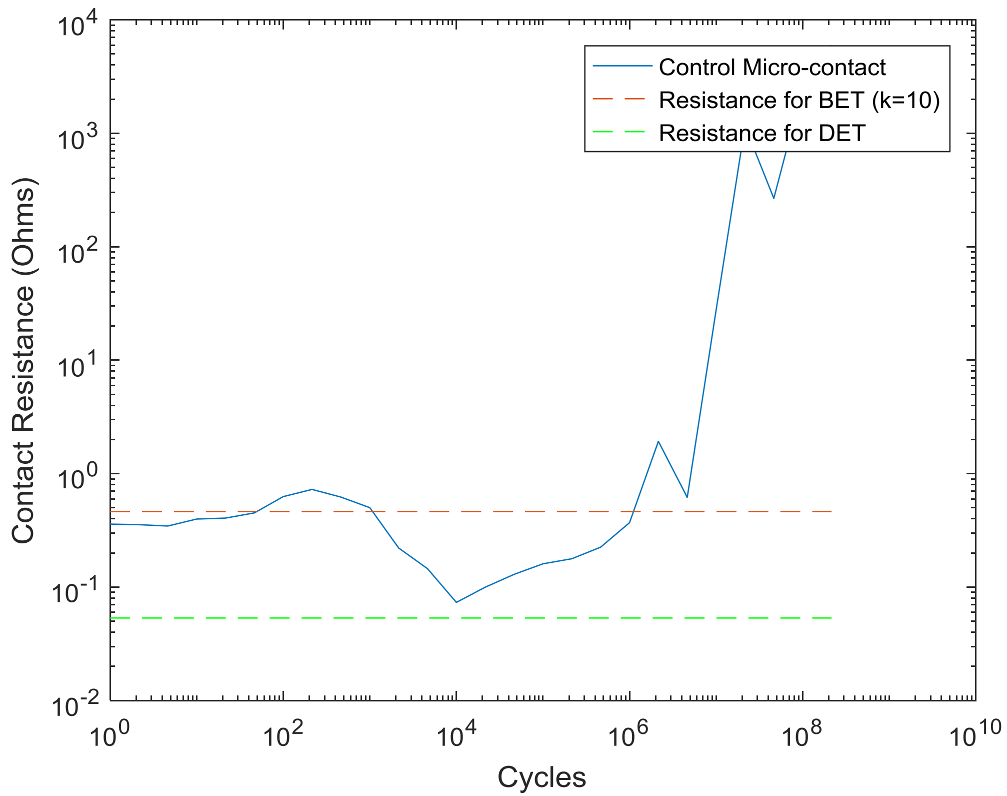

Figure 59. The lowest resistances measured while a force was applied to the beam for the micro-contact taken at test points throughout testing.

Figure 60. Image taken with the 3-D microscope showing that electromigration started to occur on the bottom contact.

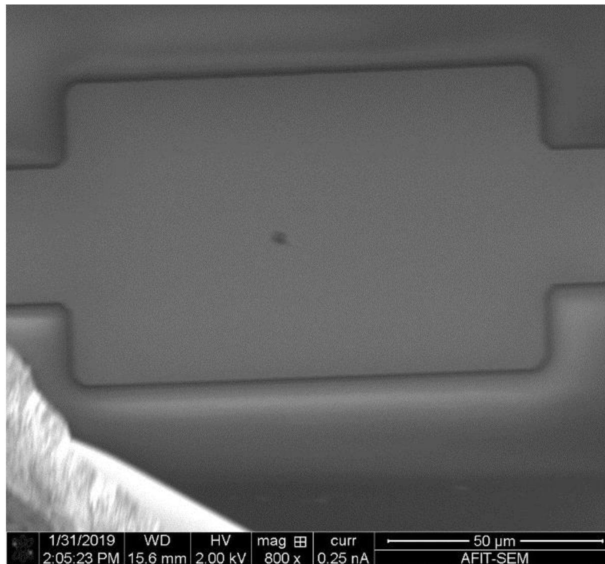

Figure 61. SEM image showing the damage caused by electromigration to the bottom contact.

4.9 Comparison Testing

Although there were duplicates on each chip, there was a lower yield of working devices than expected due to issues with fabrication, the release process, and wires adhering to the surface of the chips during wire bonding. As a result of the low yield, the original planning to use DOE techniques to determine significant factors fell out of favor for more basic comparisons. Using DOE as a method to design micro-contacts streamlined the process to analyze differences in specific factors while holding the other factors constant. The comparisons looked at differences in resistance between a bottom contact with a 3-D surface and one with a flat bottom, differences in the voltage load, and differences in the size of the upper bump.

4.9.1 Longevity of Grayscale 3-D Surface Compared to Control

The comparison of the resistance between a micro-contact with a 3-D surface created with grayscale lithography and one with a flat bottom was done using the data from section 4.3.2 and 4.8.2. For both micro-contacts, there were large increases in the resistance indicating a failure mechanism that were confirmed after testing with the use of a microscope although neither contact failed to open or close during testing. The large increase occurred in the grayscale micro-contact a decade earlier than in the control micro-contact. It is unclear if this is a trend without more replications of the testing being done.

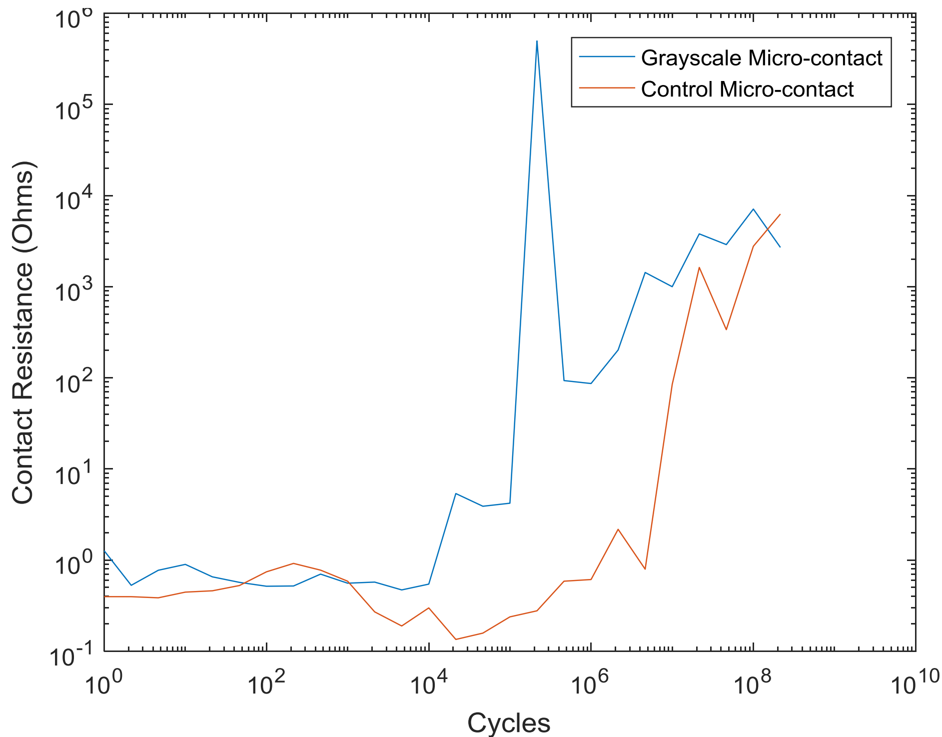

Figure 62. Comparison of the resistance measured when 100 μN is applied between a contact with a 3-D surface and one without.

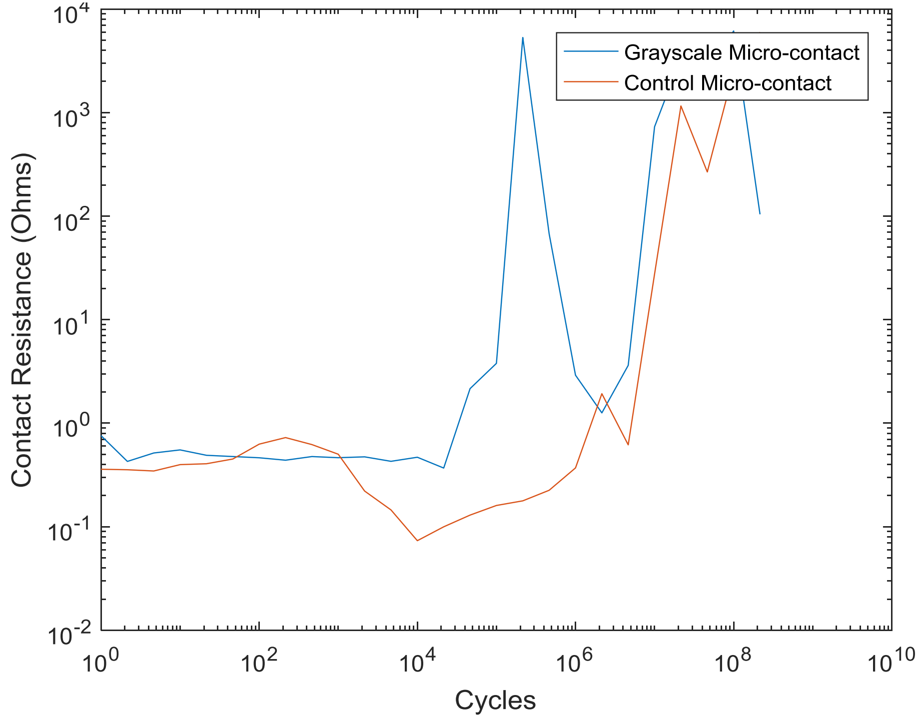

Figure 63. Comparison of the lowest resistances recorded while a force was applied between a contact with a 3-D surface and one without.

4.9.2 Voltage Comparison

A comparison between using 1 V and 0.5 V was done to see if the load applied would affect whether a micro-contact would be in the ballistic electron transport region and the longevity of the micro-contact. The design of the micro-contacts used for this comparison was described in the first DOE run with small circles spaced out by 4 µm and an upper bump with a radius of 6 µm. Figure 64 and Figure 65 show the resistance of the two micro-contacts over the course of testing. Both figures show that the resistance of the contact applied with 1 V was closer to the ballistic electron transport region after 100

cycles. Due to neither micro-contact failing over the course of 1 million cycles, more testing is needed to be done for more cycles to determine if a specific load is better for the longevity of micro-contacts.

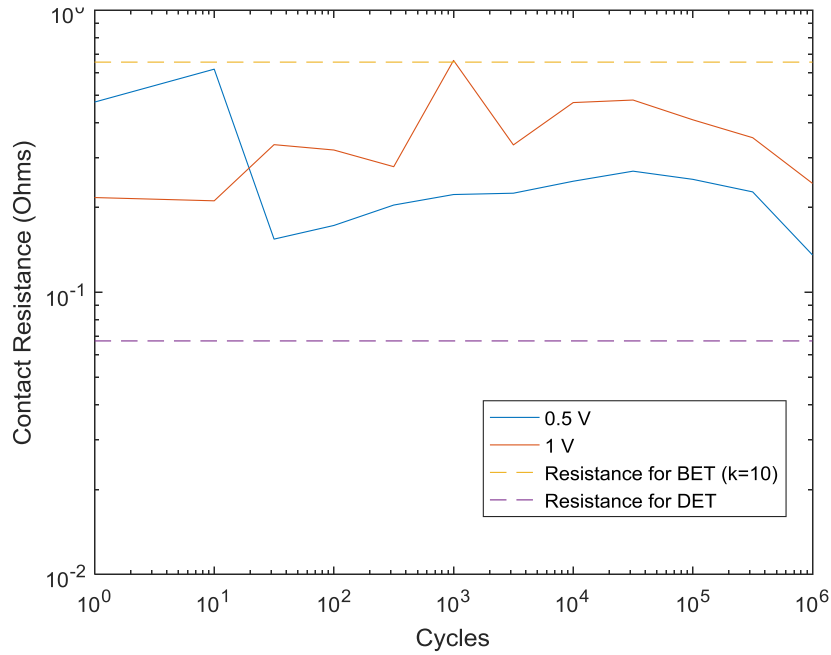

Figure 64. Comparison of the resistance measured when 100 μN is applied between a contact with a 0.5 V load and one with a 1 V load.

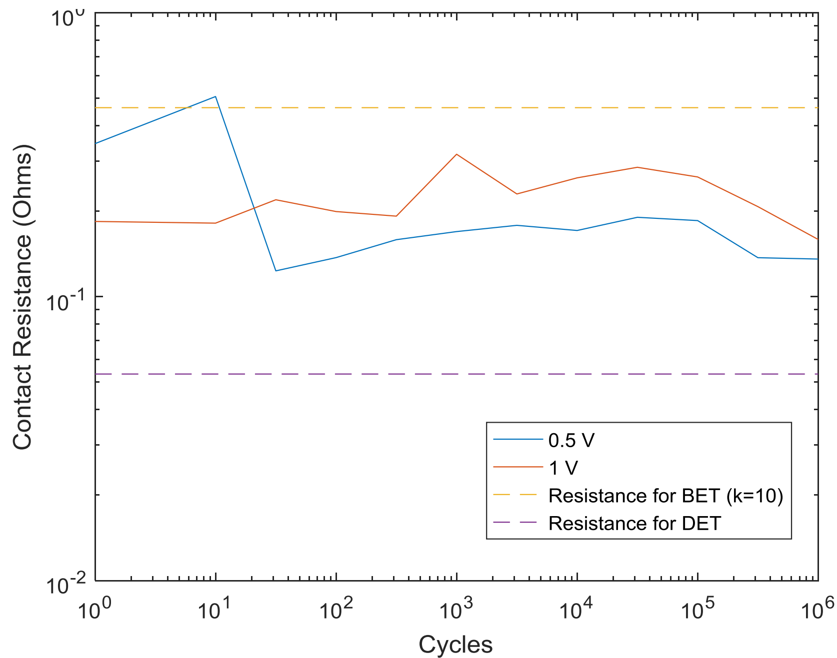

Figure 65. Comparison of the lowest resistances recorded while a force was applied between a contact with a 0.5 V load and one with a 1 V load.

4.9.3 Upper Bump Radius Comparison

A comparison between micro-contacts with an upper bump radius of 6 μm and 8 μm was done to see if the size of the upper bump would affect whether a micro-contact was in the ballistic electron transport region. The design used for this micro-contact was described in the first and ninth DOE run with small circles spaced out by 4 μm. The only difference between the two micro-contacts was the radius of the upper bump. Figure 66 and Figure 67 show the resistance of the contacts while they experienced forces up to 200 μN after 100,000 cycles and a million cycles, respectively. These figures show that the curves for the contact with a 6 μm radius bump appear to remain closer and more similar in shape to the ballistic electron transport region than the contact with the 8 μm radius

bump. Figure 68 and Figure 69 show that the 6 µm radius bump micro-contact had the highest resistances after a thousand cycles.

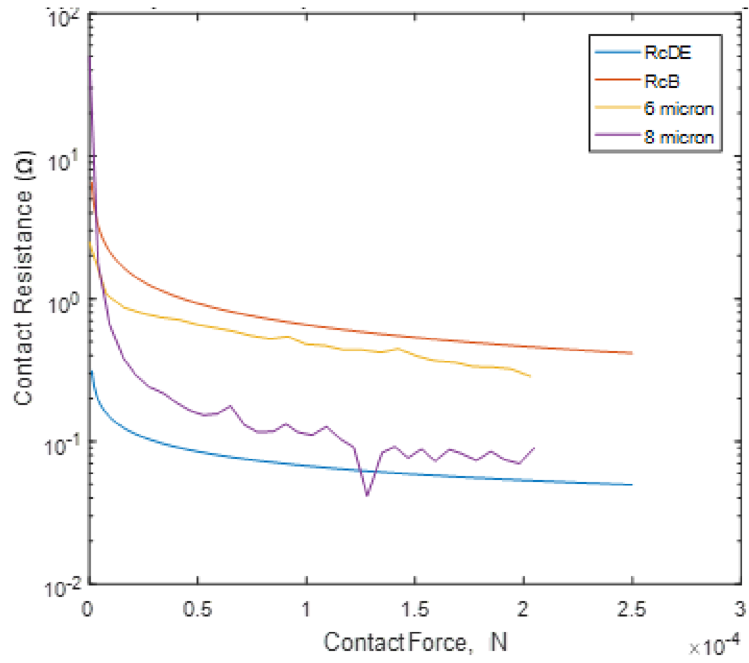

Figure 66. Resistance of the micro-contacts for forces up to 200 µN after 100,000 cycles.

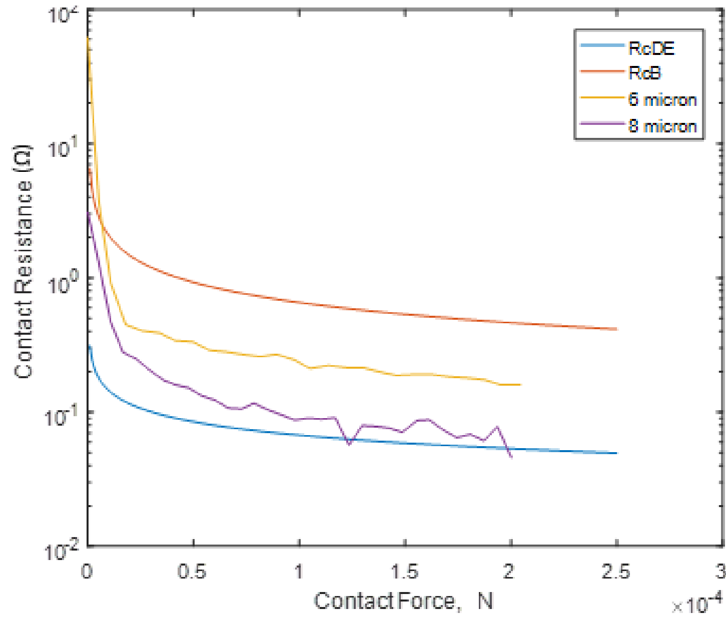

Figure 67. Resistance of the micro-contacts for forces up to 200 μN after a million cycles.

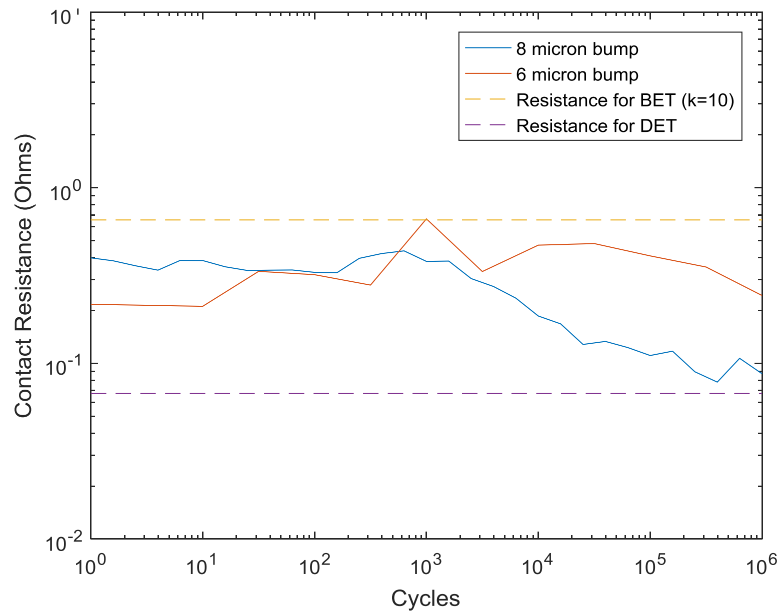

Figure 68. Comparison of the resistance measured when 100 μN is applied between a contact with a 6 μm upper bump radius and an 8 μm upper bump radius.

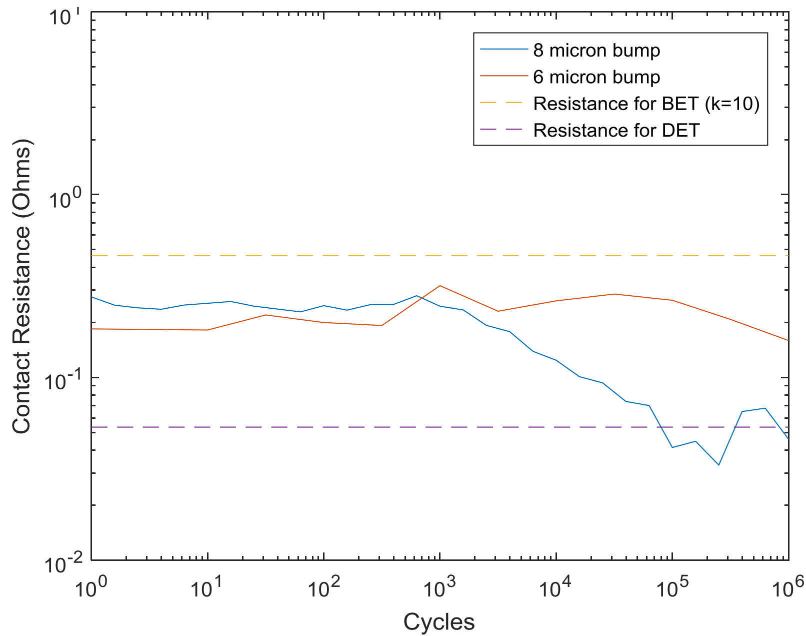

Figure 69. Comparison of the lowest resistances recorded while a force was applied between a contact with a 6 μm upper bump radius and an 8 μm upper bump radius.

4.10 Resistance and Standard Deviation of Micro-contacts

Table 3 shows the resistances of the micro-contacts discussed in the previous sections of Chapter 4 after 10,000 cycles and after 1 million cycles. The table shows that there were two micro-contacts with resistances that were within the ballistic electron transport model for the duration of their testing. It also shows the standard deviation of the resistance calculated from measurements taken after the 100th cycle to the millionth cycle. This was done to avoid incorporating the larger resistances found during the break-in period. The standard deviation was used to determine the variability of the contact resistance which is an indication of whether a micro-contact would be reliable in its lifetime. From the data in Table 3 as well as the analysis in section 4.6, the micro-contact

with small circles separated by 6 μm and actuated with an upper bump with an 8 μm radius was in the ballistic region for the entirety of testing as well as having the smallest standard deviation of resistance out of all the micro-contacts with 3-D surfaces. The combination of the smaller surface areas with larger spacing between them, compared to other designs from the DOE run, appears to have been the reason that this was the best design out of the ones tested.

Table 3. Resistance for certain cycles and standard deviation of the resistance of the devices tested. The green boxes indicate that a device operated within the ballistic electron transport model.

Device	Upper Bump Radius (μm)	Micro-contact Design	Resistance @ 10,000 cycles, 100 μN	Resistance @ 1 mil cycles, 100 μN	Standard Deviation (cycles 100 to 1,000,000)
DOE #1	6	Small SA, circles, 4 μm distance	0.5442	86.47	32.89
DOE #1	8	Small SA, circles, 4 μm distance	0.3506	946.7	685.6
DOE #2	6	Large SA, circles, 4 μm distance	0.1323	0.2155	0.0474
DOE #4	6	Large SA, squares, 4 μm distance	3.939	3.852	0.595
DOE #5	8	Small SA, circles, 6 μm distance	4.407	4.394	0.045
DOE #7	6	Small SA, squares, 6 μm distance	0.4358	0.3947	0.0899
DOE #8	6	Large SA, Squares, 6 μm distance	124.7	307.4	233.48
Control	6	Flat Bottom	0.06039	0.1669	0.0344
Control	8	Flat Bottom	0.2983	0.611	0.257

4.11 Chapter Summary

This chapter discussed the results from the fabrication process and then analyzed the data from testing several of the micro-contacts. The analysis revealed that a few of the

micro-contacts had resistances that within the model for ballistic electron transport. Additionally, comparisons were done to determine if any factors were significant. The next chapter discusses the conclusions reached by the end of research, contributions of this research and provides recommendations for future research.

V. Conclusions and Recommendations

5.1 Chapter Overview

The goal of this research was to fabricate micro-contacts with 3-D surfaces using grayscale lithography and to have them operate in the ballistic electron transport region. This chapter talks about the results, conclusions, and contributions made from the research. It then recommends different topics to research in the future to follow on to this research.

5.2 Conclusions of Research

5.2.1 Micro-contact Surface Engineering

This research demonstrated that it is possible to use grayscale lithography to fabricate micro-contacts with 3-D surfaces and to integrate them into MEMS switches. This was done by patterning 3-D surfaces in photoresist and then transferring the pattern into the silicon nitride layer underneath with the RIE process. The grayscale lithography process was refined during this research to create micro-contacts with surfaces that had a maximum height difference of approximately 1 μm. The patterned 3-D surfaces were suitable to restrict the area where current flows in micro-contacts to have resistances in the ballistic electron transport region during testing. The fabricated micro-contacts with 3-D surfaces were tested to 200 million cycles without any failures and were shown to remain in the ballistic region for up to 1 million cycles. Additionally, micro-contacts with a flat surface were shown to remain in the diffusive region for up to 1 million cycles, which illustrates the effectiveness of using micro-contacts with 3-D surfaces to operate in the ballistic electron transport region. Analysis after testing revealed that a smaller upper

bump was better for contacts to perform in the ballistic electron transport region. The analysis also showed that a larger load applied during cold switching was more likely to have a micro-contact with a resistance in the ballistic regime however it did not determine whether a specific load would cause better longevity. The best micro-contact design for having a stable resistance and remaining in the ballistic transport region for the entirety of testing was made of small circles spaced 6 μm apart which is seen in Figure 76.

5.2.2 Test Stand

The addition of the two digital cameras operated by a laptop replaced the original camera and the wedge beneath the test stand. The cameras were mounted on a moveable platform and could be moved around to see different views of the force sensor and the beams under test. This enabled more precise adjustments to be done with the force sensor to test the micro-contacts.

5.3 Recommendations for Future Research

While there were several conclusions reached from this research, there were also many topics that were not possible to research in this work but are worth investigating in the future. Additionally, several recommendations are mentioned to improve and follow-on to this research.

5.3.1 Additional Testing

There are many tests that can be done to micro-contacts with 3-D surfaces that were not possible to attempt in this research. The first would be to test the 16 designs found in Appendix C that were created outside of the DOE process. Due to time

constraints, these designs were not tested at all. These designs may have resistances that are in the ballistic electron transport region due to the way the current is restricted to specific areas.

A second test would be to cold switch test micro-contacts with 3-D surfaces until failure to determine their longevity and to figure out the failure mechanism that causes the failure with an SEM. This testing would be useful to determine if the micro-contacts with 3-D surfaces are capable of meeting the 200 billion cycle minimum set by industry as well as determining the longevity of micro-contacts operating in the ballistic electron region. It would also help to determine if devices that operate in the ballistic region are less susceptible to electromigration caused by joule heating. Hot switch testing of the micro-contacts could be done to compare the performance of the micro-contacts under cold switch testing. The software currently supports the testing of leading edge, trailing edge, and a combination of both.

The analysis on whether a 1 V or a 0.5 V load would cause a micro-switch to have better longevity was inconclusive in this research due to only running the test for 1 million cycles. This investigation can be continued by cold switching until failure using different voltage loads to determine if there is an optimal voltage for a micro-contact to use for better longevity.

5.3.2 Micro-contact Design

The use of different metals or a protective coating on the bottom 3-D surface may help the devices last longer. The process follower in Appendix B allows for a metal other than gold to be sputtered on the bottom without any extra steps. It is worth investigating whether a harder metal on the bottom surface can increase the number of cycles that a

contact remains in the ballistic electron transport region or whether the effects of electromigration are reduced. Ruthenium oxide and metals from the platinum group would be suitable to use as the bottom metal for this testing.

For this research, the minimum feature sizes were 2 μm and the limit of the resolution of the Heidelberg mask writer was not reached. For future experiments, the design of micro-contacts with surface features at the limit of the Heidelberg mask writer resolution can be done to further restrict the current to smaller areas. With the deposition of a thicker silicon nitride layer, micro-contacts can be designed with higher peaks and can be made narrow by adjusting the selectivity of the RIE process. Designs made this way are worth investigating to determine the number of cycles they remain in the ballistic region.

It is also possible to create micro-contacts with 3-D surfaces using grayscale lithography as a mechanical contact rather than an electrical contact. A 3-D surface can be designed to bond or interlock with another 3-D surface and could reduce or eliminate the amount of epoxy or adhesive used to connect the two surfaces. This has applications in packaging of chips and the fabrication of devices.

5.4 Chapter Summary

Several conclusions have been drawn from this research which contribute to improving the performance of micro-contacts. This research provided insight into using grayscale lithography to fabricate micro-contacts with 3-D surfaces. It demonstrated that micro-contacts with 3-D surfaces are capable of operating within the ballistic electron transport region. Recommendations based on this research were provided to continue

investigating this topic. This research provided insight into using micro-contact physics to better design and fabricate micro-contacts to be suitable for use in industry applications. Continuing to research micro-contacts operating in the ballistic electron transport region is a way ahead to creating micro-contacts that will be used in the next generation of electronic switches and RF applications.

Appendix A. Mask Layouts

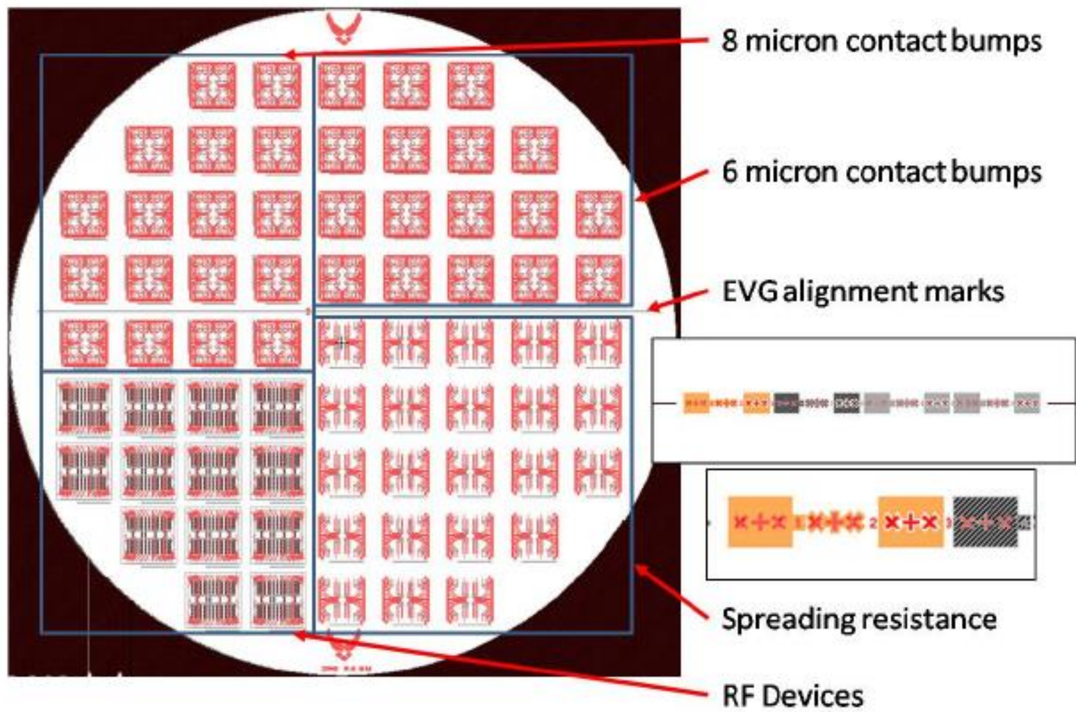

Figure 70. Overlay of five masks that were designed for use with a dual camera alignment system. The mask includes a single horizontal strip and alignment marks. For this research, only the top two regions are used. The top two contain 16 devices per reticle with a fixed-fixed beam with 8 or 6 micron contact bumps [6].

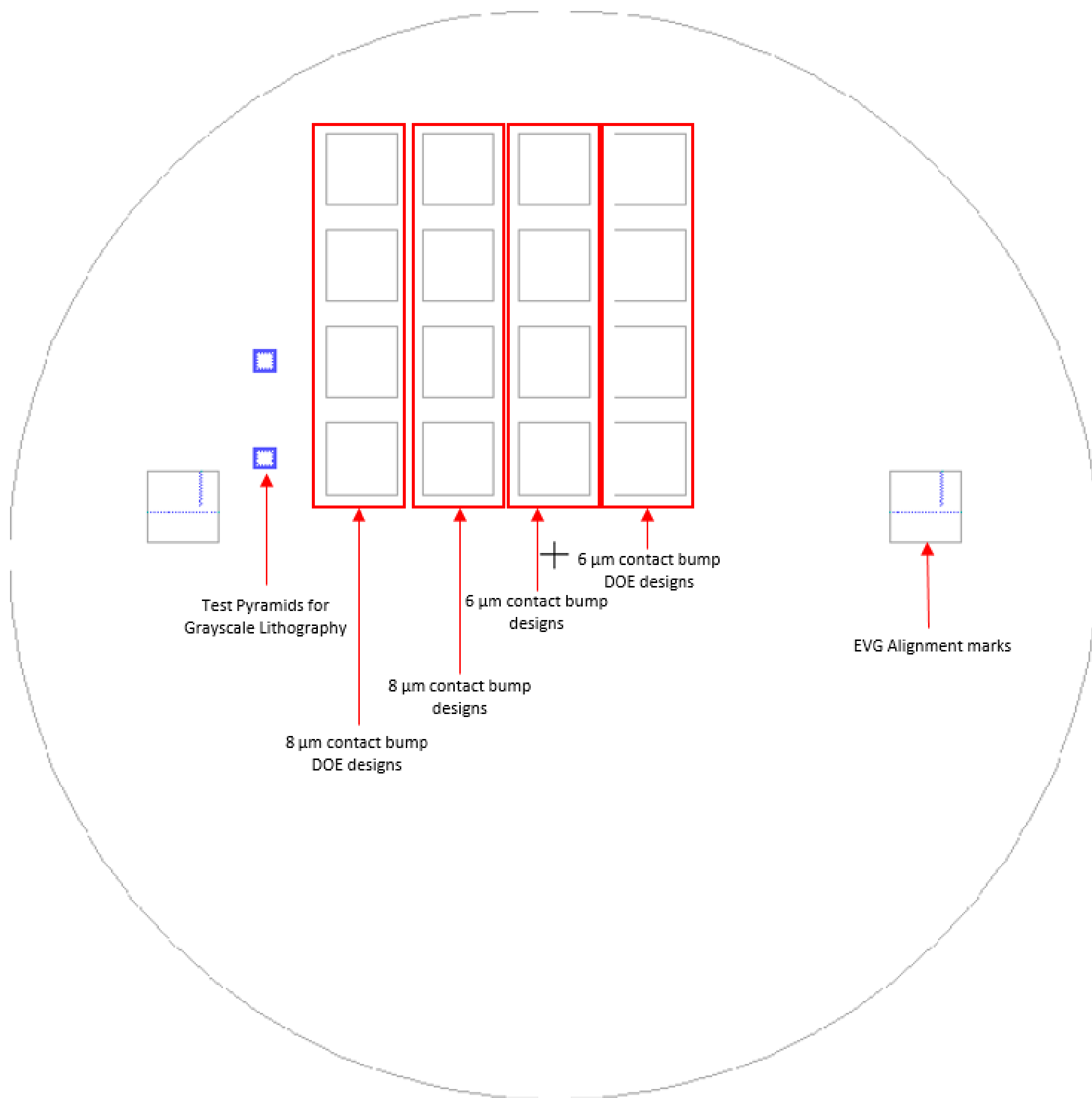

Figure 71. Mask layout for grayscale lithography that lines up with the masks in Figure 70. This is the first lithography step done in the process follower and is a direct write with the Heidelberg mask writer rather than using an actual mask.

Appendix B. Process Followers

The following is a copy of process followers used to create devices for this research.

	Process Step	Notes	Date/Time
	INSPECT WAFER: ☐ Note any defects ☐ For grayscale lithography, use wafer with sufficient Si_2N_3 passivation for pattern transferring (>1 μm minimum)	**Start Date** **Start Time**	
	SOLVENT CLEAN WAFER: ☐ 30 sec acetone rinse at 500 rpm ☐ 30 sec methanol rinse at 500 rpm ☐ 30 sec isopropyl alcohol rinse at 500 rpm ☐ 30 sec DI water rinse at 500 rpm ☐ Dry with nitrogen at 500 rpm ☐ Dry wafer with nitrogen on clean texwipes		
	DEHYDRATION BAKE: ☐ 1 min 110°C hot plate bake		
	For Grayscale Lithography:		
	1818 COAT: ☐ Flood wafer with 1818 ☐ 4 sec spread at 500 rpm ☐ 30 sec spin at 4,000 rpm, ramp = 200 ☐ 75 sec 110°C hot plate bake		
	GRAYSCALE PATTERNING: ☐ Follow grayscale patterning process for patterns required		
	1818 DEVELOP: ☐ 40 sec develop with 351:DI (1:5), use a spin/stop/spin/stop method at 500 rpm ☐ 30 sec DI water rinse at 500 rpm ☐ Dry with nitrogen at 500 rpm ☐ Dry wafer with nitrogen on clean texwipes		
	PATTERN INSPECTION: ☐ Verify patterning and alignment marks are present, fully exposed and clean		
	RIE PATTERN TRANSFER TO NITRIDE LAYER: ☐ Conduct RIE using the following settings o 60 W plasma power o 350 W ICP power o 150 mT pressure o Use O2/ CF4 flow rate ratio of ~0.6 for 1.0 selectivity (20:33 SCCM) o Etch rate ~0.3 μm/min		
	CLEAN AND INSPECT: ☐ Inspect for complete etch, expose longer if needed ☐ When satisfactory, clean the wafer with acetone followed by DI water ☐ Dry wafer with nitrogen		
	SF-11 RESIST COAT: ☐ Flood wafer with SF-11 ☐ 30 sec spin at 4,000 rpm - Hold swab between wafer and Al foil during spin to capture excess photoresist which spins like 'cotton candy' ☐ 2 min 200°C hot plate bake		

	1818 COAT: ☐ Flood wafer with 1818 ☐ 4 sec spread at 500 rpm ☐ 30 sec spin at 4,000 rpm, ramp=200 ☐ 75 sec 110°C hot plate bake		
	EXPOSE 1805 WITH Bottom Metal MASK #1: ☐ Align to alignment marks created during grayscale lithography ☐ 7.0 sec exposure using EVG 620; 7 sec exposure using MJB3		
	1818 DEVELOP: ☐ 40 sec develop with 351:DI (1:5), use a spin/stop/spin/stop method at 500 rpm ☐ 30 sec DI water rinse at 500 rpm ☐ Dry with nitrogen at 500 rpm ☐ Dry wafer with nitrogen on clean texwipes		
	INSPECT RESIST: ☐ Inspect photoresist under microscope, look for fringe patterns indicating residual SF-11		
	SF-11 EXPOSURE (~1.5 um / cycle): ☐ Place wafer in center of circle ☐ 300 sec DUV exposure with OAI DUV		
	SF-11 DEVELOP: ☐ 60 sec bucket develop with SAL 101 ☐ 30 sec DI rinse at 500 RPM or hold under DI faucet for 30 sec ☐ Dry with nitrogen at 500 RPM ☐ Dry wafer with nitrogen on clean texwipes		
	INSPECT RESIST: ☐ Inspect photoresist under microscope		
	TENCOR MEASUREMENT: ☐ Measure metal step height T _________ C __________ B ________		
	ASHER DESCUM ☐ 4 min, 75W, LFE Barrel Asher - Immediately before Evaporation		
	BOTTOM METAL DEPOSITION ☐ *Evaporate* 200 Å Ti / 2800 Å Au		
	LIFT-OFF METAL: ☐ Heat 1165 remover to 90°C (set hot plate to 170°C) ☐ 5 min ultrasonic bath in acetone ☐ 30 sec acetone rinse at 500 rpm ☐ 30 sec isopropyl alcohol rinse at 500 rpm ☐ 30 sec DI water rinse at 500 rpm ☐ Dry with nitrogen at 500 rpm ☐ 5 min soak in 1165 at 90º C ☐ 30 sec DI rinse at 500 rpm ☐ Dry wafer with nitrogen on clean texwipes		
	INSPECT METAL: ☐ Inspect metal under microscope		
	ASHER DESCUM ☐ 4 min, 150W, LFE Barrel Asher		
	TENCOR MEASUREMENT: ☐ Measure metal step height T ________ C __________ B ___________		
	Electrical Isolation Test: ☐ Verify electrical isolation between contact pads		

	Process Step	Notes	Date/Time
	DEHYDRATION BAKE: ☐ 5 min 110°C hot plate bake	**Start Date** **Start Time**	
	FIRST SF-11 (PMGI) COAT: ☐ Flood wafer with SF-11 ☐ 30 sec spin at 4,000 rpm, ramp= 999, 5 sec spread=500 ☐ 2 min 200º hot plate bake		
	SECOND SF-11 (PMGI) COAT: ☐ Flood wafer with SF-11 ☐ 30 sec spin at 4,000 rpm ☐ 2 min 200º hot plate bake		
	1818 COAT: ☐ Flood wafer with 1818 ☐ 4 sec spread at 500 rpm ☐ 30 sec spin at 4,000 rpm, ramp=200 ☐ 75 sec 110°C hot plate bake		
	EXPOSE 1818 WITH Anchor MASK #3: ☐ Align to bottom metal alignment marks ☐ 7.0 sec exposure using EVG 620; 7 sec exposure using MJB3		
	1818 DEVELOP: ☐ 40 sec develop with 351:DI (1:5), use a spin/stop/spin/stop method at 500 rpm ☐ 30 sec DI water rinse at 500 rpm ☐ Dry with nitrogen at 500 rpm ☐ Dry wafer with nitrogen on clean texwipes		
	INSPECT RESIST: ☐ Inspect photoresist under microscope		
	FIRST DUV EXPOSURE (~1.5 um / cycle): ☐ Place wafer in center of circle ☐ 200 sec DUV exposure with OAI DUV		
	SF-11 DEVELOP: ☐ 60 sec develop with SAL 101, use a spin/stop/spin/stop method at 500 rpm ☐ 30 sec DI rinse at 500 RPM ☐ Dry with nitrogen at 500 RPM ☐ Dry wafer with nitrogen on clean texwipes		
	INSPECT RESIST: ☐ Inspect photoresist under microscope, look for fringe patters indicating residual SF-11		
	SECOND DUV EXPOSURE (~1.5 um / cycle): ☐ Place wafer in center of circle ☐ 200 sec DUV exposure with OAI DUV		
	SF-11 DEVELOP: ☐ 60 sec develop with SAL 101, use a spin/stop/spin/stop method at 500 rpm ☐ 30 sec DI rinse at 500 RPM ☐ Dry with nitrogen at 500 RPM ☐ Dry wafer with nitrogen on clean texwipes		
	INSPECT RESIST: ☐ Inspect photoresist under microscope, look for fringe patters indicating residual SF-11		
	TENCOR MEASUREMENT: ☐ Measure metal step height T _________ C __________ B ________		

	REMOVE 1818: ☐ Redevelop with 351:DI (1:5) ☐ 40 sec develop at 500 rpm ☐ 30 sec DI water rinse at 500 rpm ☐ Dry with nitrogen at 500 rpm ☐ Dry wafer with nitrogen on clean texwipes	Remaining 1818 is exposed to UV during DUV. Developing it removes the remaining 1818	
	INSPECT RESIST: ☐ Inspect photoresist under microscope		
	TENCOR MEASUREMENT: ☐ Measure metal step height T _________ C ___________ B _______		
	1818 COAT: ☐ Flood wafer with 1818 ☐ 4 sec spread at 500 rpm ☐ 30 sec spin at 4,000 rpm, ramp =200 ☐ 75 sec 110ºC hot plate bake		
	EXPOSE 1818 WITH Contact Bump MASK #4: ☐ Align to bottom metal alignment marks ☐ 7 sec exposure using EVG 620; 7 sec exposure using MJB3		
	1818 DEVELOP: ☐ 40 sec develop with 351:DI (1:5), use a spin/stop/spin/stop method at 500 rpm ☐ 30 sec DI water rinse at 500 rpm ☐ Dry with nitrogen at 500 rpm ☐ Dry wafer with nitrogen on clean texwipes		
	INSPECT RESIST: ☐ Inspect photoresist under microscope		
	TENCOR MEASUREMENT: ☐ Measure metal step height T _________ C __________ B ______		
	PARTIAL DUV EXPOSURE (~0.7um BUMP DEPTH): ☐ 60 sec DUV exposure @ 35 mW/cm^2 , 254 nm		
	SF-11 DEVELOP: ☐ 60 sec develop with SAL 101, use a spin/stop/spin/stop method at 500 rpm ☐ 30 sec DI rinse at 500 RPM ☐ Dry with nitrogen at 500 RPM ☐ Dry wafer with nitrogen on clean texwipes		
	INSPECT RESIST: ☐ Inspect photoresist under microscope		
	TENCOR MEASUREMENT: ☐ Measure metal step height T __________ C _________ B _______		
	REMOVE 1818: ☐ 40 sec develop with 351:DI (1:5), use a spin/stop/spin/stop method at 500 rpm ☐ 30 sec DI water rinse at 500 rpm ☐ Dry with nitrogen at 500 rpm ☐ Dry wafer with nitrogen on clean texwipes		
	INSPECT RESIST: ☐ Inspect photoresist under microscope		

	TENCOR MEASUREMENT: ☐ Measure metal step height T ________ C ________ B ________		
	ASHER DESCUM ☐ 8 min, 75W, LFE Barrel Asher		
	TENCOR MEASUREMENT: ☐ Measure metal step height T ________ C _________ B ________		
	ANCHOR AND BUMP REFLOW & INSPECT WAFER: ☐ 7 sec 270ºC hot plate bake		
	TENCOR MEASUREMENT: ☐ Measure metal step height T __________ C _________ B ________		

	Process Step	Notes	Date/Time
	ASHER DESCUM: ☐ 4 min, 75W, LFE Barrel Asher	**Start Date** **Start Time**	
	SPUTTER CONTACT METAL LAYER: ☐ Sputter bottom contact metal (optional) ☐ Sputter 2000 Å Au using Discovery-18		
	AZ5214 COAT: ☐ Flood wafer with AZ5214 ☐ 4 sec spread at 300 rpm ☐ 30 sec spin at 3,000 rpm, ramp=500 ☐ 5 min 110°C hot plate bake		
	EXPOSE AZ5214 WITH Bridge Metal MASK: ☐ Align to bottom metal alignment marks ☐ 7 sec exposure using EVG 620;		
	AZ5214 DEVELOP: ☐ 70 sec develop with 300MIF at 500 rpm ☐ 30 sec DI water rinse at 500 rpm ☐ Dry with nitrogen at 500 rpm ☐ Dry wafer with nitrogen on clean texwipes		
	INSPECT RESIST: ☐ Inspect photoresist under microscope		
	TENCOR MEASUREMENT: ☐ Measure metal step height T _______________ C _______________ B _______________		
	SOLVENT BAKE: ☐ Bake in 110ºC oven for 20 min		
	ASHER DESCUM ☐ 4 min, 75W, LFE Barrel Asher		
	Electroplate BRIDGE METAL LAYER: ☐ Electroplate 6 µm Au using Electroplate Bath ☐ ~0.3 – 0.45 A-mn ☐ Wait until temperature is 58.5ºC		
	TENCOR MEASUREMENT: ☐ Measure metal step height T _______________ C _______________ B _______________		
	DICE WAFER: ☐ Send wafer to AFRL for dicing process. Leave adhesive on back side of wafer until ready to wire bond devices		
	REMOVE AZ5214: ☐ 30 sec acetone rinse at 500 rpm ☐ 30 sec isopropyl alcohol rinse at 500 rpm ☐ 30 sec DI water rinse at 500 rpm ☐ Dry with nitrogen at 500 rpm ☐ Dry wafer with nitrogen on clean texwipes		
	ASHER DESCUM ☐ 2 min, 75W, LFE Barrel Asher		
	CONTACT METAL ETCH: ☐ 40 sec Au Etchant, agitated ☐ 30 sec DI water rinse (stops the etching) ☐ Dry with nitrogen on clean texwipes		

	INSPECT CONTACT METAL: ☐ Make sure contact metal layer is completely removed		
	ASHER DESCUM: ☐ 5 min, 150W, LFE Barrel Asher		
	STRIP SF-11 SACRIFICIAL LAYER (RELEASE PROCESS): ☐ Do NOT place devices in ultrasonic bath ☐ Place devices in 1165 at room temperature ☐ Heat 1165 remover to 90ºC (set hot plate to 120ºC) ☐ 35 min soak in 1165 at 90ºC ☐ Wet transfer from 1165 beaker to 1st IPA in petri dish, 30 sec soak ☐ Wet transfer to 2nd IPA in petri dish, 30 sec soak ☐ Wet transfer to 3rd IPA in petri dish, 30 sec soak ☐ Wet transfer to 4th IPA in petri dish, 30 sec soak ☐ Wet transfer to 1st methanol in petri dish, 30 sec soak ☐ Wet transfer to 2nd methanol in petri dish, 30 sec soak ☐ Wet transfer to 3rd methanol in petri dish, 30 sec soak ☐ Wet transfer to 4th methanol in petri dish, 30 sec soak ☐ Fill CO2 dryer chamber with enough methanol to cover the wafer ☐ Remove wafer from 4th methanol dish and place in CO2 dryer chamber ☐ Immediately cover CO2 dryer and start process		
	ASHER DESCUM ☐ 15-30 min, 75W, LFE Barrel Asher		

Appendix C. Grayscale Designs

The following are micro-contact designs created in L-Edit along with microscope images of the micro-contact after grayscale lithography, RIE, and gold evaporation. For the L-Edit designs, the highest point of the contact is in white, and the lowest point is in dark blue.

Designs made with the DOE process:

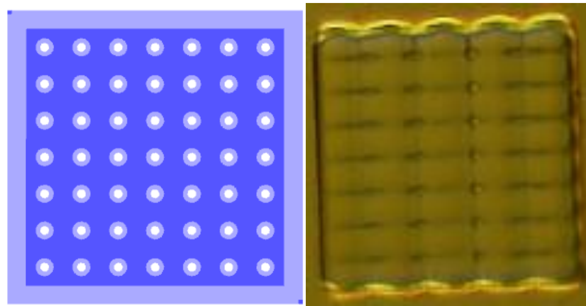

Figure 72. DOE design #1: small circles 4 µm apart

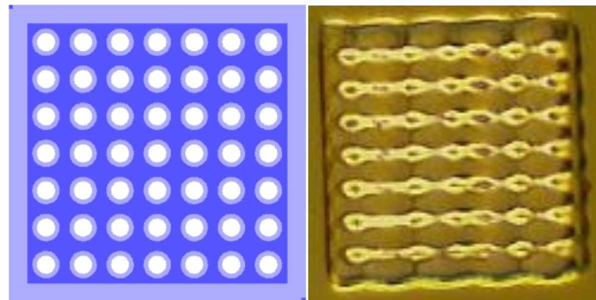

Figure 73. DOE design #2: large circles 4 µm apart

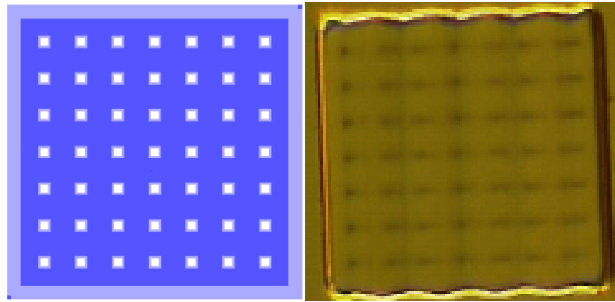

Figure 74. DOE design #3: small squares 4 μm apart

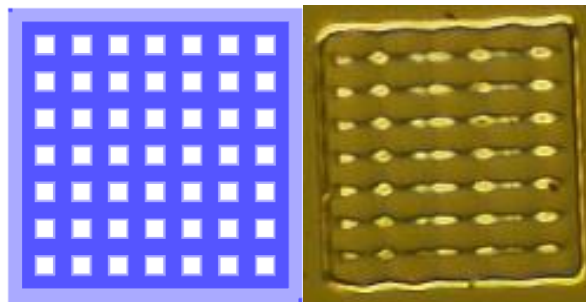

Figure 75. DOE design #4: large squares 4 μm apart

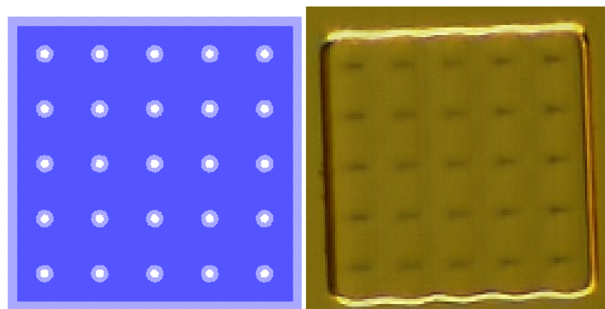

Figure 76. DOE design #5: small circles 6 μm apart

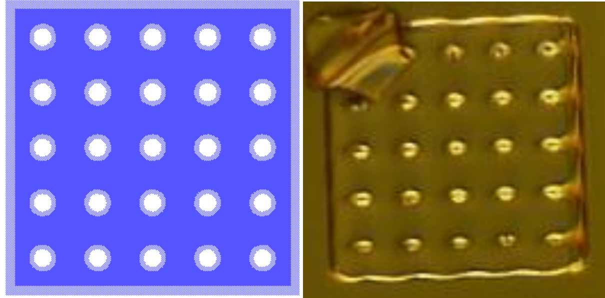

Figure 77. DOE design #6: large circles 6 µm apart

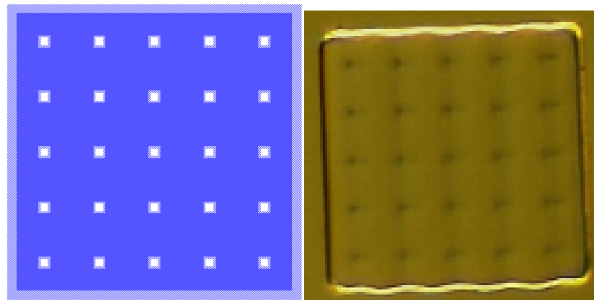

Figure 78. DOE design #7: small squares 6 µm apart

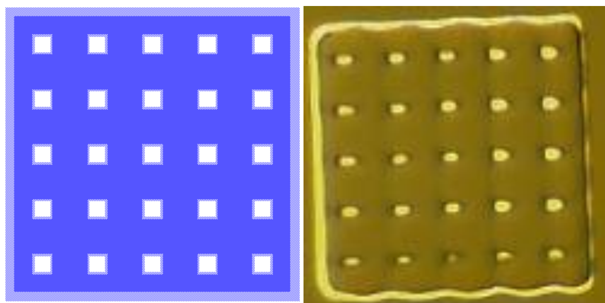

Figure 79. DOE design #8: large squares 6 µm apart

Miscellaneous designs:

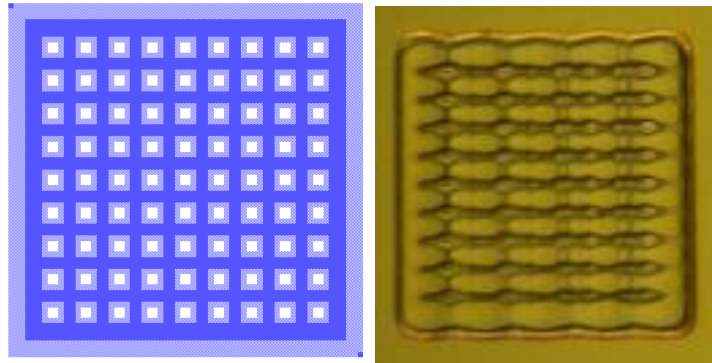

Figure 80. Miscellaneous design #1

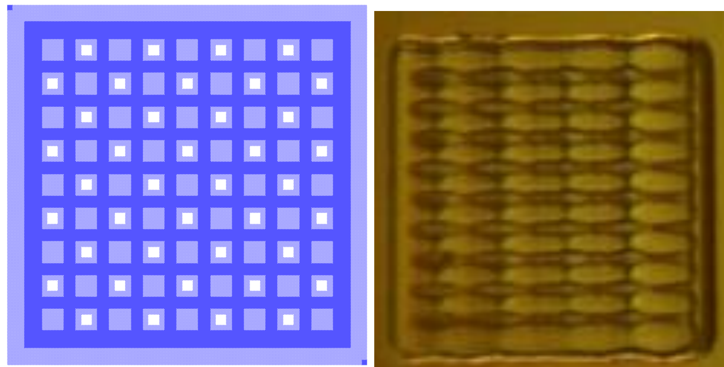

Figure 81. Miscellaneous design #2

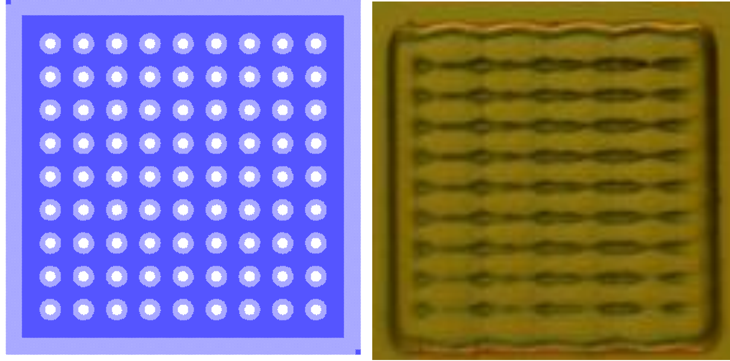

Figure 82. Miscellaneous design #3

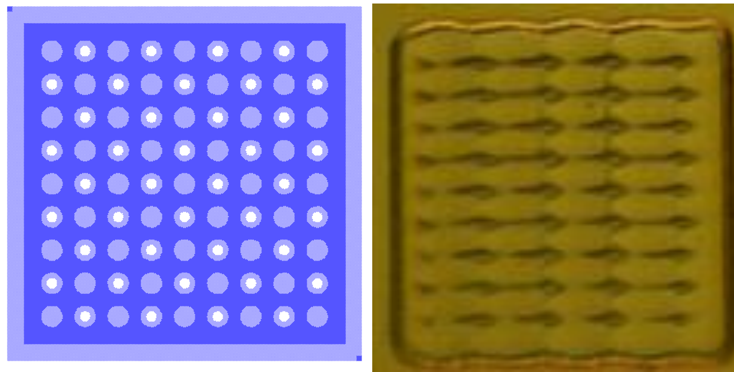

Figure 83. Miscellaneous design #4

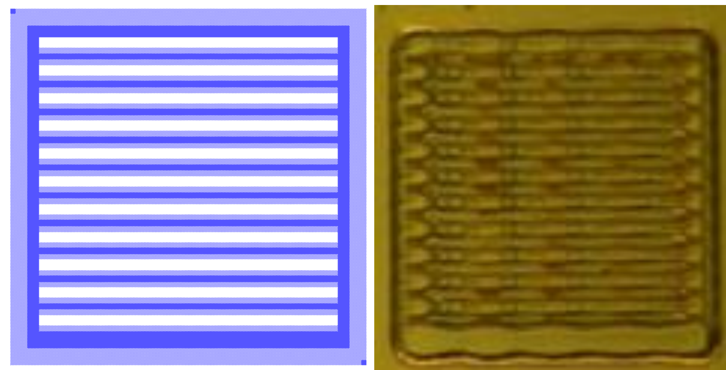

Figure 84. Miscellaneous design #5

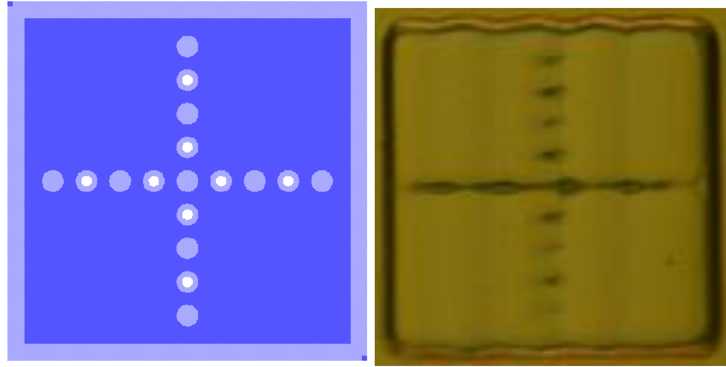

Figure 85. Miscellaneous design #6

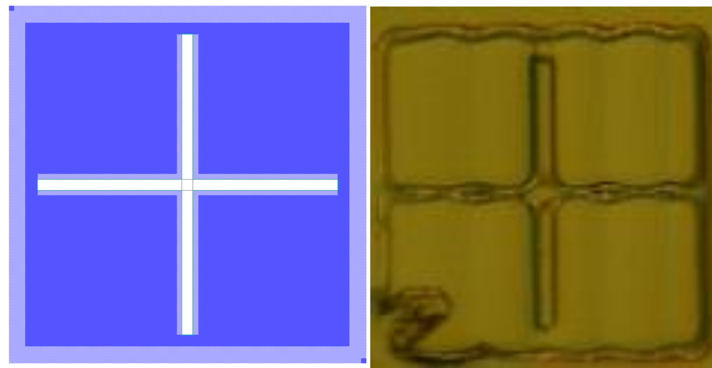

Figure 86. Miscellaneous design #7

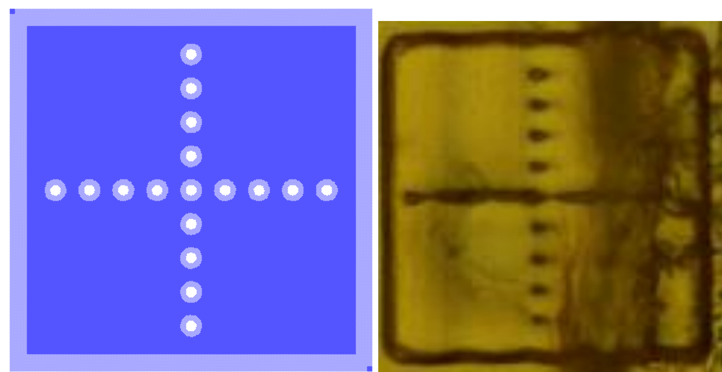

Figure 87. Miscellaneous design #8

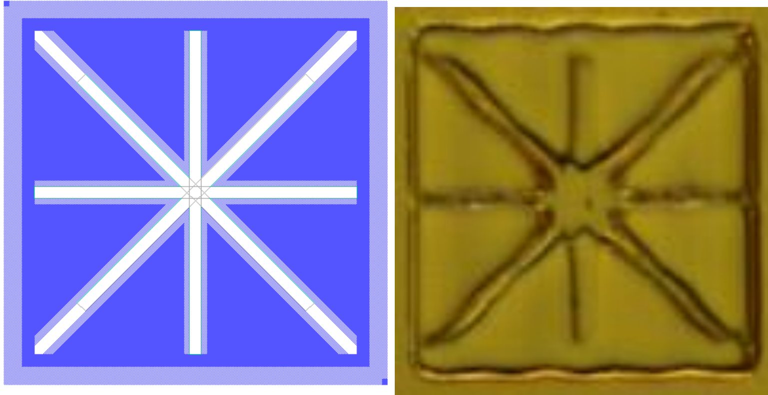

Figure 88. Miscellaneous design #9

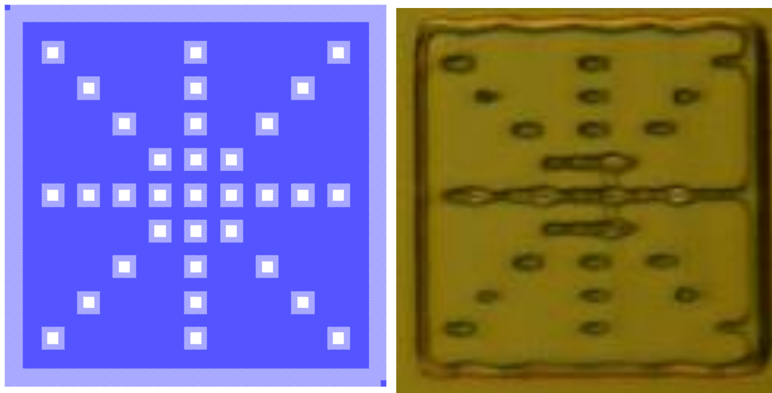

Figure 89. Miscellaneous design #10

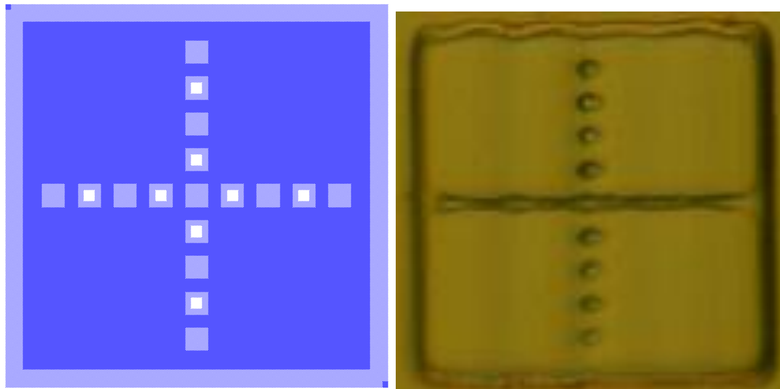

Figure 90. Miscellaneous design #11

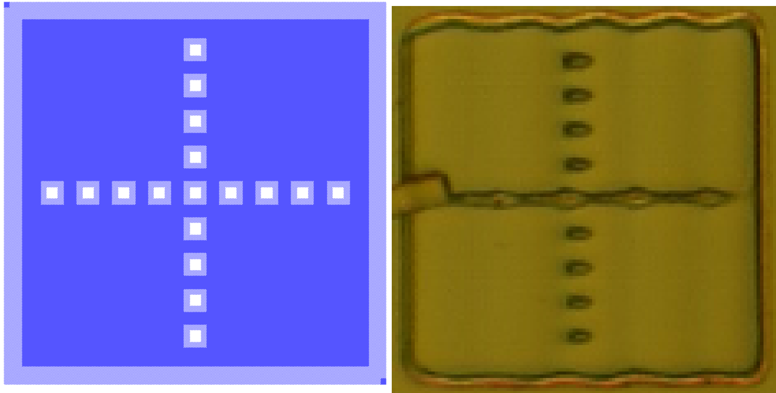

Figure 91. Miscellaneous design #12

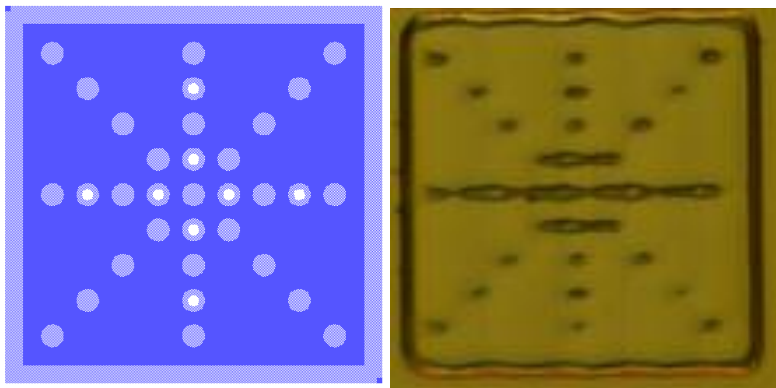

Figure 92. Miscellaneous design #13

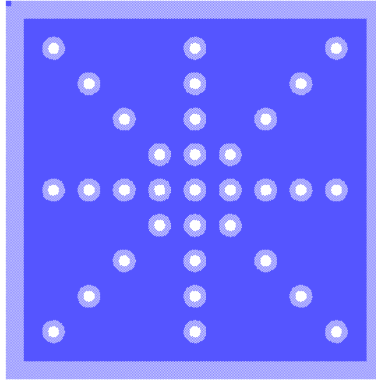

Figure 93. Miscellaneous design #14

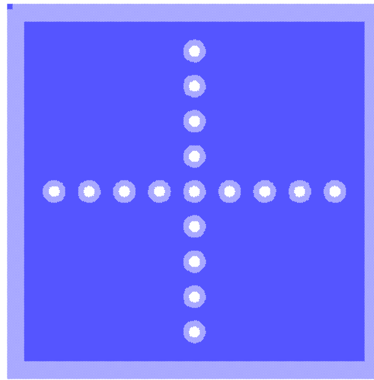

Figure 94. Miscellaneous design #15

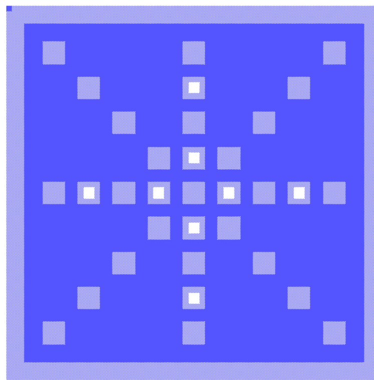

Figure 95. Miscellaneous design #16

Appendix D. MATLAB Code

MATLAB code used to create plots to model ballistic and diffuse electron transport:

```
result = zeros(10000,1);
t = 1;
for K = 0.01:0.01:100
   f = @(x) exp(-K.*x).*sin(x)./x;
   result(t,1) = (2./pi).*integral(f,0,Inf);
   t = t+1;
end

k = 0.01:0.01:100;
figure(1)
semilogx(k,result)
xlabel('Knudsen #, K')
ylabel('Gamma(K)')

%variables
rho = 2.8505E-8;
H = 2.45E9;
Fc = 1E-6:1E-6:250E-6;
thick = 280E-9; %thickness of the deposited metal
nu = 0.42; %off a website
Ky = 1.12828+1.158*nu;

beta = sqrt(H.*pi.*(1.062+0.354.*(2.*Ky./3-3))./Fc);


knudsen = logspace(-2,2,10); %creates a 10 number long vector log

gamma = zeros(1,10);
u = 1;
for L = logspace(-2,2,10)
   f = @(x) exp(-L.*x).*sin(x)./x;
   gamma(1,u) = (2./pi).*integral(f,0,Inf);
   u = u+1;
end

RcBEP = zeros(10,250);
RcDEP = zeros(10,250);
RWEP  = zeros(10,250);
RWEP2 = zeros(10,250);

loopvar = 1;
for loop = 1:1:10
   RcBEP(loopvar,:) = 4.*rho.*knudsen(1,(11-loopvar)).*beta./(3.*pi);
   RcDEP(loopvar,:) = (rho./2).*beta;

   RWEP(loopvar,:) = RcBEP(loopvar,:) +
gamma(1,loopvar).*RcDEP(loopvar,:);
```

```
   loopvar=loopvar+1;
end

figure(2)
plot(Fc,RWEP(10,:),Fc,RWEP(8,:),Fc, RWEP(6,:),Fc, RWEP(4,:),Fc,
RWEP(2,:),Fc, RcDEP(1,:),'--','LineWidth',1)
ylim([0,0.5])
xlabel('Contact Force, N')
ylabel('Contact Resistance')
legend('Ballistic, K=.01','Ballistic, K=.0774','Ballistic,
K=0.5995','Ballistic, K=4.6416','Ballistic, K=35.9381','Diffuse Only' )

figure(3)
semilogy(Fc,RWEP(10,:),Fc,RWEP(8,:),Fc, RWEP(6,:),Fc, RWEP(4,:),Fc,
RWEP(2,:),Fc, RcDEP(1,:),'--','LineWidth',1)
xlabel('Contact Force, N')
ylabel('Contact Resistance')
legend('Ballistic, K=.01','Ballistic, K=.0774','Ballistic,
K=0.5995','Ballistic, K=4.6416','Ballistic, K=35.9381','Diffuse Only' )

figure(4)
semilogy(Fc,RWEP(1,:),Fc, RcDEP(1,:),'--')
xlabel('Contact Force, N')
ylabel('Contact Resistance')
legend('Purely Ballistic, K=10', 'Purely Diffuse, no K component')
```

MATLAB code used to compare the resistance models to data:

```
clear
%theoretical

%constants
rho = 2.8505E-8;
R = 6E-6;   %asperity peak radius of curvature
H = 2.45E9; %meyer hardness of au
Fc = 1E-6:1E-6:250E-6;
thick = 280E-9; %thickness of the deposited metal
nu = 0.42; %off a website
Ky = 1.12828+1.158*nu;
E = 78E9;   %Young's modulus for Au
Einv = 2*(1-nu^2)/E
ET = inv(Einv)

beta = sqrt(H.*pi.*(1.062+0.354.*(2.*Ky./3-3))./Fc);

RcDEP = (rho./2).*beta; %Model of Elastic-Plastic
RcDE = (rho./2).*(4.*ET./(3.*Fc.*R)).^(1/3);    %Model for Elastic
RcDP = (rho./2).*sqrt(H.*pi./Fc);               %Model for Plastic

%ballistic
knudsen = 10; %assumption to assume that it's ballistic
%it's technically mean free length/reff
RcB = 4.*rho.*knudsen.*beta./(3.*pi);

figure(1)
semilogy(Fc, RcDEP, Fc, RcDP, Fc, RcDE, Fc, RcB)
xlabel('Contact Force, uN')
ylabel('Contact Resistance')
legend('RcDEP', 'RcDP', 'RcDE', 'RcB')

%actual data to compare with
% data =
importdata('thesis_data\wafer7\chip1\1_4\1to1mil\1v\test01_0001.lvm')
data =
importdata('thesis_data\wafer7\control\1_2\1to1bil\1v\test01_0015.lvm')
;

Volt_meas=data(:,2);
Cur_meas=data(:,3);
Res_meas=data(:,4);
Adj_Force=data(:,5);
Tot_Force=data(:,7);
Dist=data(:,8);
Step_Num=data(:,9);

counter = 1;
[stop, x] =size(Adj_Force)

while counter < stop
```

```
    if Adj_Force(counter,1)== 0
       start = counter
       break
    end
    counter = counter +1

end

figure(2)
semilogy(Adj_Force(start:stop), Res_meas(start:stop))
xlabel('Contact Force, uN')
ylabel('Contact Resistance')

figure(3)
semilogy(Fc, RcDE,Fc, RcB, Adj_Force(start:stop).*(10^-6),
Res_meas(start:stop))
xlabel('Contact Force, uN')
ylabel('Contact Resistance')
legend('RcDE', 'RcB', 'data')
title('wafer7\control\1_2\1to1bil\1v\test01_0015')
```

MATLAB code used to import data measured by the test stand:

```
pwd
data =
importdata('thesis_data\wafer7\control\3_4\1to1mil\halfv\test01_0019.lv
m')

Volt_meas=data(:,2);
Cur_meas=data(:,3);
Res_meas=data(:,4);
Adj_Force=data(:,5);
Tot_Force=data(:,7);
Dist=data(:,8);
Step_Num=data(:,9);

figure(1)
semilogy(Adj_Force, Res_meas)
%ylim([0,100])
xlabel('Contact Force, uN')
ylabel('Contact Resistance')

Adj_Force(2,1)
counter = 1;
[stop, x] =size(Adj_Force)

%only graph part of curve that is usable
while counter < stop

    if Adj_Force(counter,1)== 0
       start = counter
       break
    end
    counter = counter +1

end

figure(2)
semilogy(Adj_Force(start:stop), Res_meas(start:stop))
xlabel('Contact Force, uN')
ylabel('Contact Resistance')
%title('wafer7\control\1_2\1to1bil\1v\test01_0010')

minimum_res = min(Res_meas)
```

MATLAB code used to graph the data compared to ballistic and electron transport models:

```
%used to graph resistance vs cycle of contacts that are probably
undergoing
%diffusive electron transport

x = logspace(1,6,11);
data =importdata('thesis_data\Control_3_4_longevity.xlsx');
newdata = struct2cell(data);

Measurement_num = newdata{1,1}(:,1);
cycle = newdata{1,1}(:,4);

Resist_100uN_1 = newdata{1,1}(:,2);
Resist_lowest_1 = newdata{1,1}(:,3);

ball_10k_100uN = newdata{1,1}(:,5);
ball_10k_lowest = newdata{1,1}(:,6);

elastic_100uN = newdata{1,1}(:,7);
elastic_lowest = newdata{1,1}(:,8);

figure(1)
loglog(cycle, Resist_100uN_1, cycle, ball_10k_100uN, '--',cycle,
elastic_100uN, '--' )
ylim([.001,10])
xlabel('Cycles')
ylabel('Contact Resistance (Ohms)')
legend('Control Micro-contact', 'Resistance for BET (k=10)',
'Resistance for DET')
title('Resistance at 100 uN of Control u-contact over 200 mil cycles')

figure(2)
loglog(cycle, Resist_lowest_1, cycle, ball_10k_lowest, '--',cycle,
elastic_lowest, '--' )
ylim([.001,10])
xlabel('Cycles')
ylabel('Contact Resistance (Ohms)')
legend('Control Micro-contact', 'Resistance for BET (k=10)',
'Resistance for DET')
title('Lowest Resistance of Control u-contact over 200 mil cycles')
```

MATLAB code used to graph data to compare with ballistic electron transport models:

```
%Used to graph resistance vs cycle of contacts that look like they
undergo
%ballistic electron transport
x = logspace(1,6,11);
y = logspace(0,9,28);
y =transpose(y)

data =importdata('thesis_data\W7_Chip1_1_4_longevity.xlsx');
newdata = struct2cell(data);

Measurement_num = newdata{1,1}(:,1);
cycle = newdata{1,1}(:,4);

Resist_100uN_1 = newdata{1,1}(:,2);
Resist_lowest_1 = newdata{1,1}(:,3);

ball_10k_100uN = newdata{1,1}(:,5);
ball_10k_lowest = newdata{1,1}(:,6);
ball_100k_100uN = newdata{1,1}(:,7);
ball_100k_lowest = newdata{1,1}(:,8);

figure(1)
loglog(cycle, Resist_100uN_1, cycle, ball_10k_100uN, '--',cycle,
ball_100k_100uN, '--' )
ylim([.1,10000])
xlabel('Cycles')
ylabel('Contact Resistance (Ohms)')
legend('Grayscale Micro-contact', 'Resistance for BET (k=10)',
'Resistance for BET (k=100)')
title('Resistance at 100 uN of Grayscale u-contact over 1 mil cycles')

figure(2)
loglog(cycle, Resist_lowest_1, cycle, ball_10k_lowest, '--',cycle,
ball_100k_lowest, '--' )
ylim([.1,10000])
xlabel('Cycles')
ylabel('Contact Resistance (Ohms)')
legend('Grayscale Micro-contact', 'Resistance for BET (k=10)',
'Resistance for BET (k=100)')
title('Lowest Resistance of Grayscale u-contact over 1 mil cycles')
```

Bibliography

[1] R. A. Coutu, “When will MEMS switches be ready for commercial products?,” *Int. J. Biosens. Bioelectron.*, vol. 3, no. 4, 2017.

[2] K. Van Caekenberghe, “RF MEMS on the radar,” *IEEE Microw. Mag.*, 2009.

[3] A. Basu, G. G. Adams, and N. E. McGruer, “A review of micro-contact physics, materials, and failure mechanisms in direct-contact RF MEMS switches,” *Journal of Micromechanics and Microengineering*. 2016.

[4] A. Basu, R. Hennessy, G. Adams, and N. McGruer, “Reliability in hot switched ruthenium on ruthenium MEMS contacts,” in *Proceedings of the 59th IEEE Holm Conference on Electrical Contacts, HOLM 2013*, 2013.

[5] R. P. Hennessy, A. Basu, G. G. Adams, and N. E. McGruer, “Hot-switched lifetime and damage characteristics of MEMS switch contacts,” *J. Micromechanics Microengineering*, 2013.

[6] T. V. Laurvick, “Improvements to Micro-contact Performance and Reliability,” 2016.

[7] B. F. Toler, R. A. Coutu, and J. W. McBride, “A review of micro-contact physics for microelectromechanical systems (MEMS) metal contact switches,” *Journal of Micromechanics and Microengineering*. 2013.

[8] C. Stilson, “Contact Resistance Evolution and Degradation of Highly Cycled Micro-contacts,” 2014.

[9] A. Broue *et al.*, “Characterization of Au/Au, Au/Ru and Ru/Ru ohmic contacts in MEMS switches improved by a novel methodology,” in *Proceedings of SPIE*, 2010.

[10] S. Majumder, N. E. McGruer, G. G. Adams, P. M. Zavracky, R. H. Morrison, and J. Krim, “Study of contacts in an electrostatically actuated microswitch,” *Sensors Actuators, A Phys.*, 2001.

[11] R. A. Coutu, J. R. Reid, R. Cortez, R. E. Strawser, and P. E. Kladitis, “Microswitches with sputtered Au, AuPd, Au-on-AuPt, and AuPtCu alloy electric contacts,” *IEEE Trans. Components Packag. Technol.*, 2006.

[12] W. R. Chang, “An elastic-plastic contact model for a rough surface with an ion-

plated soft metallic coating," *Wear*, 1997.

[13] B. Toler, C. Stilson, and R. Coutu, "Contact resistance evolution of au-au micro-contacts with encapsulated AG colloids," in *Proceedings of the 59th IEEE Holm Conference on Electrical Contacts, HOLM 2013*, 2013.

[14] S. Karmalkar, P. V. Mohan, and B. P. Kumar, "A unified compact model of electrical and thermal 3-D spreading resistance between eccentric rectangular and circular contacts," *IEEE Electron Device Lett.*, 2005.

[15] R. S. Timsit, "Constriction resistance of thin film contacts," *IEEE Trans. Components Packag. Technol.*, 2010.

[16] P. Zhang, Y. Y. Lau, and R. S. Timsit, "Spreading resistance of a contact spot on a thin film," in *Proceedings of the 59th IEEE Holm Conference on Electrical Contacts, HOLM 2013*, 2013.

[17] P. Zhang, Y. Y. Lau, and R. M. Gilgenbach, "Thin film contact resistance with dissimilar materials," *J. Appl. Phys.*, 2011.

[18] K. B. Lee, *Principles of Microelectromechanical Systems*. 2010.

[19] R. Jaeger, *Introduction to Microelectronic Fabrication*, Second Edi. Prentice Hall, 2002.

[20] C. McKenna, K. Walsh, M. Crain, and J. Lake, "Maskless direct write grayscale lithography for MEMS applications," in *Biennial University/Government/Industry Microelectronics Symposium - Proceedings*, 2010.

[21] J. Loomis, D. Ratnayake, C. McKenna, and K. M. Walsh, "Grayscale lithography—automated mask generation for complex three-dimensional topography," *J. Micro/Nanolithography, MEMS, MOEMS*, 2016.

[22] C. Stilson, R. Pal, and R. A. Coutu, "Fabrication of 3D surface structures using grayscale lithography," in *Proceedings of SPIE*, 2014.

[23] T. Laurvick and R. A. Coutu, "Improved grayscale lithography," in *Proceedings of the IEEE National Aerospace Electronics Conference, NAECON*, 2017.

[24] M. Braunovic, V. V. Konchits, and N. K. Myshkin, *Electrical contacts: Fundamentals, applications and technology*. 2017.

[25] W. Merlijn Van Spengen, R. Puers, and I. De Wolf, "A physical model to predict stiction in MEMS," *J. Micromechanics Microengineering*, 2002.

[26] B. D. Beake, T. W. Liskiewicz, and J. F. Smith, "Deformation of Si(100) in spherical contacts - Comparison of nano-fretting and nano-scratch tests with nano-indentation," *Surf. Coatings Technol.*, 2011.

[27] C. Stilson and R. Coutu, "Reliability Evolution of Au-Au, Au-Ru and Au-RuO2 Micro-Contacts," in *Proceedings of the 27th International Conference on Electrical Contacts; ICEC 2014*, 2014.

[28] T. V. Laurvick and R. A. Coutu, "Micro-contact performance and reliability under low frequency, low amplitude, alternating current (AC) test conditions," in *Electrical Contacts, Proceedings of the Annual Holm Conference on Electrical Contacts*, 2015.

[29] D. J. Dickrell and M. T. Dugger, "Electrical contact resistance degradation of a hot-switched simulated metal MEMS contact," *IEEE Trans. Components Packag. Technol.*, 2007.

[30] T. G. Bull and J. W. McBride, "In-Situ Contact Surface Charaterization in a MEMS Ohmic Switch under Low Current Switching," *MDPI Technol.*, vol. 6, no. 47, 2018.

[31] R. A. Coutu, J. W. McBride, and L. V. A. Starman, "Improved micro-contact resistance model that considers material deformation, electron transport and thin film characteristics," in *Electrical Contacts, Proceedings of the Annual Holm Conference on Electrical Contacts*, 2009.

[32] B. Arrazat, K. Inal, and P. Gergaud, "Investigation of boron and nitrogen ion beam implantation in gold thin films for ohmic MEMS switch contact improvement," in *2013 Transducers and Eurosensors XXVII: The 17th International Conference on Solid-State Sensors, Actuators and Microsystems, TRANSDUCERS and EUROSENSORS 2013*, 2013.

[33] A. Peschot, C. Poulain, N. Bonifaci, and O. Lesaint, "Contact bounce phenomena in a MEM switch," in *Electrical Contacts, Proceedings of the Annual Holm Conference on Electrical Contacts*, 2012.

[34] C. Stilson, T. Laurvick, and R. Coutu, "Contact resistance evaluation of micro-contacts with upper hemisphere and lower planar or engineered surfaces," in *Electrical Contacts, Proceedings of the Annual Holm Conference on Electrical*

Contacts, 2015.

[35] T. V. Laurvick and R. A. Coutu, “Improving Gold/Gold Microcontact Performance and Reliability under Low-Frequency AC Through Circuit Loading,” *IEEE Trans. Components, Packag. Manuf. Technol.*, 2017.

[36] D. C. Montgomery, *Design and Analysis of Experiments - Eighth Edition*. 2012.

[37] T. Laurvick, C. Stilson, and R. Coutu, “Experimental investigation of thin film spreading resistance in micro-contacts,” in *Electrical Contacts, Proceedings of the Annual Holm Conference on Electrical Contacts*, 2015.

REPORT DOCUMENTATION PAGE

Form Approved
OMB No. 0704-0188

The public reporting burden for this collection of information is estimated to average 1 hour per response, including the time for reviewing instructions, searching existing data sources, gathering and maintaining the data needed, and completing and reviewing the collection of information. Send comments regarding this burden estimate or any other aspect of this collection of information, including suggestions for reducing the burden, to Department of Defense, Washington Headquarters Services, Directorate for Information Operations and Reports (0704-0188), 1215 Jefferson Davis Highway, Suite 1204, Arlington, VA 22202-4302. Respondents should be aware that notwithstanding any other provision of law, no person shall be subject to any penalty for failing to comply with a collection of information if it does not display a currently valid OMB control number.
PLEASE DO NOT RETURN YOUR FORM TO THE ABOVE ADDRESS.

1. REPORT DATE *(DD-MM-YYYY)*: 21-03-2019

2. REPORT TYPE: Master's Thesis

3. DATES COVERED *(From - To)*: August 2017 - March 2019

4. TITLE AND SUBTITLE
Micro-contacts with 3-D Surfaces made with Grayscale Lithography

5a. CONTRACT NUMBER

5b. GRANT NUMBER

5c. PROGRAM ELEMENT NUMBER

6. AUTHOR(S)
Michaud, Paul L.J., 2d Lt, USAF

5d. PROJECT NUMBER

5e. TASK NUMBER

5f. WORK UNIT NUMBER

7. PERFORMING ORGANIZATION NAME(S) AND ADDRESS(ES)
Air Force Institute of Technology
Graduate School of Engineering and Management (AFIT/EN)
2950 Hobson Way
Wright-Patterson AFB OH 45433-7765

8. PERFORMING ORGANIZATION REPORT NUMBER
AFIT-ENG-19-M-043

9. SPONSORING/MONITORING AGENCY NAME(S) AND ADDRESS(ES)
Intentionally Left Blank

10. SPONSOR/MONITOR'S ACRONYM(S)

11. SPONSOR/MONITOR'S REPORT NUMBER(S)

12. DISTRIBUTION/AVAILABILITY STATEMENT
DISTRIBUTION A. APPROVED FOR PUBLIC RELEASE; DISTRIBUTION UNLIMITED.

13. SUPPLEMENTARY NOTES
This work is declared a work of the U.S. Government and is not subject to copyright protection in the United States.

14. ABSTRACT
The aim of this research is to design and fabricate micro-contacts with three-dimensional surfaces using grayscale lithography. The goal was to create devices that have stable resistances within the ballistic electron transport region. These devices were designed to restrict current to smaller areas to take advantage of micro-contact physics. The micro-contact designs were created with a factorial design to determine factors that are significant to operating within the ballistic region and maintaining a stable contact resistance. The contacts were tested in a test stand filled with nitrogen that uses a piezoelectric actuator to cycle the devices with an applied signal for a specified number of cycles. The contact resistance and the force were recorded at certain points during testing. Testing revealed that certain micro-contacts with three-dimensional surfaces fit into the ballistic electron transport model for 1 million cycles. After testing, the micro-contacts were inspected using a Scanning Electron Microscope to determine the presence of failure mechanisms.

15. SUBJECT TERMS
Micro-contacts, Ballistic Electron Transport, Grayscale Lithography

16. SECURITY CLASSIFICATION OF: a. REPORT	b. ABSTRACT	c. THIS PAGE	17. LIMITATION OF ABSTRACT	18. NUMBER OF PAGES
U	U	U	UU	146

19a. NAME OF RESPONSIBLE PERSON
Maj Tod Laurvick, AFIT/ENG

19b. TELEPHONE NUMBER *(Include area code)*
(937) 255-3636 x4382 tod.laurvick@afit.edu